Phreatomagmatic eruption products from the maar complex of Lamongan Volcanic Field (LVF), East Java, Indonesia

インドネシア東ジャワ州ラモンガン火山地帯（LVF）のマール複合火山からのマグマ水蒸気噴火噴出物

Andriansyah Gurusinga

アンデリアンシャー グルシンガ

Doctoral Thesis

Submitted in fulfilment of the requirements for the Degree of Doctor of Science

Department of Geosciences, Geotechnology, Material Engineering for Resources

Akita University

February

2024

Mt. Pinatubo in May 1994 by **Marko Riikonen**

"Phreatomagmatic eruptions are the most dangerous type of volcanic eruption, as they can occur without warning and can produce large amounts of ash and debris."

- Dr. Janine Krippner

ABSTRACT

Phreatomagmatic eruptions at maar volcanoes produce ash-rich pyroclastic deposits that record information about eruption dynamics and the underlying magmatic system. This thesis characterized volcanic ash preserved in maar deposits of the Lamongan Volcanic Field (LVF), East Java, to advance understanding of maar eruption processes and magmatism.

The investigation of ash particles through integrated analysis of textural, morphometric, and geochemical properties from six maars reflected factors influencing the variability of ash particle type and morphology. Two juvenile ash types were identified: Juvenile A (black and brown ash) and Juvenile B (orange-brown ash), reflecting different fragmentation mechanisms. Juvenile A particles exhibited blocky shapes despite heterogeneous basaltic compositions, highlighting phreatomagmatic fragmentation. Irregular Juvenile B particles indicated magmatic fragmentation of basaltic andesite magma.

Geochemical analysis of ash particles revealed two fractional crystallization trends influencing compositional variation. Major and trace element compositions revealed two fractionation trends from mafic to felsic endmembers, influenced by clinopyroxene ± olivine + plagioclase ± Fe-Ti oxide fractionation and plagioclase ± minor Fe-Ti oxide fractionation, respectively. Primitive scoria and lava compositions suggested evolution from a spinel ± garnet peridotite source undergoing crustal assimilation and fractional crystallization.

Stratigraphic characterization and ash aggregate identification at Ranu Klakah maar tracked changing eruption styles over time. Abundant aggregates in Unit 2 are correlated with intense wet conditions optimum for aggregation. Altered domains and juvenile materials within aggregates provided insights into magmatic fragmentation and vent material recycling over time. Componentry, morphometry, and mineralogy fingerprinted variable eruption dynamics through aggregate preservation.

This integrated study demonstrates how volcanic ash characterization illuminates maar eruption dynamics and heterogeneity within small-scale basaltic magmatic systems like the LVF. Such multi-parameter analyses advance understanding of volcanic processes influencing monogenetic volcanism and associated hazards.

[Keywords] phreatomagmatic, maar, volcanic ash, geochemistry, ash aggregates, Lamongan Volcanic Field

ACKNOWLEDGEMENTS

I would like to express my deepest gratitude to my supervisor, Professor Tsukasa Ohba, for his invaluable guidance, support, and feedback throughout this research project. His expertise in volcanology and petrology, encouragement of my scientific development, and dedication to improving this work significantly enhanced my knowledge and understanding. I am also thankful to Dr. Takashi Hoshide for his continuous discussion and technical assistance, especially with SEM-EPMA instrumentation. Prof. Agung Harijoko and Dr. Mirzam Abdurrahman for their invaluable insights to improve this work.

I am grateful to Yumi Hayakawa for providing valuable laboratory support and Associate Prof. Ryohei Takahashi and Dr. Hinako Sato from the Economic Geology Laboratory for facilitating ICP-MS analysis. I appreciate the generous support from the Perum Perhutani Klakah and Segaran people, Om Kasno, Pak Aris, Pak Jumadi, and Pak Mistur during the fieldwork. Thanks also to Khoirul Haq Nur Rohman and Moch. As'ad Muzakky for assistance, during the field investigation and sample collection.

I would like to extend my appreciation to the Volcanology and Petrology Laboratory members. Wildan Nur Hamzah, Reza Firmansyah Hasibuan, Renaldi Suhendra, Takumi Imura, Mradipta Lintang Alifcanta Moktikanana, Muhammad Burhanuddin Sulhuzair, Aulia Agus Patria, Muhammad Alfath Salni, Jananda Nuralam Indriyanto, Rinaldi Ikhram, Arifuddin Jamil, Astiti Aggorowati, Volcanolovers members, Indranova Suhendro, and Gabriela Nogo Retnaningtyas Bunga Naen. I appreciate their camaraderie and insightful scientific discussions that aided my research.

Heartfelt thanks are also due to my inspiring friends. All members of PPI Akita: Fadlin, Nanda Ajeng Nurwantari, Cendi Diar Permata Dana, Renaldi Suhendra, Reza Firmansyah Hasibuan, Muhammad Arfah, Benny Sumaryono, Reza Al Furqan, Jananda Nuralam Indriyanto, Adi Sulaksono, Muhammad Burhanuddin Sulhuzair, Rahman Ardiansyah, Astiti Aggorowati, Fareza Sasongko, Wildan Nur Hamzah, Arifuddin Jamil, Rinaldi Ikhram, Hartaja Wicaksono, Reza MD, Mradipta L A Moktikanana, Arba Azzaman, Aulia Agus Patria, Enrico G W Suharjo, Mirai Suchayla, Syaiful Hilal, Mirna Mariana, Tighfar Ahmadjayadi, Firda Fahriandini, Naufal F, Alvi Fauzan, Gabriela C N Gaspersz, Sherinna M Cahyani, Afi Ishendriati, Anjali K Wardani, Taufiq Abbiyu R, Tommy Herawan, Y Zaki Agung, and Ikhsan

Chalik. All Indonesian residents in Akita: Koseki Dewi, Ani Komatsu, Meriyani Rika, Nana Sugawara, Raden Eliani, Sugiyati Kamada, Wahyu, Rudy, Hiday, Latief, and all their families. Oishi-tomodachi: Dragana Adamovic, Bennedict Mabuto, Hernan Gabriel, Hiromi Camile, Amanda Thiemi, Batlile Tsae, Olaotse Deezy, and Taka. FIRES colleague (Manuel, June, Leeysmon, Malika, Daher, Ali, Paulo, and Jonathan), IBC-badminton member, AXT-International and JC soccer teams. Their friendship has been an invaluable personal anchor throughout this process, and I appreciate each of them for standing by my side. They made my life in Akita much happier and more colorful.

I dedicate this thesis to my beloved parents, Mamak Mariam br Tarigan and Bapak Budiyanto Gurusinga, my sister Noer Intan Prasidha br Gurusinga, Nenek, Kakek, Iting, Mama, and extended family who have always encouraged and supported my education through unconditional love, care, and sacrifice. My success would not have been possible without their endless guidance and faith in me.

Most of all, I am eternally grateful to my wife, Vetty Alfiarnika, and our newborn son, Yazeed Eren Gurusinga, for the unwavering love, support, and understanding throughout the challenges of conducting doctoral research abroad. Their encouragement and belief in me helped motivate me to persevere, especially during difficult periods. I am truly grateful to have had them by my side, contributing to my success through their companion.

Finally, I acknowledge the funding support provided by the Ministry of Education, Culture, Sports, Science, and Technology of Japan (MEXT) and Akita University that enabled my doctoral studies in Japan and greatly facilitated the successful completion of this research.

Akita, February 2024

Mhd. Andriansyah Gurusinga

TABLE OF CONTENTS

LIST OF FIGURES

LIST OF TABLES

LIST OF APPENDIX

Publications arising from this thesis

Journal articles

Gurusinga, M. A., Ohba, T., Harijoko, A., & Hoshide, T. (2023). Characteristics of ash particles from the maar complex of Lamongan Volcanic Field (LVF), East Java, Indonesia: How textural features and magma composition control ash morphology. Volcanica, 6(2), 415–436. https://doi.org/10.30909/vol.06.02.415436

Conference Abstracts

Gurusinga, A., & Ohba, T. (2020). The characteristics of phreatomagmatic ash particles from maar complex of Lamongan Volcanic Field, East Java, Indonesia. Abstract volume, International Maar Conference (IMC-8), Petropavlovsk-Kamchatsky, Russia: p.28-29.

Gurusinga, A., & Ohba, T. (2022). Characteristics of Ash Particle from Maar Complex, Lamongan Volcanic Field (LVF), East Java, Indonesia. Japan Geoscience Union (JpGU) Meeting, Chiba, Japan, 22 May – 3 June.

Gurusinga, A., & Ohba, T. (2023). Characteristics and origins of erupted volcanic ash particles: Insights from maar complex deposits at Lamongan Volcanic Field, East Java, Indonesia. Abstract volume, IAVCEI Scientific Assembly, Rotorua, New Zealand. 30 Jan – 3 Feb: p.280.

Gurusinga, M., A., Ohba, T., Harijoko, A., & Hoshide, T. (2023). The magmatic system beneath maar complex revealed from the geochemistry of ash particles at Lamongan Volcanic Field (LVF), East Java, Indonesia. Japan Geoscience Union (JpGU) Meeting, Chiba, Japan, 22 – 26 May.

Chapter I - General Introduction

1.1. Phreatomagmatism

Phreatomagmatism refers to volcanic eruptions triggered by the explosive interaction of rising or intruding magma with external water sources such as groundwater, surface water, seawater, or glacial meltwater (Lorenz, 1986; White & Houghton, 2006; White & Ross, 2011; Zimanowski, 2015). The rapid expansion of water into steam due to the contact produces explosive interactions that can shatter and excavate country rocks (Rosseel et al., 2006; Németh & Kósik, 2020). The resulting ejected pyroclastic material can vary in size and composition. Phreatomagmatic eruptions produce typical pyroclastic deposits and landforms, reflecting the explosive interaction between magma and water, including coarse cinder, ash agglomerate deposits, and circular landforms like tuff rings/cones and maar, respectively (Cas & Wright, 1987; Wohletz & Sheridan, 1983; White & Ross, 2011).

The nature and intensity of phreatomagmatic eruptions are closely controlled by several interrelated parameters, including the amount of water involved, its proximity to the vent, and the temperature and composition of the magma (Cas & Wright, 1987; White & Houghton, 2006; Valentine & White, 2012). A large volume of water coming into contact with magma can lead to rapid expansion of steam (sudden conversion of water to steam), which generates a significant pressure change and thus causes highly explosive eruptions. In accordance, the close location of water to the vent allows immediate and intense heat transfer, resulting in more explosive eruptions, and vice versa. Moreover, the magma temperature also contributes, and hot magma rising into contact with water can lead to a rapid expansion of steam and an intense explosive eruption. In addition, the dynamics of a phreatomagmatic eruption also relate to the chemical composition of magma and other external factors. Magma composition influences the rheology (study of deformation and flow in matter) of the melt and its volatile content, which are linked to its inter-related physical properties, including viscosity, bubble content and size,

crystallinity, etc. (Avery et al., 2017). However, external factors such as conduit architecture, terrain and substrate permeability may allow for alternating dynamics and multiple pulse of eruption activity (Avery et al., 2017; Graettinger & Valentine, 2017).

The volcanoes that are primarily formed by phreatomagmatic explosions are maar-diatremes, which are the most common sub-aerial volcanoes on Earth after scoria cones (Sweeney & Valentine, 2015). They are commonly characterized by a crater floored below the pre-eruptive surface, a low-angle tephra ring, and a subsurface vent structure (diatreme) that extends up to 2 km to the feeder dike (White & Ross, 2011). These landforms are not only limited to monogenetic volcanoes but also to larger composite volcanoes. In the composite volcanic system, the magma-water interaction commonly triggers phreatomagmatic activity at the margins or flanks of stratovolcanoes, where rising magma following fractures (evolution of feeder dike) intersect with shallow groundwater or surface hydrothermal reservoirs (e.g. Geshi et al., 2019).

1.2. Monogenetic volcanic fields

Monogenetic volcanic fields represent common features across basaltic volcanic terrains worldwide. They form from multiple eruption of small-centered volcanoes within a defined area and age (Valentine & Connor, 2015). Each individual volcano formed by discrete injections of typically basaltic magma (less than 52 wt% SiO_2) at shallow crustal levels (Németh et al., 2003; Brenna et al., 2015; Cortés et al., 2015; Geshi et al., 2022). Most of these volcanoes produced small total erupted products at less than 1 km^3 volume (Valentine & Connor, 2015). In contrast to larger composite volcanoes that are constructed through successive layers of eruptive deposits, monogenetic volcanic centers are not built up gradually over time. Instead, they typically erupt just once or within relatively short periods of activity before becoming dormant.

Eruptive activity at monogenetic volcanic centers is typically characterized by either phreatomagmatic or strombolian eruptive style (Wohletz & Sheridan, 1983), with switching between the two observed. Strombolian eruptions arise from intermittent ejection of molten tephra particles between episodes of lava fountaining at the vent, constructing modest spatter and cinder cones as magma ascends through the conduit while degassing (Wilson and Head, 1981). In contrast, phreatomagmatic eruptions are initiated upon direct interaction magma with external water, generating powerful explosions via rapid steam production and through fragmentation process (Wohletz & Sheridan, 1983; White & Ross, 2011). These hydromagmatic explosion efficiently fracture magma into finely fragmented tephra particles due to explosive energy generated (Wohletz & Sheridan, 1983). This explosivity associated with phreatomagmatic activity thereby significantly exceeds that of strombolian eruptions, owing to the additional energy released through magma-water interactions (Wohletz & Sheridan, 1983; Cashman & Giordano, 2014).

Overall, monogenetic volcanic fields represent a landscapes constructed over time by the accumulation of numerous single-vent eruptions. These individual centers are typically small and characterized by short-duration eruptive periods, rapidly initiating and terminating activity (Wohletz & Sheridan, 1983; Valentine & Connor, 2015). Common edifice types arising from strombolian explosive activity are cinder or spatter cones, with only minimal associated with lava flows (Cashman & Giordano, 2014). However, the characteristic landforms defining numerous monogenetic fields are the uniquely structured maar volcanoes (Lorenz, 1973; 1986; Wohletz & Sheridan, 1983). Maar volcanoes initiate when magma intersects a shallow aquifer or surface water, triggering powerful steam-driven explosive eruption that excavate shallow crater through ejection of tephra and hydraulic fracturing of substrate rocks (Wohletz & Sheridan, 1983; Lorenz, 1986).

1.3. Lamongan Volcanic Field (LVF)

Lamongan Volcanic Field (LVF) is located *c.* 140 km southeast of Surabaya, East Java, Indonesia, and lies between the Tengger-Semeru and Iyang-Argapura volcanic complexes. The LVF and its surroundings are the product of Pleistocene to Holocene volcanism (Suwarti & Suharsono, 1992). Lamongan volcano, the central edifice, consists of three vents: Tarub, Tjupu, and Lamongan. The oldest vent is the truncated Tarub cone. Tjupu is a scoria cone complex that covers several hundred meters between Lamongan and Tarub. Lamongan is a basaltic stratovolcano with an NW-SE linear orientation. It is, to date, the only active vent, with lava flows covering the west and southwest flanks. Although the first historical eruption occurred in 1799 CE, the Lamongan volcano was one of the most active volcanoes in Indonesia during the 19th century. It has undergone around 40 eruptions, including 15 effusive basaltic eruptions (Carn, 2000). Following the last six eruptions in 1898, seismic activity in the west region of the LVF in 1925, 1978, 1985, and 1988–1989 raised awareness of volcanic hazards in this area.

The LVF covers an area of 260 km^2. It comprises several prehistoric centers, including 61 cinder-spatter cones and 29 maars, distributed on the flanks around the central edifice (Fig. 1). The maars have variable dimensions (crater diameters from 175 to 575 m) and were formed by eruptions that ejected tephra volumes of 0.02–51 x 10^6 m^3 dense rock equivalent (DRE) (Carn, 2000). In terms of eruptive rate and volume, Carn (2000) estimated the age of the LVF to range from 40 to 13 ka and placed it among the youngest-dated volcanoes in Indonesia. LVF maar deposits include pyroclastic surges, pyroclastic flows, ash falls, and ballistic ejecta of various sizes.

According to Carn and Pyle (2001), the eruptive products of the LVF range in composition from basaltic-to-basaltic andesite (~43–56 wt% SiO_2 and ~0.6–2.2 wt% K_2O). The lava samples from this field represent some of the most silica-undersaturated (lowest SiO_2 content) compositions yet found in the Sunda arc, indicating the presence of relatively primitive

magmas. The most primitive lavas are associated with some of the youngest cinder cones, suggesting a recent influx of new magma into the system. These lavas possess unusual compositions (e.g. high TiO_2, FeO*, CaO, and low SiO_2) that may indicate unique source conditions and melting processes (Carn and Pyle, 2001). The geochemistry of cinder cones from the northern region of LVF correlates them to the recent lava from Semeru volcano, whereas some cones in the west area are the parental to lavas from Bromo, despite the similar locations of these volcanoes relative to the trench (Carn and Pyle, 2001). This highlights the significant role of extensional tectonics in this region in governing the style and composition of volcanism.

1.4. Thesis rationale and organization

Phreatomagmatic eruptions arising from maar volcanoes within monogenetic volcanic fields, such as the LVF, bring significant challenges and risks to nearby communities due to their violent explosivity and wet volcanism. Hence, understanding the eruption histories of these volcanoes is essential. One of the most appropriate approaches to fulfilling this goal is the examination of eruptive materials, including pyroclastic deposits and lava flows. Furthermore, it is important to note that the characteristics of eruptive deposits exhibit temporal and spatial variations, thereby offering valuable insights into dynamic nature of volcanic events. In order to fully evaluate of the various attributes of these deposits, we have utilized a combination of detailed observation, analysis of texture, morphology, and examination of geochemical data. This approach will enable us to explore the complex processes of phreatomagmatism and the underlying magmatic system.

The general purpose of this study is to characterize the pyroclastic deposits on the maar volcanoes and to determine the origin of the products and to understand the eruption processes involved. It included the primary eruption products (all clasts that are features of fragmented magma) and secondary products (clast that have been changed due to alteration process as well

as ash aggregates). In specific, the purpose is to determine (1) the factors that control the variation of ash particles from maar eruptions, (2) the magmatic system beneath maar complex using fine-sized fractions as a common product of explosive eruptions, and (3) the implication of secondary products (in this case ash aggregates) to the evolution of volcanic system during the typical short-term maar eruptions phase.

Each aim of this study has been grouped into a chapter, including a general introduction as well as summary and conclusions, yielding a total of five chapters. Specifically, the main chapters (Chapters II, III and IV) are written in a style that appropriate for publication. Moreover, only slight modification has been made to the published version of Chapter II.

Chapter I provides background information on the study of phreatomagmatic products from maar complex of Lamongan Volcanic Field (LVF).

Chapter II presents an integrated approach using physical, morphological, and magmatic properties to explain the variation of ash particles from maar eruption. This chapter provides new and significant insights into the fragmentation dynamics that govern the shape of pyroclasts in the LVF maar complex, despite varying magma properties.

Chapter III presents a geochemical study on ash particles from the LVF maar complex. This chapter highlights the importance of basic component analysis for fine-sized fraction of eruption products. This approach revealed consistent geochemical properties among the ash sample types. Accordingly, this study offers the potential to obtain valuable geochemical data on explosive eruptions that produce ash-dominated products. Such data can greatly contribute to our understanding of magmatic system associated with the dynamics of explosive eruptions.

Chapter IV presents a stratigraphic identification of ash aggregate-bearing layers. This chapter highlights the complex and time-transgressive nature of Ranu Klakah Maar eruptions, which progress from drier to wetter and back again as water availability fluctuates. Moreover, the occurrence of two different materials in the pyroclastic deposits and ash aggregates highlights

the complex recurrent nature of maar eruptions, which involve both syn- and post-eruptive products.

Chapter V provides a conclusion and summary of the major findings of the thesis.

1.5. REFERENCE

Avery, M., Panter, K., & Gorsevski, P. (2017). Distinguishing styles of explosive eruptions at erebus, redoubt and taupo volcanoes using multivariate analysis of ash morphometrics. *Journal of Volcanology and Geothermal Research, 332*, 1-13. https://doi.org/10.1016/j.jvolgeores.2017.01.010

Brenna, M., Nakada, S., Miura, D., Toshida, K., Ito, H., Hokanishi, N., & Nakai, S. (2015). A trachyte–syenite core within a basaltic nest: filtering of primitive injections by a multi-stage magma plumbing system (oki-dōzen, south-west japan). Contributions to Mineralogy and Petrology, 170(2). https://doi.org/10.1007/s00410-015-1181-0

Cashman, K. V., & Giordano, G. (2014). Calderas and magma reservoirs. Journal of Volcanology and Geothermal Research, 288, 28-45. https://doi.org/10.1016/j.jvolgeores.2014.09.007

Carn, S. A. (2000). The Lamongan volcanic field, East Java, Indonesia: Physical volcanology, historic activity and hazards. *Journal of Volcanology and Geothermal Research*, *95*(1–4), 81–108. https://doi.org/10.1016/S0377-0273(99)00114-6

Carn, S. A., & Pyle, D. M. (2001). Petrology and geochemistry of the Lamongan volcanic field, East Java, Indonesia: Primitive Sunda arc magmas in an extensional tectonic setting? *Journal of Petrology*, *42*(9), 1643–1683. https://doi.org/10.1093/petrology/42.9.1643

Cortés, J., Smith, E., Valentine, G., Johnsen, R., Rasoazanamparany, C., Widom, E., … & Ruth, D. (2015). Intrinsic conditions of magma genesis at the lunar crater volcanic field (nevada), and implications for internal plumbing and magma ascent. American Mineralogist, 100(2-3), 396-413. https://doi.org/10.2138/am-2015-4812

Geshi, N., Németh, K., Noguchi, R., & Oikawa, T. (2019). Shift from magmatic to phreatomagmatic explosions controlled by the lateral evolution of a feeder dike in the suoana-kazahaya eruption, Miyakejima volcano, Japan. *Earth and Planetary Science Letters, 511*, 177-189. https://doi.org/10.1016/j.epsl.2019.01.038

Geshi, N., Oikawa, T., Weller, D., & Conway, C. (2022). Evolution of the magma plumbing system of miyakejima volcano with periodic recharge of basaltic magmas. Earth Planets and Space, 74(1). https://doi.org/10.1186/s40623-022-01577-7

Graettinger, A. and Valentine, G. A. (2017). Evidence for the relative depths and energies of phreatomagmatic explosions recorded in tephra rings. *Bulletin of Volcanology, 79*(12). https://doi.org/10.1007/s00445-017-1177-x

Lorenz, V. (1973). On the formation of maars. *Bull Volcanol 37*, 183–204. https://doi.org/10.1007/BF02597130

Lorenz, V. (1986). On the growth of maars and diatremes and its relevance to the formation of tuff rings. *Bull Volcanol* 48, 265–274. https://doi.org/10.1007/BF01081755

Németh, K. and Kósik, S. (2020). Review of explosive hydrovolcanism. *Geosciences, 10*(2), 44. https://doi.org/10.3390/geosciences10020044

Németh, K., White, J., Reay, A., & Martin, U. (2003). Compositional variation during monogenetic volcano growth and its implications for magma supply to continental volcanic fields. Journal of the Geological Society, 160(4), 523-530. https://doi.org/10.1144/0016-764902-131

Rosseel, J., White, J. M., & Houghton, B. F. (2006). Complex bombs of phreatomagmatic eruptions: role of agglomeration and welding in vents of the 1886 Rotomahana eruption, Tarawera, New Zealand. *Journal of Geophysical Research: Solid Earth, 111*(B12), n/a-n/a. https://doi.org/10.1029/2005jb004073

Sheridan, M. F. and Wohletz, K. H. (1983). Hydrovolcanism: basic considerations and review. *Journal of Volcanology and Geothermal Research, 17*(1-4), 1-29. https://doi.org/10.1016/0377-0273(83)90060-4

Sweeney, M. and Valentine, G. (2015). Transport and mixing dynamics from explosions in debris-filled volcanic conduits: numerical results and implications for maar-diatreme volcanoes. *Earth and Planetary Science Letters, 425*, 64-76. https://doi.org/10.1016/j.epsl.2015.05.038

Valentine, G., A., & Connor, C., B. (2015). Magma–water interaction and phreatomagmatic fragmentation. *The Encyclopedia of Volcanoes, 423-439*. http://dx.doi.org/10.1016/B978-0-12-385938-9.00023-7

Wilson, L. and Head, J. (1981). Ascent and eruption of basaltic magma on the earth and moon. Journal of Geophysical Research Atmospheres, 86(B4), 2971-3001. https://doi.org/10.1029/jb086ib04p02971

White, J. D. L. and Ross, P. (2011). Maar-diatreme volcanoes: a review. *Journal of Volcanology and Geothermal Research, 201*(1-4), 1-29. https://doi.org/10.1016/j.jvolgeores.2011.01.010

Zimanowski, B., Büttner, R., Dellino, P., White, J. D. L., & Wohletz, K. H. (2015). Magma–water interaction and phreatomagmatic fragmentation. *The Encyclopedia of Volcanoes, 473-484*. https://doi.org/10.1016/b978-0-12-385938-9.00026-2

Chapter II - The characteristics of ash particles from the maar complex of Lamongan Volcanic Field (LVF), East Java, Indonesia: how textural features and magma composition control ash morphology

2.1. INTRODUCTION

Maars are volcanic landforms typically generated by phreatomagmatic eruptions, which occur when magma comes into contact with shallow groundwater, leading to violent, ash-rich explosive eruptions (Sheridan & Wohletz, 1983; Lorentz, 1986; White & Ross, 2011; Smith & Németh, 2017; Valentine et al., 2017; Graettinger, 2018; Németh & Kósik, 2020). They often occur in groups or fields within multiple craters formed by closely spaced explosions over time (e.g. Lorentz, 1986; Jordan & Hayman, 2013; Morales Volosín & Risso, 2019). Maar-forming phreatomagmatic events produce a wide range of pyroclastic particles, each exhibiting distinctive properties and morphologies (Heiken, 1978; Wohletz, 1983; Sheridan & Wohletz, 1983; Dellino & Liotino, 2002; Mattsson, 2010). The characteristics of these pyroclastic particles, in particular in the ash size range, are influenced by the fragmentation processes (e.g. brittle vs. ductile) and magma properties (composition, viscosity, temperature, bubbles, and crystals) (Maria & Carey, 2002; 2007; Noguchi et al., 2008; Mattsson, 2010; Miwa et al., 2013; Liu et al., 2015; Nurfiani and de Maisonneuve, 2018; Ross et al., 2022), as well as by pyroclast transport (Manga et al., 2011; Kueppers et al., 2012; Jordan and Hayman, 2013; Liu et al., 2015; Hornby et al., 2020). Despite maar eruptions being driven by magma-water interaction, distinguishing the factors controlling the characteristics of the pyroclasts from maar eruptions remains a challenge. These are attributed to the underlying complexity of phreatomagmatic explosions, which involve dynamic interplay between magmatic properties and the explosivity of magma-water contact (Wohletz, 1983; Büttner et al., 2002; Schipper, 2009; Pardo et al., 2014). Consequently, further thorough investigations are required to unravel the key variables governing the heterogeneous characteristics of ash particles in maar volcanoes.

The deposits of the Lamongan Volcanic Field (LVF) maar complex in Indonesia provide an opportunity to evaluate the factors that control the characteristics of ash particles. We investigated particles from the ash-dominated proximal deposits at six maars, where particle modification by secondary processes such as transport is minimized (e.g. Liu et al., 2015; Hornby et al., 2020). Although previous studies have reported on the physical volcanology and the geochemistry of the LVF (Carn, 2000; Carn & Pyle, 2001), none have investigated the pyroclast products from the Maar complex. The objective of this study is to provide a comprehensive analysis of ash particles derived from the LVF maar complex, with a primary emphasis on their morphological, textural, and geochemical characteristics (e.g. White & Houghton, 2006; Cioni et al., 2008; Ross & White, 2012; Rausch et al., 2015). Through this analysis, we aim to elucidate the underlying variables that govern the variability of ash properties and morphologies generated by maar eruptions.

2.2. METHODS

Ash samples were collected from five crater-wall maar exposures to minimize the influence of the transport process, except for one outcrop situated approximately 200 m NE of Ranu Kembar maar, which was included to supplement the limited outcrops in the eastern region (Fig. 2.1e). In cases where deposits were consolidated, the samples were disaggregated by gently hitting them with a rubber hammer wrapped in a soft fabric. The samples were then manually dry-sieved using a whole-ϕ interval. Subsequently, particles ranging in size from 125−250 μm (+3 to +2 ϕ) from ash-rich layers were selected and subjected to ultrasonic cleaning in order to remove any adhering muddy material. To prevent potential damage to the original ash particles that could arise from prolonged ultrasonic treatment, the cleaning cycles were interrupted, and water was replaced every 60−90 seconds.

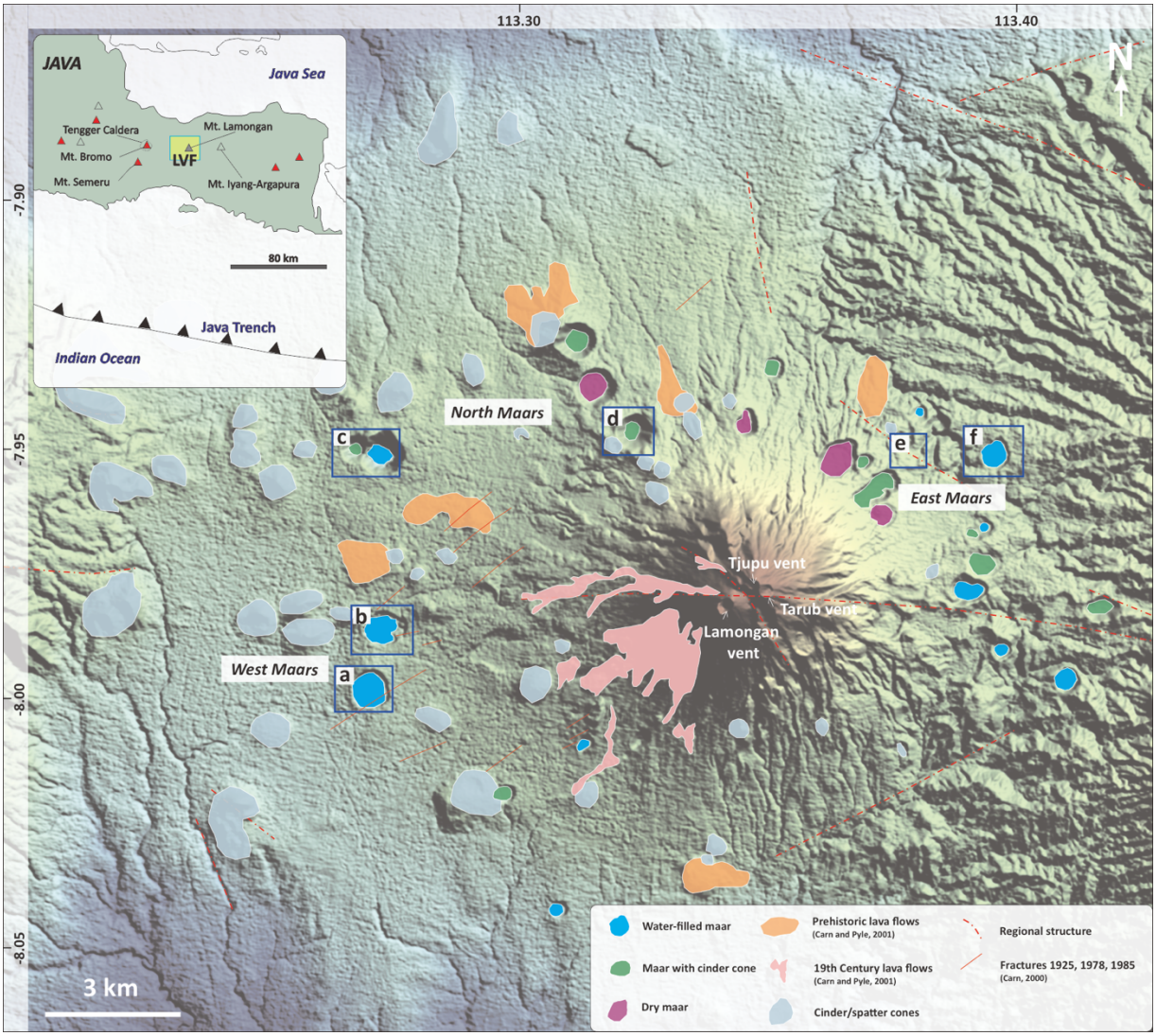

Figure 2. 1. Location and sample map for the LVF maar complex. The digital elevation model (DEM) was downloaded from https://tanahair.indonesia.go.id/demnas. The maars included in this study are indicated by blue squares and labeled as follows: (**a**) Ranu Pakis, (**b**) Ranu Klakah, (**c**) Ranu Kering, (**d**) Ranu Air, (**e**) outcrop NE of Ranu Kembar, and (**f**) Ranu Segaran. The distribution of maars, lava flows, and cinder-spatter cones on LVF is based on Carn and Pyle (2001).

Upon completion of the drying process, the samples underwent an epoxy immersion process, following which the lower part of the briquette was polished until the central portion of each grain became visible (Comida et al., 2022). This polished part was mounted to the glass slide and then prepared into a polished thin section of 30 µm thickness. Polarized light microscopy was utilized to determine the ash components and shapes. Juvenile (black, brown, and orange ash) and other (altered/weathered ash and free crystals) grains were discriminated on the basis of color and internal texture.

To quantify the morphometric parameters of the ash particles in 2D cross-sections, we delineated their outlines on photomicrographs using a vector editing tool (*Corel Draw*). We converted the drawings into black-and-white (binary) TIFF files. Particles were hand-delineated due to the presence of fine aggregate coatings on some grains, which could interfere with automated edge detection. The clast images were processed using Particle Shape Analyzer (*PARTISAN*), a software application developed by Dürig et al. (2018) written in *MATLAB* ®TM. This yielded image particle analysis (IPA) parameters (Dellino & La Volpe, 1996) and morphometric parameters from the Liu et al. (2015) system, such as [1] *Circularity* ($Circ_{DL}$); [2] *Rectangularity* (Rec_{DL}); [3] *Compactness* (Com_{DL}); [4] *Elongation* (Elo_{DL}) and [5] *Form Factor* (*FF*); [6] *Axial Ratio* (AR_{LI}); [7] *Convexity* (Con_{LI}); [8] *Solidity* (Sol_{LI}), respectively.

Furthermore, ash particles were observed using a scanning electron microscope (SEM) of the JEOL JSM-IT300 model at Akita University, both as cross-sections (the thin section mentioned above) and in three dimensions (3D). For the latter method, ash grains from the same size fraction were mounted on a glass slide using carbon tape. Subsequently, both the thin sections and the carbon tape grain mounts were coated with ~30 nm of carbon. The identification of 3D grain morphology and surface features was performed in secondary electron (SE) mode, while petrography and textures of particle cross-section were examined in backscattered electron (BSE) mode. The SEM operation was conducted under high vacuum

conditions with a 15 kV accelerating voltage, a 10 mm working distance, and a probe current of 2.20 nA.

Crystals and vesicles were manually digitized from BSE images of the cross-sections using *Corel Draw*, both at relatively low magnification (80x to 170x) and at high magnification (500x to 1900x). The coalesced bubbles were corrected to separate the bubble edges and obtain the most relevant numbers of bubbles within the melt (Proussevitch et al., 2007a). Area, number, and size information were quantified using *ImageJ software*. These values were used to calculate the crystallinity and vesicularity in the vesicle-free and crystal-free fractions. To achieve the proper stereological habit of vesicles in 3D projection (best-fit shape), the CSD*slice* spreadsheet developed by Morgan and Jerram (2006) was utilized. The best-fit shape, represented by x-y-z values, was then input into the CSD*Correction* v.1.6 software developed by Higgins (2000, 2002, and 2007) for quantification of the vesicle number densities (*VND*) and vesicle volumes (*VV)* (http://www.uqac.ca/mhiggins/csdcorrections.html).

The geochemical composition of the eruption products from the LVF maar complex was determined through X-ray fluorescence (XRF) analysis. Initially, the freshest (glossy) and least altered particles from the 0.5-1 mm size fractions were hand-selected from representative ash classes. The ash grains were carefully selected based on their class from individual layers, ensuring there was no mixing with grains from different classes, layers, or other maars. These particles were further categorized into five classes (as further explained below), such as black non-vesicular (*bnv*), black vesicular (*bv*), grayish-black (gray) from east maars, clear-pale brown (*cb* + *pb*), and orange-brown (*ob*) ash particles. Enough ash particles of each class were combined to obtain sufficient mass for analysis (1.2–1.6 g). In addition, lava samples (from the north and east regions) and scoria cone deposits (from the north region) were also analyzed to identify geochemical variations in the area. The lava samples were collected from lava flow outcrops, while the scoria cone samples were obtained from lapilli fall deposits. All of the

samples were crushed, pulverized, and prepared as glass beads (melting pellets) and analyzed for major oxides using a ZSX Primus II from Rigaku Co. at Akita University.

As we did not have glass compositions (due to the high crystallinity groundmass on the ash particles), viscosities were estimated using whole rock compositions and *PELE* modeling coupled with constraints from the textural analysis. The determination of liquidus temperature and viscosity was obtained using *PELE* software (https://nicholas.duke.edu/people/faculty/boudreau/DownLoads.html). This software was utilized by integrating the geochemistry data with the assumption of 1.5% H_2O content, fO_2 at the QFM buffer, fractional crystallization, temperature from 1200–900°C (increment = 4°C), and pressure from 1000-10 bar (increment = 10 bar). The initial magma water content used for viscosity determination is referenced from Kelud volcano, as it possesses a similar magma composition to Lamongan volcano and is the only nearby volcano that provides this information. Cassidy et al. (2016) calculated the water content in Kelud volcano's magma under the assumption of dissolved H_2O within plagioclase-hosted melt inclusions. Subsequently, we matched *PELE* results with quantified crystallinity and observed mineral assemblages from the textural analysis. Then the temperature and viscosity values at equivalent crystallinities and mineral assemblages were taken as approximations of the natural magma conditions.

Furthermore, the relative viscosity of the samples was assessed by analyzing crystal content (crystallinity) and crystal size distributions (CSD) in vesicle-free fractions. The relative viscosity values were calculated using the Klein et al. (2018) spreadsheet, which incorporated the parameters of crystal aspect ratio and Feret diameter obtained from *ImageJ* together with the crystallinity data of each ash particle.

2.3. RESULTS

2.3.1 The maar deposits

The LVF maar deposits can be categorized into three locality groups (Fig. 2.1) based on proximity to the center of the Lamongan volcano and the type of crater, i.e., water-filled or dry. The three groups are [1] west maars (Ranu Pakis and Ranu Klakah); [2] north maars (Ranu Kering and Ranu Air); and [3] east maars (Ranu Segaran and an outcrop near Ranu Kembar). Water-filled craters characterize west and east maars, whereas north maars are distinguished by their dry craters (as described in Table 2.1).

Ranu Pakis Maar, a water-filled crater with a dimeter of 750 m, comprises three outcrops on the eastern crater wall (~19 m total thickness). The lower layers comprise grayish-brown deposits with lapilli and blocks, with intermittent intercalations of thin ash layers bearing accretionary lapilli. The upper layers consist of grayish-brown consolidated fine ash to lapilli deposits with some intercalations of thin dark and pale-yellow layers (10 cm) (Fig. 2.2b).

Ranu Klakah is a water-filled maar with a diameter of 675 m, exhibiting two outcrops with lateral continuity and a total exposed thickness of 6.3 m. The deposits are characterized by plane-parallel (planar) layers of fine to coarse ash from 10 to 15 cm in thickness. These layers are consolidated, well-sorted, and include a high proportion of accretionary lapilli. Within the lower layers, bomb sag structures resulting from the impact of ballistic materials on relatively soft and unconsolidated deposits can be observed (Fig. 2.2c). The upper layers are pale yellow, while the lower layers exhibit a grayish-brown color (Fig. 2.2d).

Ranu Kering is a dry crater maar with a diameter of 390 m, located on the eastern side of the water-filled crater of Ranu Bedali maar. The name “Ranu Kering” translates to "no water accumulation in the crater" in the local language. The western crater wall of Ranu Kering exhibits two pyroclastic outcrops with a 30 m elevation difference and a combined thickness of 10 m. The lower outcrop layers are grayish-brown, coarse (coarse ash to blocks), and contain

abundant orange-brown scoria clasts 0.5-2 cm across (Fig. 2.2e). Cross-lamination and bomb-sag structures are frequently observed at the base of the deposit. The upper outcrop displays grayish-black, coarse ash to lapilli with a high concentration of orange-brown scoria clasts and glassy black ash.

Ranu Air is a 350 m diameter dry crater maar and, of those in this study, is situated closest to Lamongan volcano's center. The total exposed thickness of pyroclastic deposits is 6 m. These deposits are characterized by a dark-greyish color, coarse ash to lapilli, loose to semi-consolidated, lithic-rich layers, and interlayering with accretionary lapilli-bearing ash layers (Fig. 2.2f).

An outcrop measuring 1.2 m in thickness is located 200 m to the northeast of Ranu Kembar Maar. The pyroclastic deposits are composed of grayish-brown, severely weathered, unconsolidated, thinly laminated layers (15 cm) ranging in grain size from coarse ash to lapilli. The upper part of the deposits contains interlayered thin black ash (~4 cm thickness) (Fig. 2.2g).

Ranu Segaran, a 545–m diameter water-filled maar, exhibits a strongly weathered, 1.8-m thick outcrop that was exposed by construction activities. The deposits are composed of grayish-orange fine ash to lapilli and contain cross-lamination structures (Fig. 2.2h). The deposits are characterized by a high concentration of sparkling-black particles of opaque minerals.

We generalized the succession of the proximal maar ejecta ring deposits by comparing the vertical successions of all the outcrops found within LVF (Fig. 2.2a). This generalized stratigraphic section is divided into three major units, distinguished by distinct characteristics.

Unit 1 comprises dark gray block-bearing lapilli layers with planar and cross-laminated bedding. These layers are clast-supported, poorly sorted, semi-consolidated, and commonly display the preserved impact structure of ballistic blocks. The lower bed is a lithic-rich layer

with a significant block size (>20 cm), while the upper bed consists of lapilli-dominated deposits interlayered with lapilli-bearing coarse ash layers.

A bedded package with cross-lamination and plane-parallel lamination characterizes unit 2. The predominant lithofacies within this unit are creamy brown to dark gray coarse ash to lapilli, occasionally with blocks, exhibiting a moderate degree of sorting. This lithofacies is typically matrix-supported and exhibits a semi-consolidated character. Additionally, the unit contains minor interlayered accretionary lapilli-bearing ash layers. Unit 2 is present in most of the studied maars.

Unit 3 is characterized by planar laminated ash deposits, commonly interlayered with accretionary lapilli. The unit exhibits a yellow to dark gray color and comprises well-sorted fine to coarse ash displaying moderate consolidation.

Table 2. 1. The relationship between ash particle distribution with the physical properties of LVF maars. V_J = juvenile volume; V_E = ejecta volume; d_{max}/d_{min} is a measure of maar shape (1= circular, >1= increasingly ellipsoidal). Asterisks indicate information taken from Carn (2000).

Characteristics		West		North		East	
		Ranu Pakis	Ranu Klakah	Ranu Kering	Ranu Air	outcrop NE Ranu Kembar	Ranu Segaran
ratio	bv/bnv	low		low		very low	
	cb/pb	moderate		moderate		low	
	cb+pb / bv+bnv	high		moderate		low	
ob		rare		rich	rare	rare	
fc		rare		rare	moderate	moderate	rich
SiO_2 (average wt%)		49.99	50.40	51.31	49.18	46.16	44.81
D_{mean}* (m)		755	675	395	350	-	545
maar shape* (d_{max}/d_{min})		1.13	1.25	1.43	1.55	-	1.42
V_J* DRE ($x10^6$ m^3)		7.4	3.9	2.5	1.8	-	17
V_E* DRE ($x10^6$ m^3)		50	37	17.8	12.7	-	20
Maar type		water-filled maar		dry maar		water-filled maar	

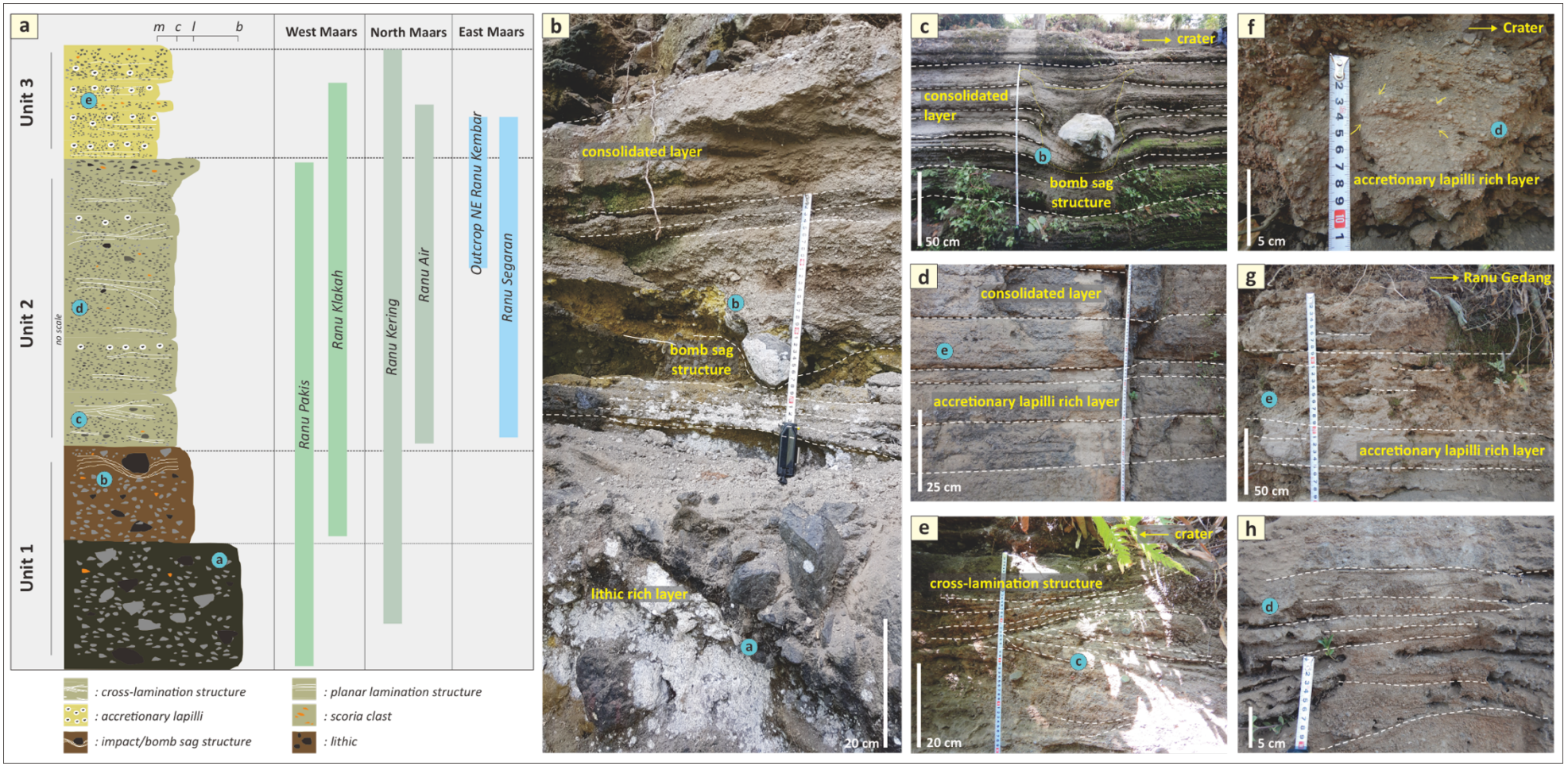

Figure 2. 2. (a) Generalized stratigraphic succession of the LVF maar complex. Vertical bars indicate the existence of a preserved outcrop from each maar, which is compared to the generalized stratigraphy. Blue circles with the letters denote depositional features on the stratigraphy unit. Images from representative outcrops are shown for (**b**) Ranu Pakis, (**c** and **d**) Ranu Klakah, (**e**) Ranu Kering, (**f**) Ranu Air, (**g**) outcrop NE Ranu Kembar, and (**h**) Ranu Segaran.

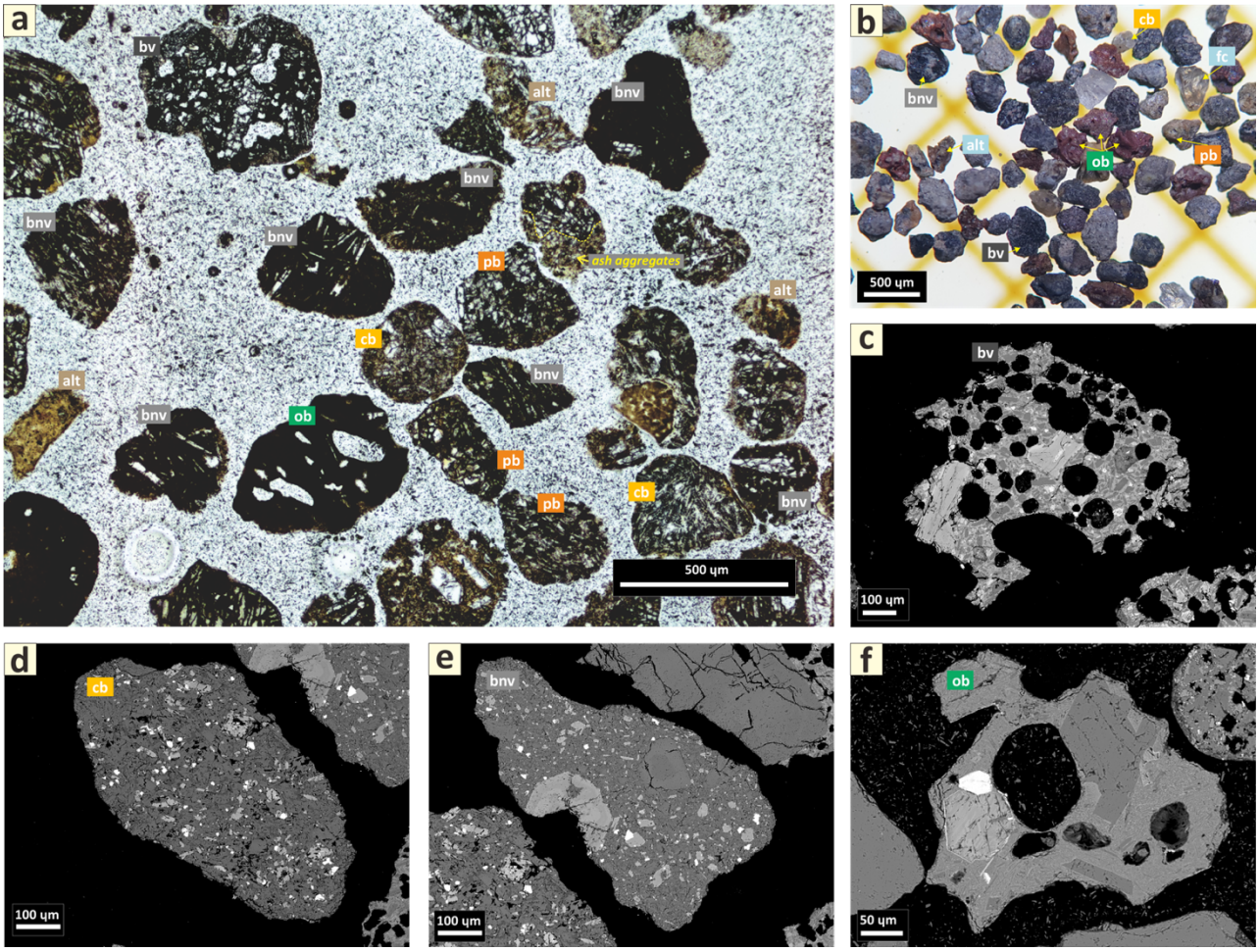

Figure 2. 3. Representative images of ash particles from LVF maar complex, including (**a**) thin-section samples under plane-polarized light (PPL) mode, (**b**) ash particle grains under a binocular microscope, (**c-f**) backscattered electron (BSE) images of ash types [(c) bv ash, (d) cb ash, (e) bnv ash, and (f) ob ash]. Ash particles can be categorized into three groups: juvenile A ash (cb, pb, bnv, and bv), juvenile B ash (ob), and other (fc and alt).

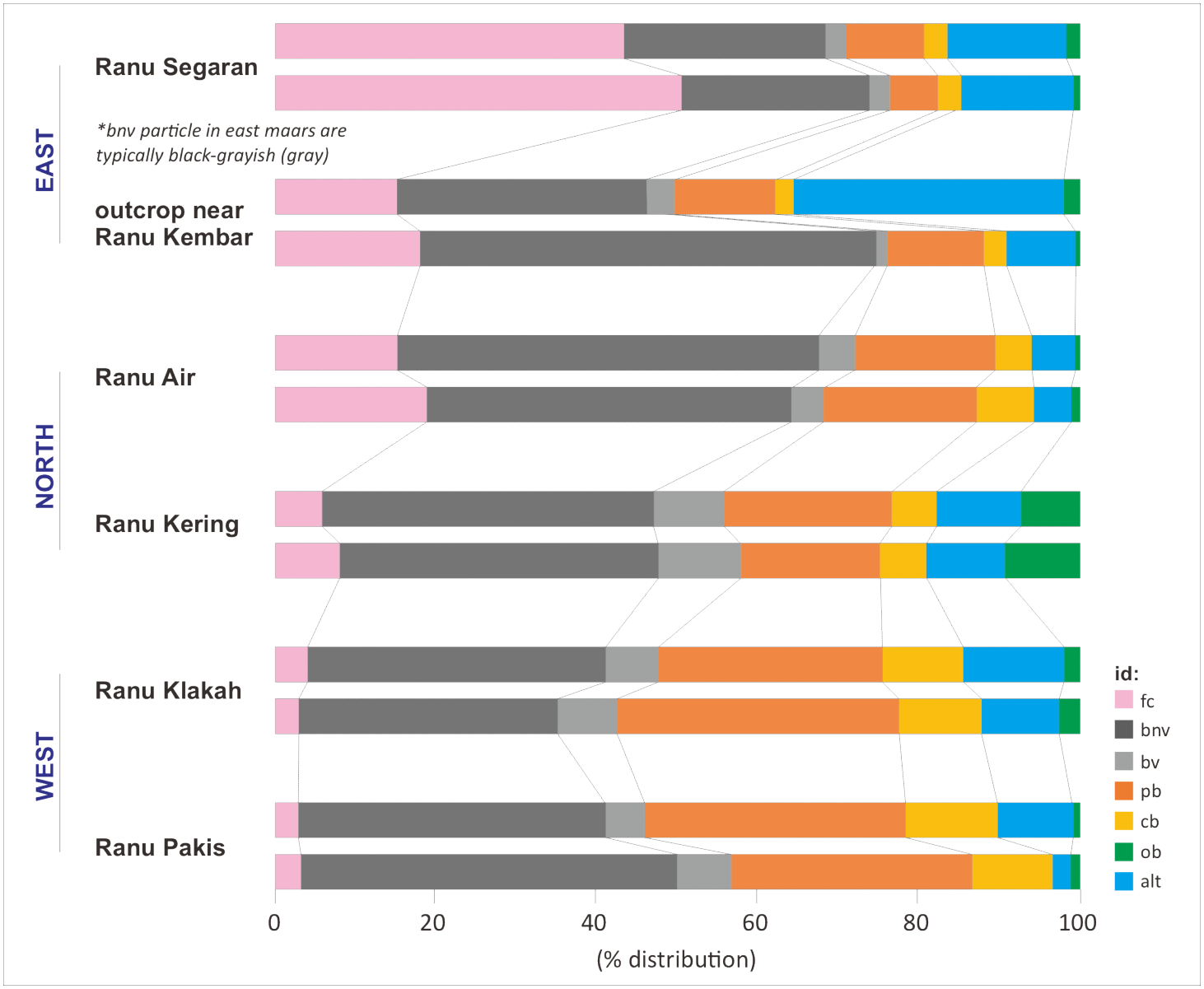

Figure 2. 4. Componentry distribution of the 125-250 µm fraction from the LVF maar complex deposits. The spatial view shows a decreased ratio distribution of brown ash (cb + pb) and black ash (bv + bnv) from east-north-west maars, while the free crystal content shows a contrary positive trend.

2.3.2. Ash characteristics

2.3.2a. Ash types and morphology

Based on the petrographic and scanning electron images, the ash particles have been categorized as juvenile particles or "other." There are two types of juveniles: type A and type B. Juvenile A grains are further subdivided into four classes: black non-vesicular, black vesicular, clear-brown, and pale-brown, which are described below. Juvenile B grains include only one class, orange-brown. Other particles include free crystals and altered (recycled) ash particles (as shown in Fig. 2.3) (e.g. D'Oriano et al., 2011; 2014). Generally, a range of ash particle types and classes are present in all maar deposits in varying proportions (Fig. 2.4).

Black non-vesicular ash (***bnv***) particles are characterized by their blocky shapes and stepped microcrystalline surfaces. This class of ash constitutes the most abundant fragments in the LVF maar complex, accounting for 28 to 49 vol.%, with slightly lower abundances observed in Ranu Klakah (25 vol.%) and Ranu Segaran (17–23 vol.%).

Black vesicular ash (***bv***) is an ash class with black-brown particles characterized by blocky to platy shapes and rough surfaces. The particles have equidimensional to elongate forms with convex outlines. While the *bv* ash particles are less abundant in the eastern maars (1.3−3.5 vol.%), they are slightly more common in the northern and western maars (4−10 vol.%).

Clear-brown (***cb***) and pale-brown (***pb***) particles are characterized by their sub-equant to elongate form, blocky to sub-round shape, rough surface, and microcrystalline texture. The average concentration of *cb* + *pb* ash particles decreases from 20.8 vol.% at the west maars to 12.4 vol.% at the north maars and to 6.3 vol.% at the east maars.

Orange-brown ash (***ob***) particles are characterized by an irregular to elongate shape with a smooth surface. Among the different classes of grains, the *ob* ash particles are the least

abundant, accounting for 0.5–2.3 vol.%, except in the samples from Ranu Kering Maar, where they represent a higher proportion of 7−9 vol.%.

Free crystals (***fc***) range in size from 100 µm to 1 mm and can be either intact or broken crystals of plagioclase, pyroxene, olivine, hornblende, and opaque minerals. These crystals are derived from either magma or country rocks. The distribution of the *fc* particles gradually increases from the west maars (average 3.3 vol.%) to the north maars (average 12 vol.%) and further to the east maars (average 31.8 vol.%). Among all the studied maars, samples from Ranu Segaran have the highest concentration of *fc* particles, with 50 vol.%.

Altered ash (***alt***) particles are small, dark-brown (about 200 µm) particles of weathered and altered ash. Except for the mag43-5 sample, which is an outcrop northeast of Ranu Kembar and has a distribution of 33 vol%, *alt* ash particles are relatively rare from LVF maar complex deposits, ranging from 2 to 14 vol%.

The ash components were initially defined through visual characterization during componentry analysis, after which quantitative morphology, texture, and geochemical analyses provided complementary datasets (explained below) that validated and further described the characteristics of these visually defined juvenile types and classes.

2.3.2b. Particle shape

Morphometric parameters were utilized to differentiate ash particle shapes based on various characteristics, including *Axial Ratio*, *Solidity*, *Convexity*, and *Form Factor* (Liu et al., 2015). *Axial Ratio* was used to distinguish between compact and elongate shapes, while *Solidity* was used to measure the area-based complexity and roughness of the ash particles. *Convexity* was used to measure the perimeter-based complexity and roughness, and *Form Factor* was utilized to quantify the deviation of a particle from a circular shape. These morphometric

parameters are commonly employed to characterize and distinguish between different types of ash particles.

The results of shape analysis (Fig. 2.5; Table 2.2) suggest that the west and north maars ash particles possess high *Solidity* and *Convexity* values, with average values of 0.93 and 0.95, respectively, while the *bv* ash has slightly lower *Convexity* values (average 0.92). Additionally, the west and north maars ash particles have an average *Axial Ratio* and *Form Factor* of 0.70 and 0.68, respectively. Notably, the *ob* particles from the Ranu Kering (north maar) exhibit lower values of *Solidity* (average 0.74), *Convexity* (average 0.73), *Axial Ratio* (average 0.65), and *Form Factor* (average 0.32). In the eastern maars samples, the average *Solidity* and *Convexity* values were found to be 0.92 and 0.88, respectively, while the average *Axial Ratio* and *Form Factor* values were 0.73 and 0.59, respectively. On average, the juvenile A particles from the east maars had more complex outlines and less circular shapes than the north or west maar ash.

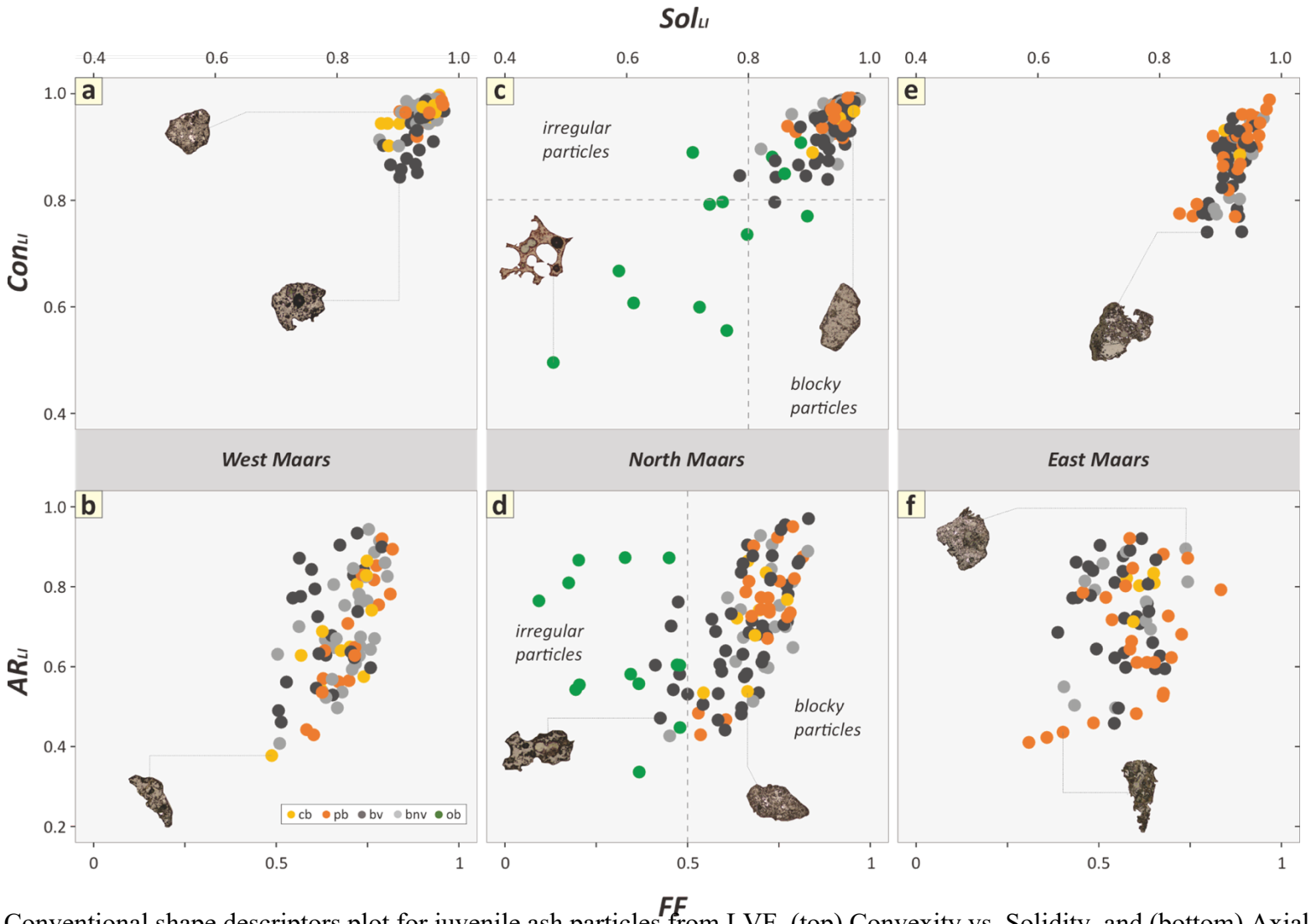

Figure 2. 5. Conventional shape descriptors plot for juvenile ash particles from LVF, (top) Convexity vs. Solidity, and (bottom) Axial Ratio vs. Form Factor; for (a and b) west maars, (c and d) north maars, and (e and f) east maars. Distinct values are particularly shown by ob ash particles from north maars.

Table 2. 2. Average values of morphometric parameters for ash particles from LVF.

Region	Maar	Ash Type	$Circ_{DL}$	Rec_{DL}	Com_{DL}	Elo_{DL}	FF	AR_{LI}	Con_{LI}	Sol_{LI}
West maars	Ranu Pakis	cb	1.22	0.90	0.72	1.91	0.67	0.64	0.95	0.93
		pb	1.20	0.90	0.76	2.00	0.70	0.65	0.97	0.95
		bv	1.29	0.95	0.73	1.94	0.61	0.68	0.91	0.92
		bnv	1.19	0.89	0.73	1.75	0.71	0.73	0.97	0.94
	Ranu Klakah	cb	1.23	0.91	0.74	1.95	0.67	0.70	0.96	0.92
		pb	1.17	0.90	0.77	1.65	0.73	0.73	0.96	0.95
		bv	1.23	0.92	0.73	1.81	0.67	0.74	0.94	0.94
		bnv	1.22	0.90	0.74	1.97	0.68	0.67	0.97	0.94
North maars	Ranu Kering	cb	1.22	0.92	0.74	1.59	0.68	0.79	0.95	0.94
		pb	1.22	0.90	0.73	1.99	0.69	0.72	0.96	0.94
		bv	1.28	0.95	0.74	1.84	0.63	0.71	0.92	0.92
		bnv	1.21	0.90	0.73	1.73	0.70	0.73	0.96	0.93
		ob	1.92	1.23	0.57	2.06	0.32	0.65	0.73	0.74
	Ranu Air	cb	1.23	0.91	0.73	2.01	0.67	0.63	0.94	0.94
		pb	1.18	0.90	0.76	1.57	0.72	0.77	0.96	0.95
		bv	1.24	0.92	0.74	1.93	0.66	0.68	0.94	0.94
		bnv	1.18	0.89	0.77	1.92	0.73	0.66	0.97	0.96
East maars	Outcrop NE Ranu Kembar	cb	1.28	0.97	0.74	1.48	0.61	0.81	0.88	0.93
		pb	1.37	1.00	0.71	2.07	0.55	0.65	0.88	0.92
		bv	1.35	1.01	0.72	1.65	0.55	0.77	0.85	0.91
		bnv	1.32	1.00	0.74	1.64	0.58	0.77	0.87	0.92
	Ranu Segaran	cb	1.27	0.96	0.73	1.59	0.62	0.77	0.91	0.92
		pb	1.27	0.95	0.74	1.90	0.64	0.67	0.92	0.94
		bv	1.33	0.97	0.71	1.93	0.58	0.68	0.89	0.92
		bnv	1.37	1.02	0.74	1.81	0.55	0.69	0.85	0.93

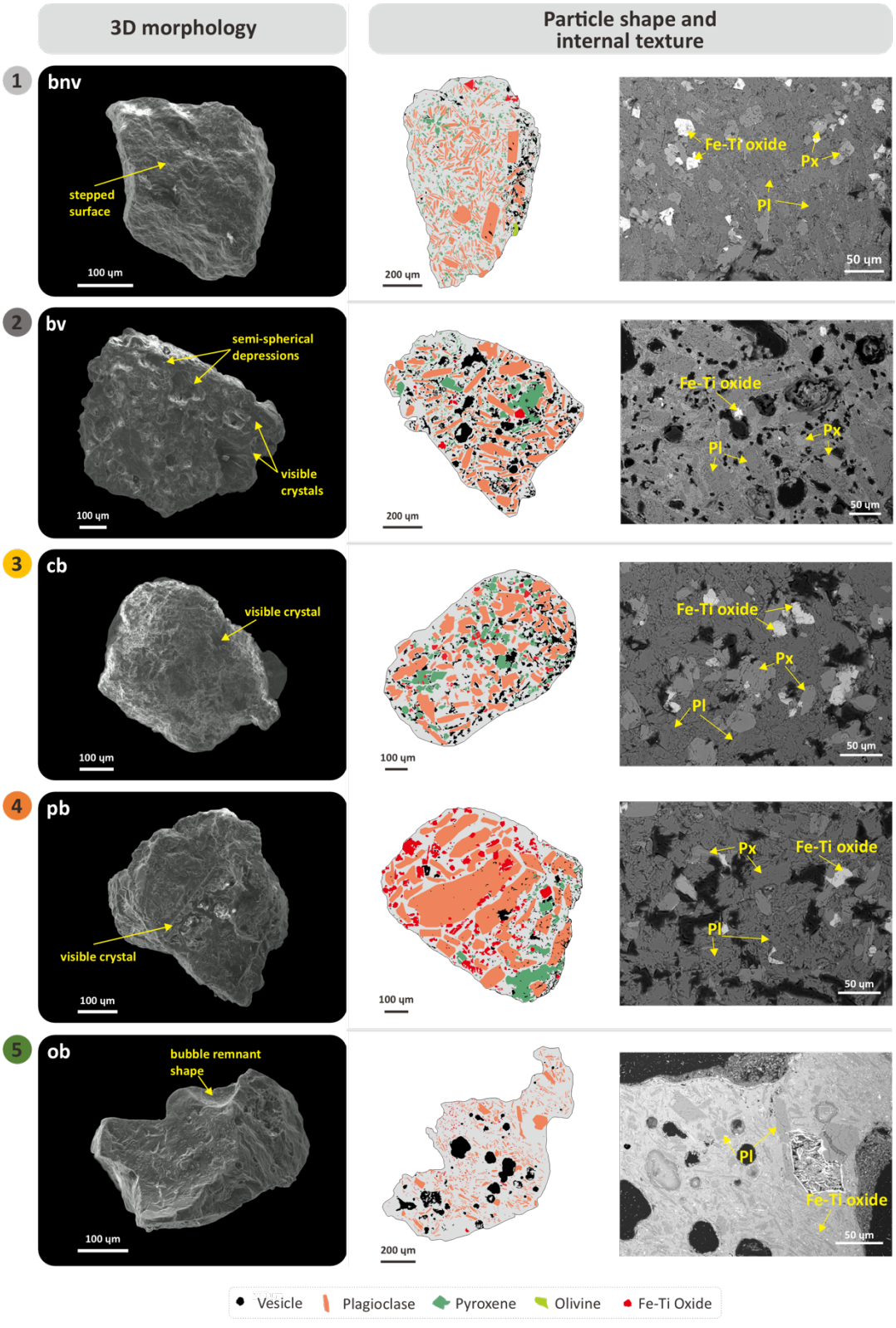

Figure 2. 6. Micro-texture description for juvenile ash classes, including 3D morphology and representative digitized grain backscattered electron (BSE) images with textural features in high magnification (square images) from ash particles in LVF maar complex. The digitized BSE images were used for vesicular and crystal features calculations.

2.3.2c. Ash texture

SEM images taken at 80x to 170x magnification reveal that all five classes of juvenile grains contain glass, crystals, and vesicles, but in variable proportions (Fig. 2.6). Samples from the east maars were excluded from this investigation due to the substantial impact of the weathering process on their textural features. The degree of vesicularity was classified using the vesicularity index of Houghton & Wilson (1989). Key vesicle properties such as vesicularity index, vesicle volume, and vesicle number density are summarized in Table 2.3. Vesicularity is the 2D area percentage of vesicles, while vesicle volume (VV) is the total 3D volume fraction estimated based on modeling vesicle size distributions.

1. ***bnv*** ash particles exhibit a non-to-poorly vesicular (average 7.2%) texture, and their average vesicle volume (VV) is 14.6 vol%. The grains are characterized by small vesicle sizes (long axis: average 57 µm), an average vesicle axial ratio of 0.60, irregular to elongate vesicle shapes, and irregular vesicle edges. These particles' exhibit an average vesicle number density (VND) of 15.6 x 10^4 mm^{-3}. The particles have high crystallinity values ranging from 42% to 58%, with a mean value of 45.6%. The crystals are 65% plagioclase, 28% pyroxene, 5.9% Fe-Ti oxides, and 0.7% olivine.
2. ***bv*** ash particles exhibit the highest degree of vesicularity (values ranging from 19% to 33%) among all investigated grains, with a mean VV of 40.7 vol.%. They show comparatively large vesicle sizes (long axis: average 130.8 µm), an average vesicle axial ratio of 0.63, and spherical to elongate vesicle shapes with coalesced vesicles. The smallest vesicles (less than 5 µm) are commonly distributed along the crystal edges. VND values range from 4 to 33 x 10^4 mm^{-3}. This class of particle has an average crystallinity of 31.5%, with 75% plagioclase, 16% pyroxene, 8.7% Fe-Ti oxides, and 5.3% olivine.

3. ***cb*** and ***p*b** ash exhibit relatively low vesicularity, with average values of 20% and 17%, respectively. Both particle classes have a comparable average VV of 28.7 vol% and 24.7% for *cb* and *pb* particles, respectively. These particles have a relatively large vesicle size (long axis: average 106.4 μm) with an average vesicle axial ratio of 0.58. The vesicles display irregular, amoeboid-to-elongate shapes and irregular edges. The *cb* particles exhibit a VND range of 3 x 10^4 mm^{-3} to 7 x 10^4 mm^{-3}, while the *pb* particles exhibit a VND range of 2 x 10^4 mm^{-3} to 24 x 10^4 mm^{-3}. The average crystallinity of these ash particles is 39.8%, with plagioclase, pyroxene, Fe-Ti oxides, and olivine constituting 46%, 38%, 14%, and 4.3%, respectively.
4. ***ob*** ash is glassier than other ash classes (Fig. 2.6). These grains consist of relatively low-vesicularity particles (average 11%) with an average VV value of 7.9 vol.%. They exhibit spherical to elongate vesicle shapes with a tendency for coalescence. The particles have the largest vesicle (long axis: average 147 μm) with an average vesicle axial ratio value of 0.66. The particles have low VND values ranging between 0.5 and 0.9 x 10^4 mm^{-3}. They display a low average crystallinity of 7.9%, and the crystals consist predominantly of plagioclase (84%) and Fe-Ti oxide (15%) in the groundmass.

In addition to low-magnification texture analysis, we used high-magnification (500x to 1900x) backscattered electron imaging to obtain more detailed information on vesicularity and crystallinity. The results showed a wide range of vesicularity values for the different particle classes, with *bv*, *bnv*, *cb*, *pb*, and *ob* exhibiting average values of 39%, 4.3%, 8.3%, 2.2%, and 2%, respectively. Furthermore, crystallinity measurements varied significantly among the particle classes, with *bv*, *bnv*, *cb*, *pb*, and *ob* displaying average values of 74%, 68%, 57%, 46%, and 27%, respectively.

2.3.2d. Geochemical composition and rheological variation

The analyzed volcanic ash particles from the LVF maar complex exhibit chemical compositions that span a range from picro-basalt to basaltic andesite (41.4–52.9 wt.% SiO_2 and 0.25–1.63 wt.% K_2O; Fig. 2.7a). They are classified as low- to medium-K basalt with high MgO (*cb* + *pb* ash), medium-K picrobasalt to basalt with high MgO (grayish-black ash from east maars), and medium- to high-K basalt to basaltic andesite with moderate to low MgO content (*bv* + *bnv* and *ob* ash), respectively. Each ash class also has a different FeO* (iron total) concentration, gray, *cb-pb*, *bv*, and some portions of *bnv* ash show a relatively decreasing trend towards increasing silica, however, *bnv* and *ob* particles show indications of a relatively flat iron trend towards increasing silica concentration. In addition, the lava fragment samples (north and east lava) are classified as medium- to high-K basalt to basaltic-andesite, while the north scoria cone deposits are medium-K picrobasalt with the lowest SiO_2 (41.4 wt.%).

In stratigraphy, we infer the typical composition of various stratigraphic layers based on the bulk composition of different particle types. As evidenced by their silica concentrations, the geochemical composition of ash classes is relatively stable over time, as shown in Figure 2.8. The brown (*cb* + *pb*) ash particles exhibit low SiO_2, averaging 47.6 wt.% for the west maars and 46.2 wt.% for the north maars. The black ash (*bv* + *bnv*) displays an average silica content of 50.5 wt.% for the west maars and 49.7 wt.% for the north maars. In contrast, the orange ash (*ob*) demonstrates the highest average silica concentration, with 51.5 wt.% for the west maars and 53.2 wt.% for the north maars. Lastly, the grayish-black ash particles obtained from the east maar are characterized by the lowest average SiO_2, which stands at 45.8 wt.%.

Through the utilization of estimates based on observed bulk crystallinity and mineral assemblages, we were able to estimate the eruptive temperature and calculate melt viscosities for the ash particles. Moreover, by taking the observed porosity into account, the bulk rheological properties can be constrained. The black particles (*bv* + *bnv* + *bnv-m*) from the west

and north maars represent average values of silica concentration of 50.7 wt.% (Table 4). They have corresponding average viscosities and liquid temperatures of $10^{3.58}$ Pa.s (~3800 Pa.s) and 1042°C, respectively. The pale-clear brown ash particles (*pb* + *cb*) exhibit lower average values of silica at 46.8 wt.%. They have a lower average viscosity at $10^{2.76}$ Pa.s (~575 Pa.s) and a higher average liquid temperature at 1067°C. Lastly, the *ob* ash particles displayed the highest silica content (average 52.6 wt.%). These particles also have the highest liquid temperature (average 1106°C) and lowest viscosity (average $10^{2.48}$ Pa.s or about 300 Pa.s).

Moreover, we applied crystal content and crystal size distribution to calculate the relative viscosities of ash particles derived from the LVF maar complex. The analysis solely focused on the influence of crystal size on the rheology of the magmatic system without considering the contribution of vesicles (Klein et al., 2018), as done in previous studies of natural samples (e.g. Bagdassarov & Dingwell, 1992). As shown in Figure 2.9, each ash particle class exhibits a distinct trend in terms of crystallinity and relative viscosity. In general, the average values of relative viscosity show an increasing trend for *ob*, *pb*, *bv*, *cb*, and *bnv* ash particles. The *ob* particles exhibit the lowest average value of relative viscosity (1.1), while the *bnv* grains display the highest relative viscosity (average 87.5).

Table 2. 3. The summary of vesicle properties within each class from LVF maar complex.*

Ash Type	Sample	Long axis	Short axis	Average long axis	Length	Width	Average length	Mean *AR*	Median *AR*	Vesicle type	Vesicle images
Clear-brown (***cb***)	1-3 cb	139.4	5.0	20.2	45.9	3.9	10.4	0.57	0.57	Irregular, amoeboid to elongate shapes, coalescence, irregular edges	
	5-12a cb	99.2	5.0	19.8	43.1	3.8	9.5	0.54	0.53		
	13-2 cb	88.0	4.8	17.1	61.0	3.9	9.6	0.61	0.63		
Pale-brown (***pb***)	1-3 pb	173.3	5.2	23.9	94.8	3.8	12.6	0.60	0.60		
	5-12a pb	91.2	5.2	20.4	54.4	4.3	10.5	0.57	0.57		
	13-2 pb	76.2	3.8	10.0	28.5	3.2	5.5	0.61	0.63		
	20-1 pb	77.5	3.5	9.4	42.7	2.9	4.9	0.58	0.58		
Black vesicular (***bv***)	1-3 bv	189.0	3.3	14.7	110.4	2.3	8.7	0.63	0.63	Spherical to elongate shapes, coalescence	
	5-12a bv	130.2	3.1	15.2	86.6	1.7	8.6	0.60	0.59		
	13-2-bv	111.5	5.4	19.9	70.8	4.0	11.7	0.63	0.64		
	20-1 bv	92.7	2.6	12.1	73.1	1.8	7.2	0.64	0.65		
Black non-vesicular (***bnv***)	1-3 bnv	71.5	3.5	11.4	34.0	3.0	6.1	0.62	0.61	Irregular to elongate shapes, irregular edges	
	5-12a bnv	33.8	2.1	6.1	16.8	1.7	3.0	0.58	0.57		
	13-2 bnv	36.9	2.7	8.1	17.9	2.2	4.7	0.63	0.63		
	20-1 bnv	49.1	2.8	8.4	16.0	2.4	4.3	0.58	0.59		
	20-1 bnv	93.5	4.1	13.2	38.8	3.2	7.1	0.61	0.61		
Orange-brown (***ob***)	1-3 ob	151.7	5.5	32.3	81.1	4.5	18.3	0.58	0.58	Spherical shapes, coalescence	
	13-2 ob	142.4	7.0	30.8	110.3	5.7	22.4	0.74	0.79		

*All measurement results in this table are micrometers scale. *AR* means axial ratio.

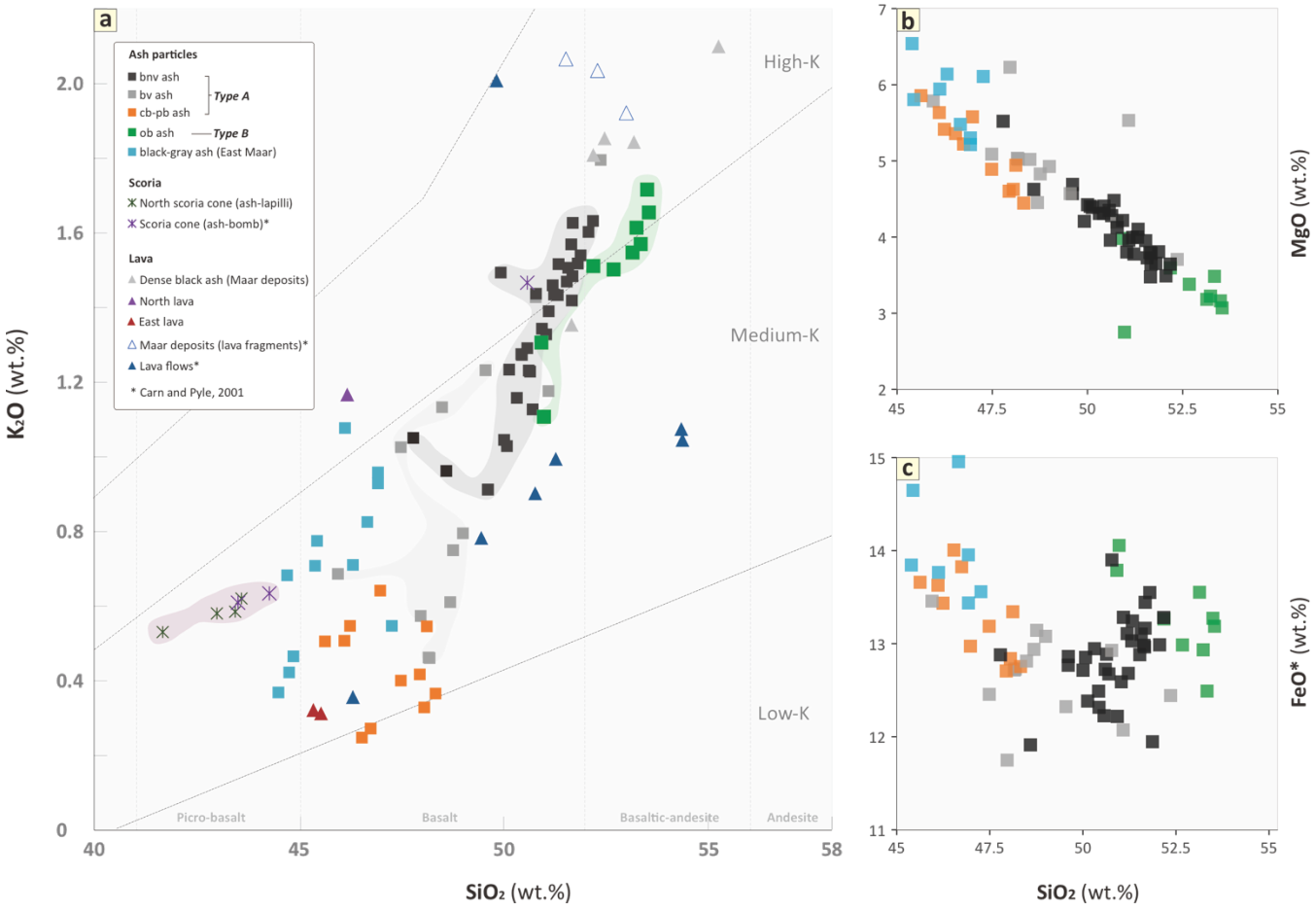

Figure 2. 7. (**a**) Binary plot of K_2O (wt.%) vs SiO_2 (wt.%) for volcanic products in LVF, including volcanic ash from maar deposits, scoria fall deposits, and lavas. The rock series boundary lines are based on Ewart (1982) and Le Maitre et al. (1989). Binary plots of (**b**) MgO (wt.%) vs SiO_2 (wt.%) and (**c**) FeO* (wt.%) vs SiO_2 (wt.%). All the major element compositions presented have been normalized to 100% volatile-free.

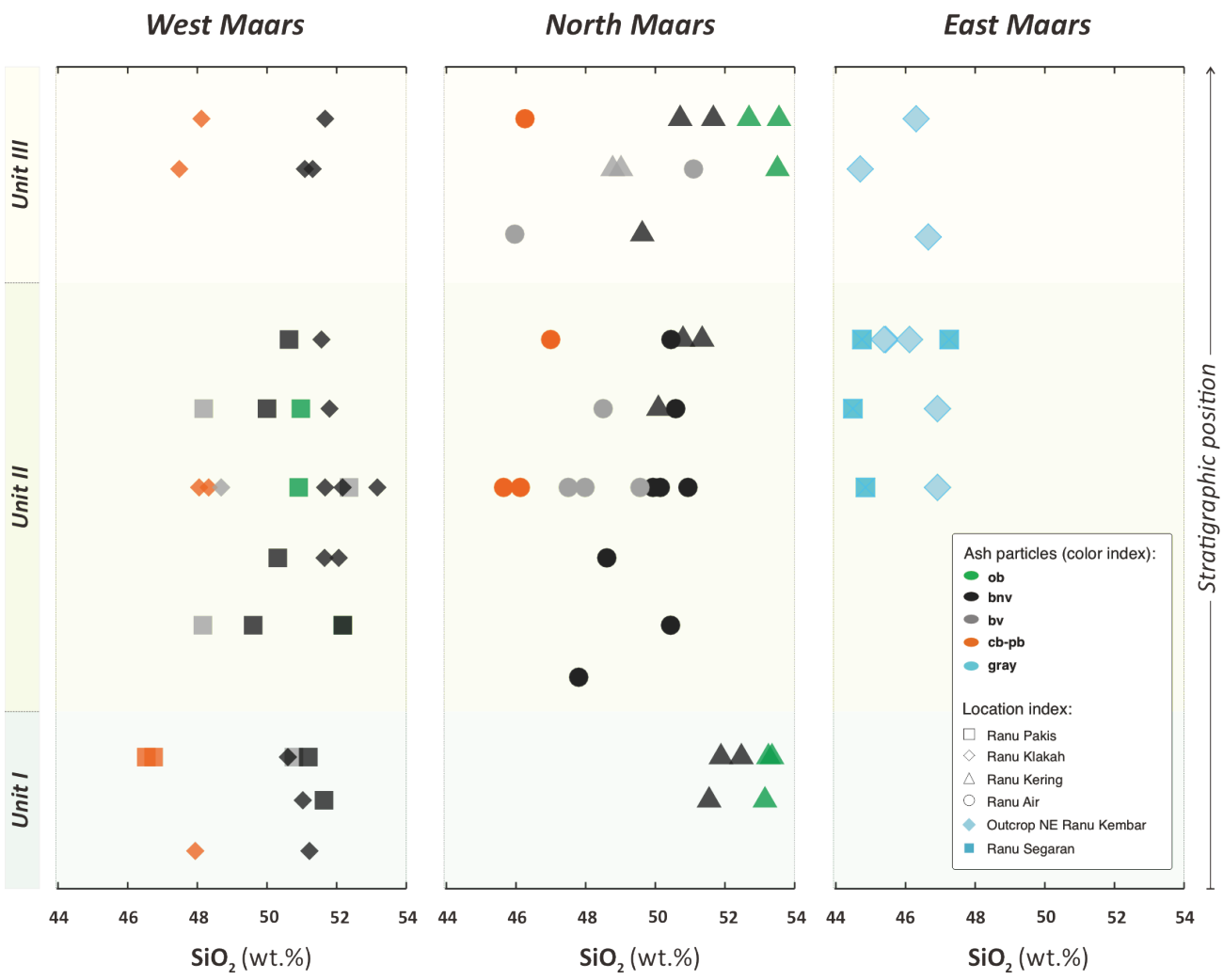

Figure 2. 8. Temporal variation diagrams of SiO_2 (wt.%) content within a single eruption center of LVF maar complex.

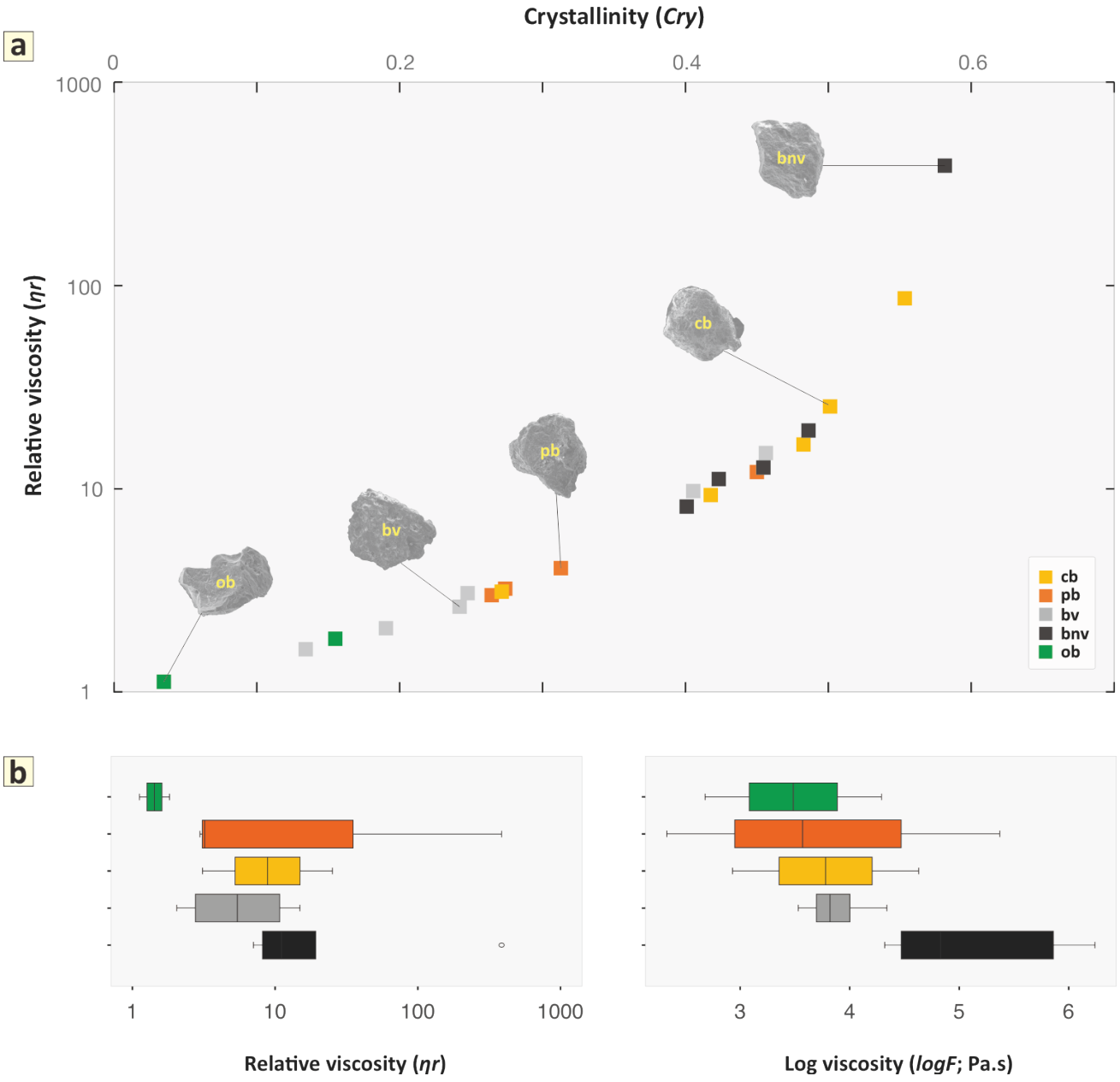

Figure 2. 9. (**a**) Plot of relative viscosity vs. crystallinity of ash particles from the LVF maar complex. Results show an increasing exponential trend from low ratio values of ob ash, bv ash, and pb-cb ash, to high ratio values of bnv ash. (**b**) Comparison of the trend between relative viscosity and log viscosity of each type of ash particle. Both show a negative trend from orange (ob), brown (pb + cb), to black (bv + bnv) ash particles.

2.4. DISCUSSION

The observed vertical stratigraphic successions and variations across the LVF maar locations provide insights into the eruption processes and progression within this maar complex. The lower lithic-rich units containing large meter-scale blocks likely represent the initial explosive vent-opening phase (Fig. 2.2b) (e.g. Lorentz, 1986; Lorentz et al., 2017; Saucedo et al., 2017). The coarse-grained units containing bomb sags may reflect the unsteady explosive eruption (Fig. 2.2c). Progressing upwards, cross-laminated lapilli beds indicate deposition from pyroclastic surges, pointing to oscillations in intensity (Fig. 2.2e). These coarser layers grade into the overlying finer-grained units, marked by extensive accretionary lapilli-bearing ash beds (Fig. 2.2-d-f-g-h). The fine ash and aggregation feature sustained eruption activities from prolonged magma-water interaction during crater development. This matches documented sequences of other maar eruptions globally (e.g. Lorentz, 1986; White & Ross, 2001; Jordan et al., 2013).

The LVF maar ash particles were divided into two distinct types based on their characteristics, namely juvenile A (comprising black vesicular [*bv*], black non-vesicular [*bnv*], clear-brown [*cb*], and pale-brown [*pb*] classes) and juvenile B (consisting of orange-brown [*ob*]) ash particles. Free-crystal (*fc*) and altered (*alt*) ash particles were excluded from the analysis since they may not directly reflect primary magma fragmentation dynamics. However, their abundance within deposits is still characterized. This classification allowed the identification of the two end-members with contrasting properties, including differences in morphology, texture, composition, and rheological characteristics. Specifically, juvenile A ash particles exhibit a commonly blocky shape, high crystallinity, low vesicularity (with small vesicles), lower silica content, and higher viscosity. On the other hand, juvenile B ash particles are irregular in shape and have low crystallinity, low vesicularity (with bigger vesicles), higher

silica content, and lower viscosity. We propose below that this reflects a different fragmentation process or eruption style for type A versus type B particles.

2.4.1. Textural variation of ash particles; ash formation

The ash particles produced by the LVF maar complex eruptions exhibit a diverse range of morphological and textural features. As depicted in Figure 2.10 and Table 2.4, juvenile A particles (*bnv*, *bv*, *cb*, and *pb*) exhibit more complex textural features compared to juvenile B ash particles (*ob*). The *bnv* ash particles have low vesicularity and crystal-rich groundmasses with tiny irregular vesicles. The complex vesicle shapes are considered to be influenced by the presence of crystals. The *bv* ash particles have slightly lower crystallinity, higher vesicularity, and higher vesicle density. The vesicles in these grains predominantly display a spherical to elongate shape, reflecting vesicle nucleation, growth, and coalescence processes. The *cb* and *pb* ash particles, having lower vesicle number densities and irregular bubble shapes, share similar textural properties with low vesicularity and crystalline tachylitic groundmass ash particles described by Murtagh & White (2013), who interpreted them as resulting from trapped volatiles within crystal networks. In contrast, the juvenile B ash particles (*ob*) have a less vesicular and less crystalline occurrence than the juvenile A particles, with a glassier groundmass. They have an unimodal vesicle distribution, indicating a trend of multiple stages of vesicle nucleation, growth, and coalescence (Shea et al., 2010). These particles are thought to be the result of the rapid cooling of magma, which produced abundant microlites of plagioclase and Fe-Ti oxide.

The explosive eruption induced by magma-water interaction (phreatomagmatic eruption) is commonly regarded as the primary factor for ash formation at maar volcanoes, where magma fragmentation implies rapid quenching and water vaporization (Wohletz, 1983; Németh, 2010; White & Valentine, 2016). Based on field observation, pyroclastic deposits, and details of ash particles derived from the LVF maar complex, we infer that this process indeed

played a significant role. The deposits are characterized by a high proportion of fine fragments, cross-bedding, bomb sags, and accretionary lapilli. Many ash particles exhibit blocky and equant shapes as the product of brittle fragmentation due to intense magma-water explosions. However, at Ranu Kering (north maars), ash products often display fluidal-like orange particles (constituting over 10% of the component), suggesting ductile (magmatic) fragmentation for those grains.

Magma that is rich in crystals can undergo brittle fragmentation during rapid deformation (Németh, 2010; Miwa et al., 2013). Blocky morphologies are easier to recognize when dealing with dense (low vesicularity) magma (Heiken & Wohletz, 1985). However, even hot magma with poor crystallinity and low viscosity can undergo brittle fragmentation under intense deformation and rapid cooling during phreatomagmatic eruptions (Zimanowski et al., 1991).

Juvenile A particles exhibit a compact distribution of particle shapes, especially on the *Solidity-Convexity* diagram (Fig. 2.5a−c−e). These phreatomagmatic particles are mostly dense, with few perimeter concavities, resulting in high values of *Convexity* and *Solidity* (> 0.8). Type B particles (class *ob*), interpreted as magmatic, have more vesicles visible on their margins and therefore have lower *Convexity* and *Solidity* values (< 0.8). They also have a lower *Form Factor* value, with a transition at 0.5 (dashed vertical line, Fig. 2.5d). In detail, there is a minor overlap between types A and B, potentially indicating transitional features in a few grains. Within the overall regions, juvenile A particles are slightly more blocky, with higher *Convexity* and *Solidity* values, while juvenile B particles from the north maars are slightly more irregular, with lower values for both parameters.

We utilized hierarchical clustering analysis (Fig. 2.11) to investigate the particle shapes of volcanic deposits from the LVF maar complex using both image particle analysis (IPA) parameters (Dellino & La Volpe, 1996) and the shape parameters of Liu et al. (2015). The

parameters used were *Circularity*, *Rectangularity*, *Compactness*, *Elongation*, *Form Factor*, *Axial Ratio*, *Convexity*, and *Solidity*. The clustering referred to the degree of similarity using the Euclidean distance scale (height) (e.g. Maria & Carey, 2002; 2007; Jordan, 2014; Liu et al., 2015; Dürig et al., 2021). Three clusters of particles are distinguished using this procedure: [1] blocky and equant shapes with smooth (1a) and rough (1b) outlines; [2] blocky to planar, sub-equant to elongate shapes with rough outlines; and [3] irregular shapes with rugged outlines. There is no general correlation between these shape clusters (1a, 1b, 2, and 3) and the particle types defined during componentry (types A and B, with type A subdivided into four classes), as the clusters are based solely on shapes, whereas the componentry types and classes integrate colors, internal textures, etc. However, some trends can be noted. Shape cluster 3 consists only of type B (class *ob*) particles; in these grains, large vesicles (vesicle remnant shape) create a distinct cluster of irregular shapes with rugged outlines. We interpret that the *ob* particles, especially those in cluster 3, were formed by magmatic fragmentation. Type B (class *ob*) grains also appear in shape cluster 2, along with some more irregular and elongate type A grains; in short, cluster 2 has transitional properties between irregular and blocky shapes. Finally, shape clusters 1a and 1b consist almost entirely of type A particles with mostly blocky shapes, which are interpreted as brittle products related to phreatomagmatic fragmentation. Within type A particles, 84% are in shape clusters 1a and 1b (with mostly block shapes), and 16% are in shape cluster 2 (with sub-equant shapes). Within juvenile B particles, 54% are in shape cluster 2, and 36% are in shape cluster 3. Our results are consistent with previous studies that have shown that a single eruption can produce a wide range of particle morphologies (e.g. Wohletz, 1983; Sheridan & Wohletz, 1983; Dellino & Liotino, 2002; Mattsson, 2010). Even though the characteristics are different, the ash particles from the LVF maar complex show a clear distribution of the most common shapes (clusters 1a, 1b, and 2). The clustering analysis method we employed is more effective in identifying different particle shapes than binary diagrams,

and can be applied to other volcanic deposits to further our understanding of the eruption mechanisms and processes.

2.4.2. Integration of textural features and geochemical compositions

Klein et al. (2018) determined the rheological properties of natural mafic to intermediate samples by analyzing the crystal-size distribution of vesicle-free magma. The results showed that samples with low crystallinity would have lower relative viscosity and vice versa (see Fig. 3d in Klein et al., 2018; Mader et al., 2013). In general, each class of ash particles in the LVF maar complex has its range of crystallinity. The crystallinity relatively increases from orange to black to brown ash, which is also how their relative viscosities change (Fig. 2.9). More specifically, we investigated the implications and relationship of relative viscosity (ηr) and bulk viscosity ($logF$) to ash particle shape and morphology. As shown in Figure 2.9a and 2.9b, both relative and bulk viscosities have similar decreasing values from *bnv* to *cb* to *ob* particles. The relatively higher viscosity of blocky juvenile A (*bv* + *bnv* + *cp* + *pb*) particles compared to juvenile B (*ob*) particles indicates a more active crystallization process. However, the *bv* particles, which contain lower silica content and have a lower crystallinity than *bnv* particles, have a slightly lower viscosity. Despite their long-range viscosities and relatively low silica content, the brown particles (*cb* + *pb*) display morphological similarities in the form of blocky to sub-round shapes, as shown in the shape distribution ratio in Figure 2.11. All four classes of type A particles (*bv*, *bnv*, *cp*, and *pb*) are evenly represented in shape cluster 1, which has the blockiest shape. These observations suggest that within phreatomagmatic eruptions, magma parcels with slightly different cooling histories and/or geochemical compositions yield variable textures (bubbles and crystals) and rheological properties, resulting in the different type A component classes in the LVF maars. Yet these magma parcels underwent the same type of fragmentation, resulting in relatively similar shapes (manifested by clusters 1 and 2) regardless of cooling history or geochemical composition. The type B juvenile particles, on the

other hand, appear to be from a distinct parcel of magma unique to the northern maars, with higher silica, hotter temperatures, fewer crystals, and larger bubbles, which fragmented into irregular-fluidal shapes, either because these less viscous particles had sufficient time to relax after phreatomagmatic fragmentation or because they underwent magmatic fragmentation.

Principal Component Analysis (PCA) has been applied to morphometric parameters in previous studies by Maria & Carey (2002; 2007) and Nurfiani & de Maisonneuve (2018) to investigate eruption styles and depositional processes (e.g. Grímsvötn [hydromagmatic fragmentation] and Katla [magmatic fragmentation]; Mt. Helens 1980 and Tambora 1815 fall, surge, and flow; Surtsey 1963−64, Pacific deep-water seamount; Iwodake, Merapi 2013, and Kelud). Using PCA, we explored the relationship between textural characteristics, rheological properties, and geochemical composition on the morphology of 16 representative samples of juvenile A and B (average values) from the LVF maar complex (Fig. 2.12). To avoid improper mixing of size fractions (125−250 μm grains used for morphology and textural analysis; 0.5−1 mm used for geochemical analysis) and enable direct comparison of the clustering based on each dataset independently. We plotted the first two principal components (PC1 and PC2) separately from each PCA variable (morphometric, morphometric + textural, and geochemistry). Each ash particle class (as defined during componentry) plots in distinct areas on the PC1-PC2 using morphometric (Fig. 2.12a) and morphometric + textural (Fig. 2.12b) variables. Juvenile B particles are interpreted as having a magmatic-like origin, indicating that *Circularity*, *Rectangularity,* and *Elongation* (as well as other morphometric parameters) are among the most discriminating aspects of these grains, which are also geochemically evolved. The juvenile A grains, interpreted as phreatomagmatic, were discriminated by *Convexity*, *Compactness*, *Solidity*, *Form Factor*, and *Aspect Ratio*. Geochemically, they are various in composition, but each class has distinct characteristics (Fig. 2.7a−c and Fig. 2.12c). Within juvenile A grains, the PC2 axis using shape and textural variables (Fig. 2.12b) helps

differentiate the variety of classes quantitatively. The PC2 axis is more influenced than the PC1 axis by vesicles (vesicularity, VND), crystals, and viscosity. At the relatively low PC2 end of the spectrum, the *bnv* grains have relatively higher viscosities, more crystals, are more dense and blocky, and have stepped microcrystalline surfaces. At the high end of the PC2 spectrum, *cb* and *pb* particles have relatively lower viscosities, fewer crystals, higher vesicularity, and a mostly blocky shape with an irregular to rough surface (*cb* + *pb* + *bv*). Two grains, one *cb* and one *pb*, are plotted at the low end of the PC2 axis, which may be strongly affected by high crystal content (Table 2.4; *5-12a cb1* and *20-1 pb1* samples). As mentioned in the clustering result, particularly in juvenile type A (phreatomagmatic particles) with mostly blocky shapes, their broad geochemical compositions result in variable textures, rheological properties, and/or cooling histories that may not be as crucial aspects as the fragmentation process to the shapes of this ash type. In addition, the PCA analysis conducted on morphometric and textural parameters (as shown in Figure 2.12b) offers a quantitative approach to distinguish between distinct ash classes by considering their fragmentation processes and surface characteristics.

Our integrated analytical approach reveals that while the juvenile ash types exhibit variability in composition, their shape distributions principally reflect the predominant brittle fragmentation style of phreatomagmatism. The blocky morphologies of most juvenile A particles, despite their geochemical diversity, indicate that phreatomagmatic processes were the primary control over their shapes. In contrast, the irregular morphology of the juvenile B particles signifies a distinct magmatic fragmentation origin. These findings demonstrate that in the LVF maar complex, variable magma properties yield diverse ash components, yet fragmentation dynamics govern pyroclast shapes.

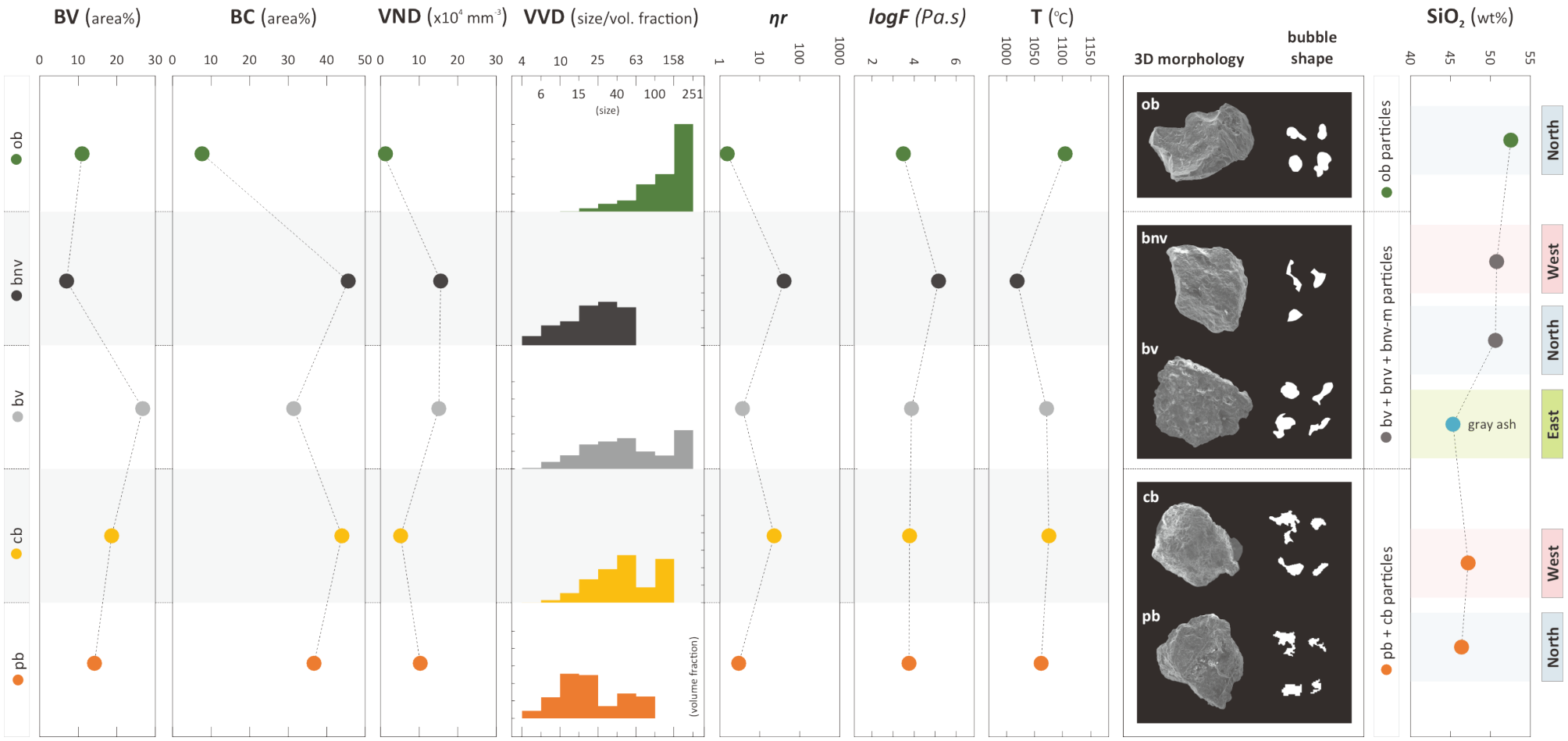

Figure 2. 10. Summary of textural features and morphology of ash particles from the LVF maar complex with their corresponding rheological variations. The variables presented are average values from representative ash particle types, including BV (bulk vesicularity), BC (bulk crystallinity), VND (vesicle number density), VVD (vesicle volume distribution), ηr (relative viscosities), logF (log viscosities), T (liquid/magma temperature), SiO_2 (silica content).

Table 2. 4. Summary of vesicle features, bulk crystallinity, and crystal fraction distribution of ash classes from the LVF maar complex.*

Ash type	Sample	Vesicle features					Cry	Crystal Fraction %				*ηr*	T (°C)	*logF* (Pa.s)	Average SiO_2 (wt%)
		n	VND	BV%	VV%	Av. VV%		Px	Pl	Fe-Ti	Ol				
bv	1-3 bv4	819	11.5	27 [31.5]	44.4	40.7	40 [78.4]	11.2	83.9	3.8	1.1	9.7	1076	2.75	50.7
	5-12a bv2	560	11.9	28	41.5		43	25	72.1	2.8	-	14.9	1048	2.53	
	13-2 bv3	366	4.16	19 [48.1]	28.9		18 [69.9]	14.2	52.3	23.9	9.5	2.1	1093	2.89	
	20-1 bv3	925	33	33	47.9		25	-	95.5	4.3	-	3.1	1069	3.34	
bnv	1-3 bnv-m3	252	9.26	8 [2.5]	14.8	12.3	42 [66.9]	25.6	69.6	4	0.7	11.1	1060	3.47	
	5-12 bnv-m2	156	24	3	6.4		49	35.9	57	7	-	19.3	979	4.86	
	13-2 bnv-m1	506	21.1	6 [4.8]	9.3		40 [69.6]	17.9	72.3	9.8	-	8.2	1039	3.83	
	20-1 bnv-m1	-	-	-	-		58	13.3	84.4	2.2	-	386.3	951	5.24	
	20-1 bnv1	261	8.07	11	18.8		39	49.9	43.3	6.8	-	7.0	1063	3.32	
cb	1-3 cb2	280	3.87	18	28.4	28.7	27	68.2	19.8	12	-	3.1	1114	1.93	46.8
	5-12a cb1	271	7.02	22	32.3		50	25.7	67.9	6.4	-	25.3	1038	3.63	
	13-2 cb4	272	4.62	16 [3.6]	25.5		55 [57.1]	22.7	69.4	7.9	-	86.3	-	-	
pb	1-3 pb2	189	2.56	24	45.6	24.7	26	55.7	28.5	15.8	-	3.0	1105	1.33	
	5-12a pb1	258	3.81	17	25.3		27	52	17.9	30.1	-	3.2	1084	2.57	
	13-2 pb1	352	10.6	5 [1.8]	9.2		31 [47.6]	35.7	46.4	13.6	4.3	4.0	-	-	
	20-1 pb1	421	24.4	11	18.6		63	10	74.8	15.2	-	-	995	4.37	
ob	1-3 ob2	60	0.92	19	20.2	17.3	0.3	-	100	-	-	1.1	1138	1.68	52.6
	13-2 ob5	57	0.55	3 [2]	14.4		15 [27.8]	-	84.2	15.8	-	1.8	1074	3.29	

*n = number of vesicles; VND = vesicle number density (x10^4 mm^{-3}); BV% = bulk vesicularity [high magnification]; VV% = vesicle volume; Av.VV% = average vesicle volume; Cry% = bulk crystallinity [high magnification]; Pyroxene (Px); Plagioclase (Pl); Fe-Ti oxides mineral (Fe-Ti); Olivine (Ol); SiO_2 = average silica content. The estimated liquid temperature (T) and log viscosity variations (l*ogF*) of LVF maar complex magma are referred from the geochemical composition of the ash particle types. They were calculated using *PELE* software with the assumption of 1.5% H_2O content, fO_2 at the QFM buffer, and fractional crystallization condition. The temperature and viscosity were obtained from crystallinity and mineral assemblages that were similar to those in the *PELE* calculation and textural analysis result. *ηr* = relative viscosity.

2.4.3. Composition of ash particles

In this study, we conducted a geochemical analysis of each class of ash particles to better constrain their origins. By integrating the results of the textural identification with the geochemical data, we were able to infer that the ash particles were derived from a heterogeneous magma source (as depicted in Fig. 2.7a–c). Our findings suggest that brown (*cb-pb*) (north and west maars) and grayish-black (east maars) ash were formed from the least evolved of low-K to medium-K basaltic magma. The compositions of the black ash (*bv* + *bnv*) from the north and west maars were also similar, originating from medium-K to high-K more evolved basalt to basaltic andesite magma. On the other hand, orange-brown (*ob*) ash particles were found to be derived from a distinctly different batch of magma with a high silica content (primarily in high-K basaltic andesite). The mineral assemblages of the *ob* class particles were also distinct, with pyroxene and olivine minerals being uncommon (Fig. 2.6). An anomalous iron trend in the PCA geochemistry (Fig. 2.12c) plot towards the low end of the PC2 axis and two different trends of iron concentration versus silica enrichment indicate that there is a specific geochemical pattern between gray + *cb-pb* and *bv* + *bnv* + *ob* (e.g. different crystal fractionation phases). A possible reason for the steep decreasing trend in gray, *cb-pb*, and *bv* particles towards increasing silica is more effective crystallization of the Fe-Ti oxide minerals (average Fe-Ti oxide abundance in *cb-pb* [14.6%] is higher than in *bv* [8.7%], *bnv* [5.9%], and *ob* [7.9%] ash particles (Table 2.4). The geochemical data from LVF may relate to the magmatic evolution towards a more silicic composition during the progression of eruptions, as noted in other mafic volcanic systems (e.g. Gaunt et al., 2016). Additionally, the geochemical data from the north scoria cone deposits (average SiO_2 at 42.3%; medium-K picrobasaltic) and east lava (Ranu Agung; average SiO_2 at 45.4%; medium-K basalt) indicate that they possessed a less evolved composition and could be comparable to the initial magma composition that fed the maar complex of the study area. Further investigation is required into the geochemistry,

trace elements, and mineral chemistry of ash particles, lavas, and scoria cone deposits to shed more light on these issues.

2.5. CONCLUSSION

1. This study presents a comprehensive analysis of ash particles produced by maar eruptions in the Lamongan Volcanic Field (LVF), providing the first detailed observations of their characteristics. The ash particles can be classified into seven classes based on componentry data and their relation to the maar eruption, which itself can be divided into two main categories: juvenile particles (composed of juvenile A [black non-vesicular, black vesicular, clear-brown, pale-brown] and juvenile B [orange-brown]) and other (free crystals and altered grains). The observed juvenile A particles mostly exhibit typical blocky to planar shapes resulting from phreatomagmatic fragmentation of magma, which produced low vesicularity particles with highly crystalline groundmasses and clear-brown to opaque (brown-black) colors. In contrast, juvenile B particles (*ob*) have irregular shapes and were produced by magmatic-like fragmentation. The calculated magma viscosity relatively increases from orange (*ob*) to brown (*cp* + *pb*) to black ash particles (*bv* + *bnv*) due to magma composition and degree of crystallization.
2. According to the clustering analysis, phreatomagmatic juvenile A particles predominantly have blocky shapes (84% in clusters 1a and 1b) and sub-equant shapes (16% in cluster 2). On the other hand, magmatic-like fragmentation produced mostly irregular juvenile B particles with sub-equant shapes (54% in cluster 2) and irregular shapes (36% in cluster 3). From PCA analysis results using morphological parameters, we infer the likely fragmentation process of the ash particles from the LVF maar complex. Most juvenile A particles, despite their geochemical diversity, exhibited

blocky shapes, indicating the influence of phreatomagmatic processes. In contrast, juvenile B particles displayed irregular shapes, suggesting a distinct magmatic fragmentation origin. These findings demonstrate how fragmentation dynamics govern pyroclast shapes in the LVF maar complex, despite varying magma properties.

3. Integrated textural and geochemical analyses show that the LVF maar pyroclasts come from either a mixture of different types of magma or from several batches of magma with slightly different compositions and/or cooling histories. The juvenile type A particles indicate various degrees of differentiation, with brown ash (*cb* + *pb*) (north and west maars) and grayish-black ash (east maars) representing the least evolved basaltic magmas, while the black ash particles (*bv* + *bnv*; north and west maars) indicating more evolved basaltic to basaltic andesite magma. In contrast, juvenile B (*ob* ash particles) with a slightly higher silica content implies further evolution towards basaltic andesite composition. Furthermore, the north scoria cone deposits (average SiO_2 42.3%; picrobasaltic) and east lava (Ranu Agung; average SiO_2 45.4%; basaltic) exhibit the most mafic-primitive compositions, which could be comparable to the initial magma composition that feeds the maar complex of LVF.

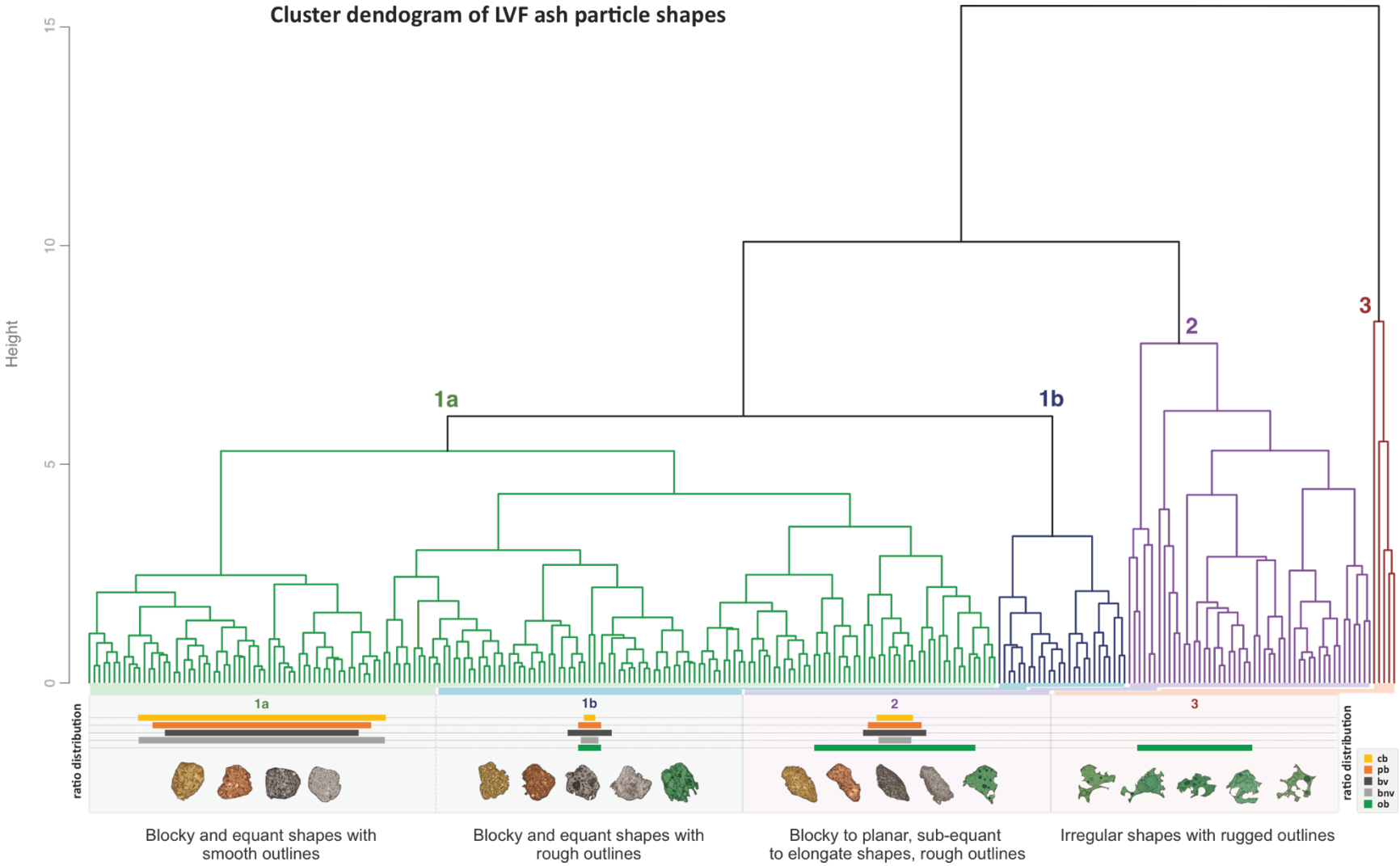

Figure 2. 11. Cluster dendrogram for ash particles from LVF maar complex (n=266 particles; bnv=67, pb=60, bv=101, cb=24, ob=13). The clustering is based on variables of particle analysis (IPA) parameters (Dellino & La Volpe, 1996) and shape parameters (Liu et al., 2015). The variables used were Circularity, Rectangularity, Compactness, Elongation, Form Factor, Axial Ratio, Convexity, and Solidity. The images below the cluster show the ratio distribution of the componentry classes and representative particles (from left to right, the images show a change in shape from blocky and equant to sub-equant and elongate to irregular, respectively).

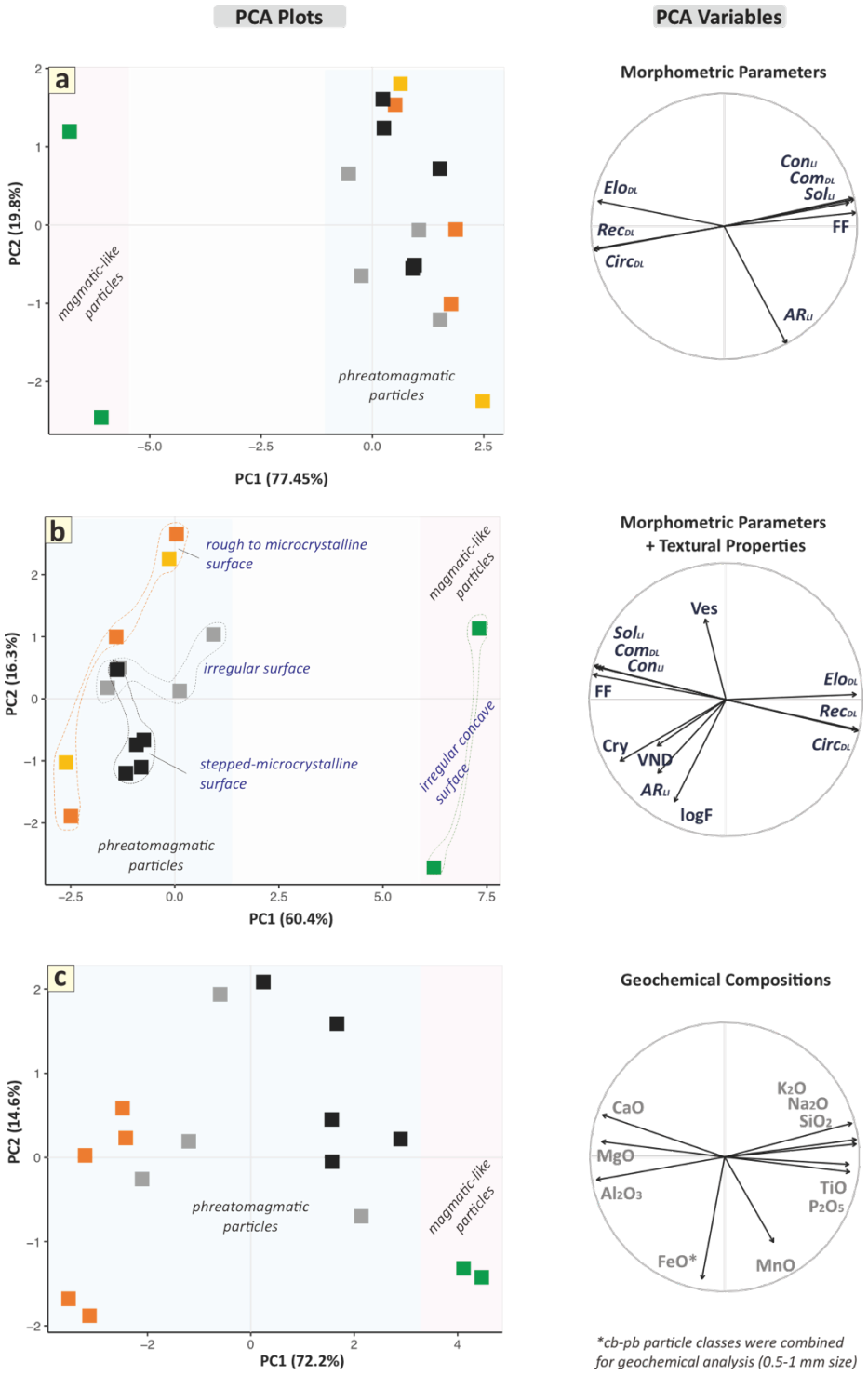

Figure 2. 12. Principal Component Analysis (PCA) of integrated multivariable parameters of ash particles from LVF maar complex, including morphometric parameters (**a**), morphometric parameters + textural features (**b**), and geochemistry (**c**). The a and b plots show a clear distinction between particle types, with each plot in the quadrans according to their dominance factors. For example, juvenile B ash particles are located at the high PC1 axis (plot b) while juvenile A particles are located in the opposite area. Furthermore, phreatomagmatic ash particle (juvenile A) can be divided based on the PC2 axis (mostly by textural variables) in plot b, which has relatively low values in bnv ash, moderate values in bv ash, and moderate to high values in cb + pb ash. Two samples of cb-pb plotted in the low values of the PC2 axis (plot b) related to the high crystallinity feature.

2.6. REFERENCE

Büttner, R., Dellino, P., la Volpe, L., Lorenz, V., & Zimanowski, B. (2002). Thermohydraulic explosions in phreatomagmatic eruptions as evidenced by the comparison between pyroclasts and products from Molten Fuel Coolant Interaction experiments. *Journal of Geophysical Research: Solid Earth*, *107*(B11), ECV 5-1-ECV 5-14. https://doi.org/10.1029/2001jb000511

Bagdassarov, N. S., & Dingwell, D. B. (1992). A rheological investigation of vesicular rhyolite. In *Journal of Volcanology and Geothermal Research* (Vol. 50).

Carn, S. A. (2000). The Lamongan volcanic field, East Java, Indonesia: Physical volcanology, historic activity and hazards. *Journal of Volcanology and Geothermal Research*, *95*(1–4), 81–108. https://doi.org/10.1016/S0377-0273(99)00114-6

Carn, S. A., & Pyle, D. M. (2001). Petrology and geochemistry of the Lamongan volcanic field, East Java, Indonesia: Primitive Sunda arc magmas in an extensional tectonic setting? *Journal of Petrology*, *42*(9), 1643–1683. https://doi.org/10.1093/petrology/42.9.1643

Cassidy, M., Castro, J. M., Helo, C., Troll, V. R., Deegan, F. M., Muir, D., Neave, D. A., & Mueller, S. P. (2016). Volatile dilution during magma injections and implications for volcano explosivity. *Geology*, *44*(12), 1027–1030. https://doi.org/10.1130/G38411.1

Cioni, R., D'Oriano, C., & Bertagnini, A. (2008). Fingerprinting ash deposits of small scale eruptions by their physical and textural features. *Journal of Volcanology and Geothermal Research*, *177*(1), 277–287. https://doi.org/10.1016/j.jvolgeores.2008.06.003

Comida, P. P., Ross, P. S., Dürig, T., White, J. D. L., & Lefebvre, N. (2022). Standardized analysis of juvenile pyroclasts in comparative studies of primary magma fragmentation: 2. Choice of size fraction and method optimization for particle cross-sections. *Bulletin of Volcanology*, *84*(1), 1–24. https://doi.org/10.1007/s00445-021-01517-5

Dellino, P., & Volpe, L. la. (1996). Image processing analysis in reconstructing fragmentation and transportation mechanisms of pyroclastic deposits. The case of Monte Pilato-Rocche Rosse eruptions, Lipari (Aeolian islands, Italy). In *Journal of Volcanology and Geothermal Research* (Vol. 7).

Dellino, P., Liotino, G., 2002. The fractal and multifractal dimension of volcanic ash particles contour: a test study on the utility and volcanological relevance. J. *Journal of Volcanology and Geothermal Research*. *113*(1), 1–18.

Dürig, T., Bowman, M. H., White, J. D. L., Murch, A., Mele, D., Verolino, A., & Dellino, P. (2018). Particle shape analyzer Partisan - An open source tool for multi-standard two-dimensional particle morphometry analysis. *Annals of Geophysics*, *61*(6). https://doi.org/10.4401/ag-7865

Dürig, T., Ross, P. S., Dellino, P., White, J. D. L., Mele, D., & Comida, P. P. (2021). A review of statistical tools for morphometric analysis of juvenile pyroclasts. In *Bulletin of Volcanology* (Vol. 83, Issue 11). Springer Science and Business Media Deutschland GmbH. https://doi.org/10.1007/s00445-021-01500-0

D'Oriano, C., Cioni, R., Bertagnini, A., Andronico, D., & Cole, P. D. (2011). Dynamics of ash-dominated eruptions at Vesuvius: The post-512 AD AS1a event. *Bulletin of Volcanology*, *73*(6), 699–715. https://doi.org/10.1007/s00445-010-0432-1

D'Oriano, C., Bertagnini, A., Cioni, R., & Pompilio, M. (2014). Identifying recycled ash in basaltic eruptions. *Scientific Reports*, *4*. https://doi.org/10.1038/srep05851

Gaunt, H. E., Bernard, B., Hidalgo, S., Proaño, A., Wright, H., Mothes, P., Criollo, E., & Kueppers, U. (2016). Juvenile magma recognition and eruptive dynamics inferred from the analysis of ash time series: The 2015 reawakening of Cotopaxi volcano. *Journal of Volcanology and Geothermal Research*, *328*, 134–146. https://doi.org/10.1016/j.jvolgeores.2016.10.013

Graettinger, A. H. (2018). Trends in maar crater size and shape using the global Maar Volcano Location and Shape (MaarVLS) database. *Journal of Volcanology and Geothermal Research*, *357*, 1–13. https://doi.org/10.1016/j.jvolgeores.2018.04.002

Heiken, G. (1978). Characteristics of tephra from cinder cone, Lassen volcanic National Park, California. *Bulletin Volcanologique*, *41*(2), 119–130. https://doi.org/10.1007/BF02597025

Heiken, G., & Wohletz, K. (1985). *Volcanic ash*. University Presses of California, Columbia and Princeton.

Higgins, M.D. (2000). Measurement of Crystal Size Distributions. *American Mineralogist, 85*, 1105-1116.

Higgins, M.D. (2002) Closure in crystal size distributions (CSD), verification of CSD calculations, and the significance of CSD fans. *American Mineralogist, 87*, 171-175.

Higgins, M. D., & Chandrasekharam, D. (2007). Nature of sub-volcanic magma chambers, deccan province, India: Evidence from quantitative textural analysis of plagioclase megacrysts in the Giant Plagioclase Basalts. *Journal of Petrology*, *48*(5), 885–900. https://doi.org/10.1093/petrology/egm005

Hornby, A., Kueppers, U., Maurer, B., Poetsch, C., & Dingwell, D. (2020). Experimental constraints on volcanic ash generation and clast morphometrics in pyroclastic density currents and granular flows. *Volcanica,* *3*(2), 263–283. https://doi.org/10.30909/vol.03.02.263283

Houghton, B. F., & Wilson, C. J. N., (1989). A vesicularity index for pyroclastic deposits. *Bulletin of Volcanology, 51*, 451-462.

Jordan, S. C., Dürig, T., Cas, R. A. F., & Zimanowski, B. (2014). Processes controlling the shape of ash particles: Results of statistical IPA. *Journal of Volcanology and Geothermal Research*, *288*, 19–27. https://doi.org/10.1016/j.jvolgeores.2014.09.012

Jordan, S. C., & Hayman, P. (2013). *Factors controlling the formation of a very large maar volcano and the fragmentation process in phreatomagmatic eruptions: Lake Purrumbete Maar, southeastern Australia*.

Klein, J., Mueller, S. P., Helo, C., Schweitzer, S., Gurioli, L., & Castro, J. M. (2018). An expanded model and application of the combined effect of crystal-size distribution and crystal shape on the relative viscosity of magmas. *Journal of Volcanology and Geothermal Research*, *357*, 128–133. https://doi.org/10.1016/j.jvolgeores.2018.04.018

Kueppers, U., Putz, C., Spieler, O., & Dingwell, D. B. (2012). Abrasion in pyroclastic density currents: Insights from tumbling experiments. *Physics and Chemistry of the Earth*, *45–46*, 33–39. https://doi.org/10.1016/j.pce.2011.09.002

Liu, E. J., Cashman, K. v., & Rust, A. C. (2015). Optimising shape analysis to quantify volcanic ash morphology. *GeoResJ*, *8*, 14–30. https://doi.org/10.1016/j.grj.2015.09.001

Lorenz, V. (1986). *On the growth of maars and diatremes and its relevance to the formation of tuff rings* (Vol. 48).

Lorenz, V., Suhr, P., & Suhr, S. (2017). Phreatomagmatic maar-diatreme volcanoes and their incremental growth: A model. In *Geological Society Special Publication* (Vol. 446, Issue 1, pp. 29–59). Geological Society of London. https://doi.org/10.1144/SP446.4

Mader, H.M., Llewellin, E.W., Muller, S.P., The Rheology of Two-Phase Magmas: A Review and Analysis, *Journal of Volcanology and Geothermal Research* (2013), https://doi.org/10.1016/j.jvolgeores.2013.02.014

Maria, A., & Carey, S. (2002). Using fractal analysis to quantitatively characterize the shapes of volcanic particles. *Journal of Geophysical Research: Solid Earth*, *107*(B11), ECV 7-1-ECV 7-17. https://doi.org/10.1029/2001jb000822

Maria, A., & Carey, S. (2007). Quantitative discrimination of magma fragmentation and pyroclastic transport processes using the fractal spectrum technique. *Journal of Volcanology and Geothermal Research*, *161*(3), 234–246. https://doi.org/10.1016/j.jvolgeores.2006.12.006

Manga, M., Patel, A., & Dufek, J. (2011). Rounding of pumice clasts during transport: Field measurements and laboratory studies. *Bulletin of Volcanology*, *73*(3), 321–333. https://doi.org/10.1007/s00445-010-0411-6

Mattsson, H. B. (2010). Textural variation in juvenile pyroclasts from an emergent, Surtseyan-type, volcanic eruption: The Capelas tuff cone, São Miguel (Azores). *Journal of Volcanology and Geothermal Research*, *189*(1–2), 81–91. https://doi.org/10.1016/j.jvolgeores.2009.10.007

Miwa, T., Geshi, N., & Shinohara, H. (2013). Temporal variation in volcanic ash texture during a vulcanian eruption at the sakurajima volcano, Japan. *Journal of Volcanology and Geothermal Research*, *260*, 80–89. https://doi.org/10.1016/j.jvolgeores.2013.05.010

Murtagh, R. M., & White, J. D. L. (2013). Pyroclast characteristics of a subaqueous to emergent Surtseyan eruption, black point volcano, california. *Journal of Volcanology and Geothermal Research*, *267*, 75–91. https://doi.org/10.1016/j.jvolgeores.2013.08.015

Morales Volosín, S., & Risso, C. (2019). El Pozo Volcanic Complex: Evolution of a group of maars, central Mendoza province, Argentina. *Journal of Volcanology and Geothermal Research*, *371*, 177–191. https://doi.org/10.1016/j.jvolgeores.2019.01.005

Németh, K. (2010). Volcanic glass textures, shape characteristics and compositions of phreatomagmatic rock units from the Western Hungarian monogenetic volcanic fields and their implications for magma fragmentation. *Central European Journal of Geosciences*, *2*(3), 399–419. https://doi.org/10.2478/v10085-010-0015-6

Németh, K., & Kósik, S. (2020). Review of explosive hydrovolcanism. In *Geosciences (Switzerland)* (Vol. 10, Issue 2). MDPI AG. https://doi.org/10.3390/geosciences10020044

Noguchi, S., Toramaru, A., & Nakada, S. (2008). Relation between microlite textures and discharge rate during the 1991-1995 eruptions at Unzen, Japan. *Journal of Volcanology and Geothermal Research*, *175*(1–2), 141–155. https://doi.org/10.1016/j.jvolgeores.2008.03.025

Nurfiani, D., & Bouvet de Maisonneuve, C. (2018). Furthering the investigation of eruption styles through quantitative shape analyses of volcanic ash particles. *Journal of Volcanology and Geothermal Research*, *354*, 102–114. https://doi.org/10.1016/j.jvolgeores.2017.12.001

Rausch, J., Grobéty, B., & Vonlanthen, P. (2015). Eifel maars: Quantitative shape characterization of juvenile ash particles (Eifel Volcanic Field, Germany). *Journal of Volcanology and Geothermal Research*, *291*, 86–100. https://doi.org/10.1016/j.jvolgeores.2014.11.008

Ross, P. S., & White, J. D. L. (2012). Quantification of vesicle characteristics in some diatreme-filling deposits, and the explosivity levels of magma-water interactions within diatremes. *Journal of Volcanology and Geothermal Research*, *245–246*, 55–67. https://doi.org/10.1016/j.jvolgeores.2012.07.006

Ross, P. S., Dürig, T., Comida, P. P., Lefebvre, N., White, J. D. L., Andronico, D., Thivet, S., Eychenne, J., & Gurioli, L. (2022). Standardized analysis of juvenile pyroclasts in

comparative studies of primary magma fragmentation; 1. Overview and workflow. *Bulletin of Volcanology*, *84*(1), 1–29. https://doi.org/10.1007/s00445-021-01516-6

Pardo, N., Cronin, S. J., Németh, K., Brenna, M., Schipper, C. I., Breard, E., White, J. D. L., Procter, J., Stewart, B., Agustín-Flores, J., Moebis, A., Zernack, A., Kereszturi, G., Lube, G., Auer, A., Neall, V., & Wallace, C. (2014). Perils in distinguishing phreatic from phreatomagmatic ash; insights into the eruption mechanisms of the 6 August 2012 Mt. Tongariro eruption, New Zealand. *Journal of Volcanology and Geothermal Research*, *286*, 397–414. https://doi.org/10.1016/j.jvolgeores.2014.05.001

Proussevitch, A. A., Sahagian, D. L., & Carlson, W. D. (2007). Statistical analysis of bubble and crystal size distributions: Application to Colorado Plateau basalts. *Journal of Volcanology and Geothermal Research*, *164*(3), 112–126. https://doi.org/10.1016/j.jvolgeores.2007.04.006

Saucedo, R., Macías, J. L., Ocampo-Díaz, Y. Z. E., Gómez-Villa, W., Rivera-Olguín, E., Castro-Govea, R., Sánchez-Núñ ez, J. M., Layer, P. W., Torres Hernández, J. R., & Carrasco-Núñez, G. (2017). Mixed magmatic-phreatomagmatic explosions during the formation of the Joya Honda maar, San Luis Potosí, Mexico. In *Geological Society Special Publication* (Vol. 446, Issue 1, pp. 255–279). Geological Society of London. https://doi.org/10.1144/SP446.11

Schipper, C. I. (2009). *Explosive Submarine Volcanism at Lō `ihi Seamount , Hawai `i*.

Shea, T., Houghton, B. F., Gurioli, L., Cashman, K. v., Hammer, J. E., & Hobden, B. J. (2010). Textural studies of vesicles in volcanic rocks: An integrated methodology. *Journal of Volcanology and Geothermal Research*, *190*(3–4), 271–289. https://doi.org/10.1016/j.jvolgeores.2009.12.003

Sheridan, M. F., & Wohletz, K. H. (1983). Explosive Volcanism. In *Journal of Volcanology and Geothermal Research* (Vol. 17).

Smith, I. E. M., & Németh, K. (2017). Source to surface model of monogenetic volcanism: A critical review. In *Geological Society Special Publication* (Vol. 446, Issue 1, pp. 1–28). Geological Society of London. https://doi.org/10.1144/SP446.14

Suwarti, T., & Suharsono (1992). *Geological map of the Lumajang and Probolinggo Quadrangle, Java. Geological Research and Development Centre of Indonesia. Scale 1:100.000.*

Valentine, G. A., White, J. D. L., Ross, P. S., Graettinger, A. H., & Sonder, I. (2017). Updates to Concepts on Phreatomagmatic Maar-Diatremes and Their Pyroclastic Deposits. In *Frontiers in Earth Science* (Vol. 5). Frontiers Media S.A. https://doi.org/10.3389/feart.2017.00068

White, J.D., & Houghton, B.F. (2006). Primary volcaniclastic rocks. *Geology, 34*, 677-680. https://doi.org/10.1130/G22346.1

White, J. D. L., & Valentine, G. A. (2016). Magmatic versus phreatomagmatic fragmentation: Absence of evidence is not evidence of absence. *Geosphere*, *12*(5), 1478–1488. https://doi.org/10.1130/GES01337.1

White, J. D. L., & Ross, P. S. (2011). Maar-diatreme volcanoes: A review. In *Journal of Volcanology and Geothermal Research* (Vol. 201, Issues 1–4, pp. 1–29). https://doi.org/10.1016/j.jvolgeores.2011.01.010

Wohletz, K. H. (1983). Explosive Volcanism. In *Journal of Volcanology and Geothermal Research* (Vol. 17).

Wohletz, K. H., & Sheridan, M. F. (1983). Hydrovolcanic explosions II. Evolution of basaltic tuff rings and tuff cones. *American Journal of Science*, *283*(5), 385–413. https://doi.org/10.2475/ajs.283.5.385

Zimanowski, B., Fröhlich, G., and Lorenz, V. (1997). Quantitative experiments on phreatomagmatic explosions. *Journal of Volcanology and Geothermal Research, 78(1-2)*, 57-68. https://doi.org/10.1016/0377-0273(91)90050-A

Chapter III - The magmatic system beneath maar complex at Lamongan Volcanic Field (LVF), East Java, Indonesia: revealed from the geochemistry of ash particles

3.1. INTRODUCTION

Volcanic ash particles serve as valuable records that offer crucial insights into the evolution and eruption dynamics of their magma (e.g. Cioni et al., 1992; Óladóttir et al., 2008). The morphological and component characteristics of volcanic ash allow fingerprinting of a specific eruptive process and fragmentation mechanisms (e.g. Heiken and Wohletz, 1985; Maria and Carey, 2001; 2007; Schmith et al., 2018). Furthermore, the geochemical composition of volcanic ash can be used to infer the pre-eruptive history of related magmatic systems and processes. In particular, the major element, trace element, and mineral chemistry of bulk ash and individual ash particles can be used to identify fractionation assemblages, magma storage, influence of assimilation, as well as the involvement of magma mixing/recharge (e.g. Óladóttir et al., 2008; Preece et al., 2016). However, most geochemical studies have relied on the analysis of relatively large clasts, such as lapilli, pyroclasts, and lithic fragments, rather than fine ash particles. Only a few studies have undertaken detailed geochemical characterization of the fine ash fraction, despite its common as the product of explosive volcanic eruptions.

Monogenetic volcanoes often exhibit significant geochemical variation over short spatial and temporal scales due to their small magma batches and rapid eruption timescales (e.g. Dorendorf et al., 2000; Nemeth et al, 2003; McGee et al., 2012; Nche et al., 2021). The magmatic processes influencing these monogenetic volcanoes include fractional crystallization of mafic mineral assemblages (e.g. clinopyroxene, olivine, and plagioclase), crustal contamination through assimilation, magma recharge and mixing events, and variable degrees of partial melting of heterogeneous mantle sources (e.g. Brenna et al., 2010; McGee et al. 2012; Németh and Kereszturi 2015). Consequently, a detailed geochemical fingerprinting of fine volcanic ash from monogenetic eruptions could provide new insights into the processes

influencing the compositional diversity of their magmas. Furthermore, the application of fine ash geochemistry in other volcanic systems has promising potential.

This chapter presents a detailed component analysis of volcanic ash and related deposits from the Lamongan Volcanic Field (LVF) in East Java, Indonesia. The LVF comprises over 90 small monogenetic volcanic centers, including maars and scoria/spatter cones (Carn and Pyle, 2001). There is a lack of geochemical data on the fine ash products produced by explosive maar-forming eruptions in this volcanic field. The objective of this study is to investigate the magmatic processes influencing the compositional variations of the ash particles. To achieved this, we analyzed major element, trace element, and mineral chemistry data from ash particles collected from six maar deposits, utilizing X-ray fluorescence (XRF), inductively coupled plasma mass spectrometry (ICP-MS), and electron probe micro-analyzer (EPMA) analysis, respectively. The assessment of fractionation assemblages, mantle source characteristics, and crustal assimilation provides insights into the key processes governing compositional diversity within the LVF ash deposits. The findings improve our understanding of the origin and evolution of magmas feeding explosive volcanism in monogenetic volcanic fields.

3.2. SAMPLE AND ANALYTICAL METHODS

Eighty-three samples from accumulated ash grains were collected from six representative maar deposits, which are (1) Ranu Klakah, (2) Ranu Klakah, (3) Ranu Kering, (4) Ranu Air, (5) outcrop NE Ranu Kembar, and (6) Ranu Segaran. In addition, three lava samples (north and east lava) and four scoria samples (north scoria cone). Ash particles were categorized into five groups, such as black non vesicular (*bnv*), black vesicular (*bv*), clear-pale brown (*cb* + *pb*), orange-brown (*ob*) particles, and grayish-black (gray; east maars). The freshest (glossy) and least weathered ash particles between 0.5 and 1 mm were hand-selected from each groups. The hand specimens of lava samples are cut into 3-5 mm dice. For scoria, lapilli (> 2 mm) and ash

sized (1 mm) were selected. All samples were cleaned thoroughly via ultrasonication in distilled water and subsequently dried at 80°C for 12 hours.

The cleaned ash, lava, and scoria samples were pulverized into powders using a tungsten carbide ring mill. The resulting powders were then heated to 900°C to determine loss on ignition (LOI) values. An alkali flux was used to prepare samples for X-ray fluorescence (XRF) analysis, mixed in proportions of 3g Merck Spectromelt®A10 ($Li_2B_4O_7$) and 1g Merck Spectromelt®A20 ($LiBO_2$) with 0.8g powdered sample. The glasses were fused at 1150°C with a dilution ratio of 5:1 (flux to sample). Accurate measurements ensured proper calibration to the internal standard (Li).

The compositions major elements (Si, Ti, Al, Fe, Mn, Mg, Ca, Na, K, and P) and trace elements (Ba, Zr, Rb, Sr, Nb, Cr, Ni, Y, and V) were determined using matrix-corrected calibration curves obtained through X-ray fluorescence analysis using the ZSX Primus II instrument by Rigaku Co., installed at Akita University. These calibration curves were constructed using international standard rock samples from the Geological Survey of Japan (GSJ).

Nineteen representative powder samples underwent wet digestion method for inductively coupled plasma mass spectrometry (ICP-MS) analysis. Samples (0.1 g) were weighed into 7 ml Teflon PFA screw jars and digested with 0.5 ml 30 M HF, 0.3 ml 7 M $HClO_4$, and 0.5 ml 0.5 M HNO_3 at 135°C for 72 hours. Upon cooling, ultrapure water was added to maximum capacity and samples were dried overnight at 135°C. Next, 1 ml 0.5 M HNO_3 was introduced and heated at 75°C for 30 minutes before filling to capacity with ultrapure water and heating at 95°C for 1 hour.

The resulting solutions were serially diluted for ICP-MS analysis. A 1000x dilution was prepared by mixing 5 ml sample, 4 ml 0.5 M HNO_3, and ultrapure water in 100 ml volumetric flasks. A second dilution combined 5 ml of the 1000x dilution, 2.5 ml 0.5 M HNO_3, and

ultrapure water in 50 ml volumetric flasks. Finally, 1 ml of the second dilution was analyzed using an Agilent 8900 ICP-MS Triple Quad instrument installed at Akita University.

Polished cross-sections of samples (ash, lava, scoria) were prepared for quantitative electron microprobe analysis. Samples were polished on agate with #6000 alumina powder and 1 μm diamond paste. A 20-25 μm thick carbon coat was applied to facilitate imaging and analysis. Backscattered electron (BSE) imaging and microprobe analyses were conducted using a JEOL JXA 8230 electron microprobe installed at Akita University. The analytical conditions were: 15 kV accelerating voltage, 20 nA beam current, 2-5 μm beam diameter, 10-20 sec peak counting times, and oxide & ZAF correction. Calibration utilized standard minerals with known compositions, including jadeite (Si, Na), rutile (Ti), corundum (Al), chromium oxide (Cr), hematite (Fe), manganosite (Mn), periclase (Mg), wollastonite (Ca), and KTiPO4 (K). Measurements were obtained on five WDS channels: Channel 1 (TAPH) for Na, Mg; Channel 2 (TAP) for Al, Si; Channel 3 (LIF) for Cr, Mn; Channel 4 (LIFH) for Ti, Ni, Fe; and Channel 5 (PETH) for K, Ca, P. The sequence was arranged to analyze Na first, minimizing potential loss.

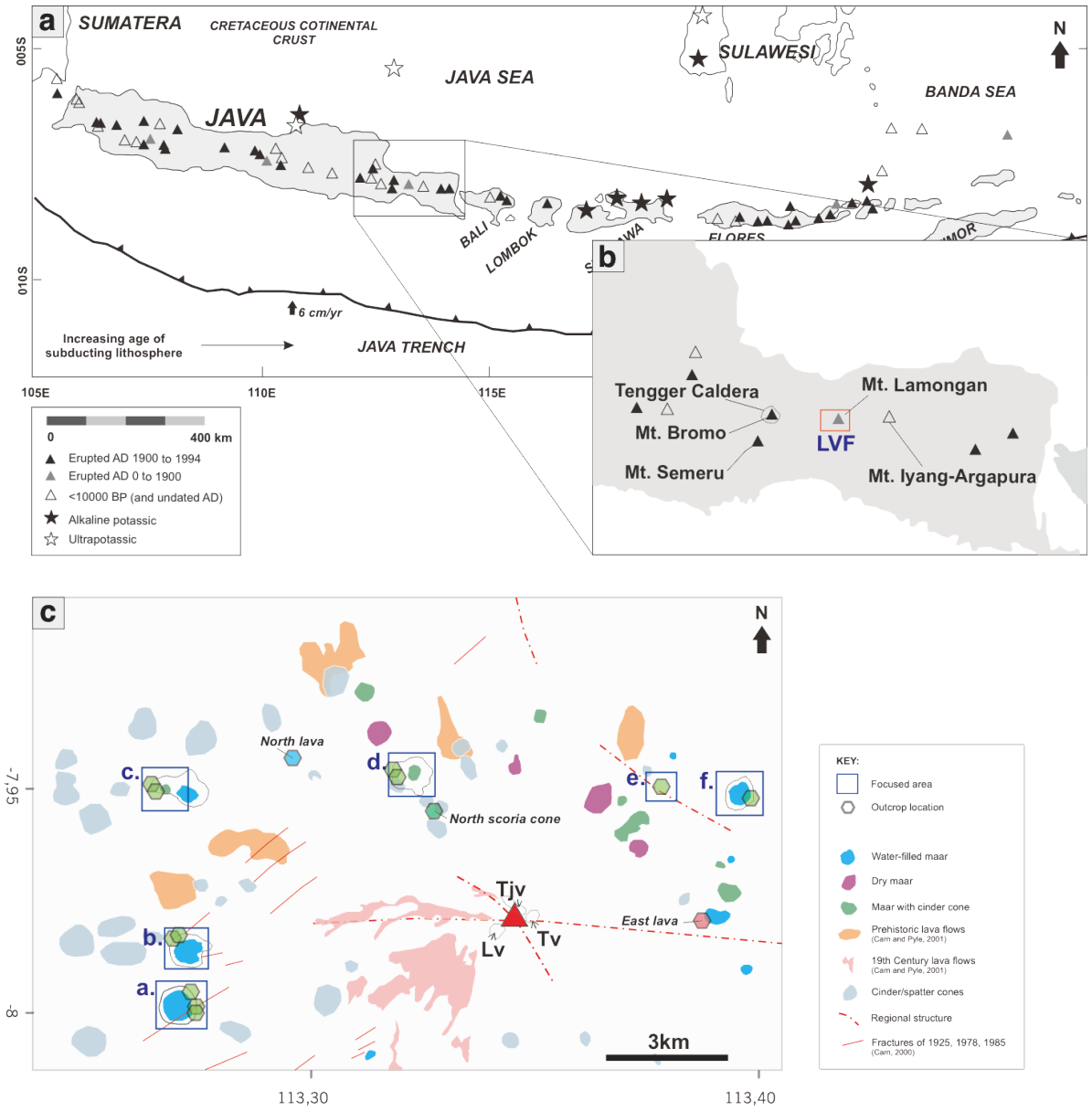

Figure 3. 1. (**a**) Map of Java with an inset map of East Java showing the location of Lamongan volcano and the Lamongan volcanic field (LVF, red square). (**b**) Map showing the distribution of eruptive vents in the LVF. Blue squares indicate the maar lakes observed in this study: west maars including a) Ranu Pakis and b) Ranu Klakah; north maars including c) Ranu Kering and d) Ranu Air; and east maars including e) outcrop near Ranu Kembar and f) Ranu Segaran. The distribution of maars, lava flows, and cinder-spatter cones on LVF according to Carn and Pyle, 2001. Abbreviations on the map of Lamongan volcano are: Tjv = Tjupu vent, Tv = Tarub vent, Lv = Lamongan vent.

3.3. RESULTS

3.3.1 Petrography

The ash particles derived from the maar complex of the LVF predominantly consist of basaltic rocks, exhibiting phenocrysts and microphenocrysts of plagioclase, clinopyroxene, Fe-Ti oxides, and minor olivine, within a highly crystalline groundmass. Figure 3.2 provides a visual representation highlighting the petrographic variations observed in the ash particle samples collected from the maar complex deposits. The black vesicular (*bv*) ash exhibits a coarse-grained texture, characterized by euhedral plagioclase, clinopyroxene, and Fe-Ti oxide phenocrysts measuring 50-100 µm. The groundmass is predominantly composed of clinopyroxene microphenocrysts (20-50 µm) and microlites (smaller than 20 µm), along with a significant abundance of vesicles. On the other hand, the clear-pale brown (*cb-pb*) ash is primarily composed of plagioclase phenocrysts (100-150 µm) and is dominated by groundmass-rich microphenocrysts (20-50 µm) of pyroxene, plagioclase, and Fe-Ti oxides. The black non-vesicular (*bnv*) ash displays mostly plagioclase and a spotted Fe-Ti oxide phenocrysts (50-100 µm), accompanied by a fine-grained groundmass consisting of elongate plagioclase, skeletal clinopyroxene, and Fe-Ti microlites smaller than 20 µm. In contrast, the orange-brown (*ob*) ash contains rare phenocrysts and exhibits a predominantly very fine-grained groundmass (less than 10 µm) consisting of plagioclase and Fe-Ti oxides.

Furthermore, the samples obtained from the north lava, east lava, and north scoria cone display the presence of phenocryst comprising plagioclase, clinopyroxene, and olivine ranging in size from 100 µm to 0.5 cm. The east lava sample exhibits a high porphyritic and is primarily composed of plagioclase and clinopyroxene, with minor olivine microphenocryst. The clinopyroxene commonly display a spongy reaction rim and contain Fe-Ti oxide, plagioclase, and occasionally melt inclusions, which were concentrated at the edge of the crystal. These samples typically exhibit a coarse-grained groundmass with similar mineralogy and varying

amount of glass. The north lava sample contains plagioclase, clinopyroxene, and minor olivine microphenocryst, exhibiting a seriate texture and a fine-grained groundmass rich in Fe-Ti oxides. Plagioclase often exhibits fine-scale concentric zones, sieved texture, and zoned inclusions, frequently consisting of Fe-Ti oxides. The north scoria cone deposit is primarily composed of olivine-rich rock, with minor clinopyroxene, Fe-Ti oxides, and plagioclase phenocryst, along with a slightly enriched microphenocryst and microlite content in the glassy groundmass.

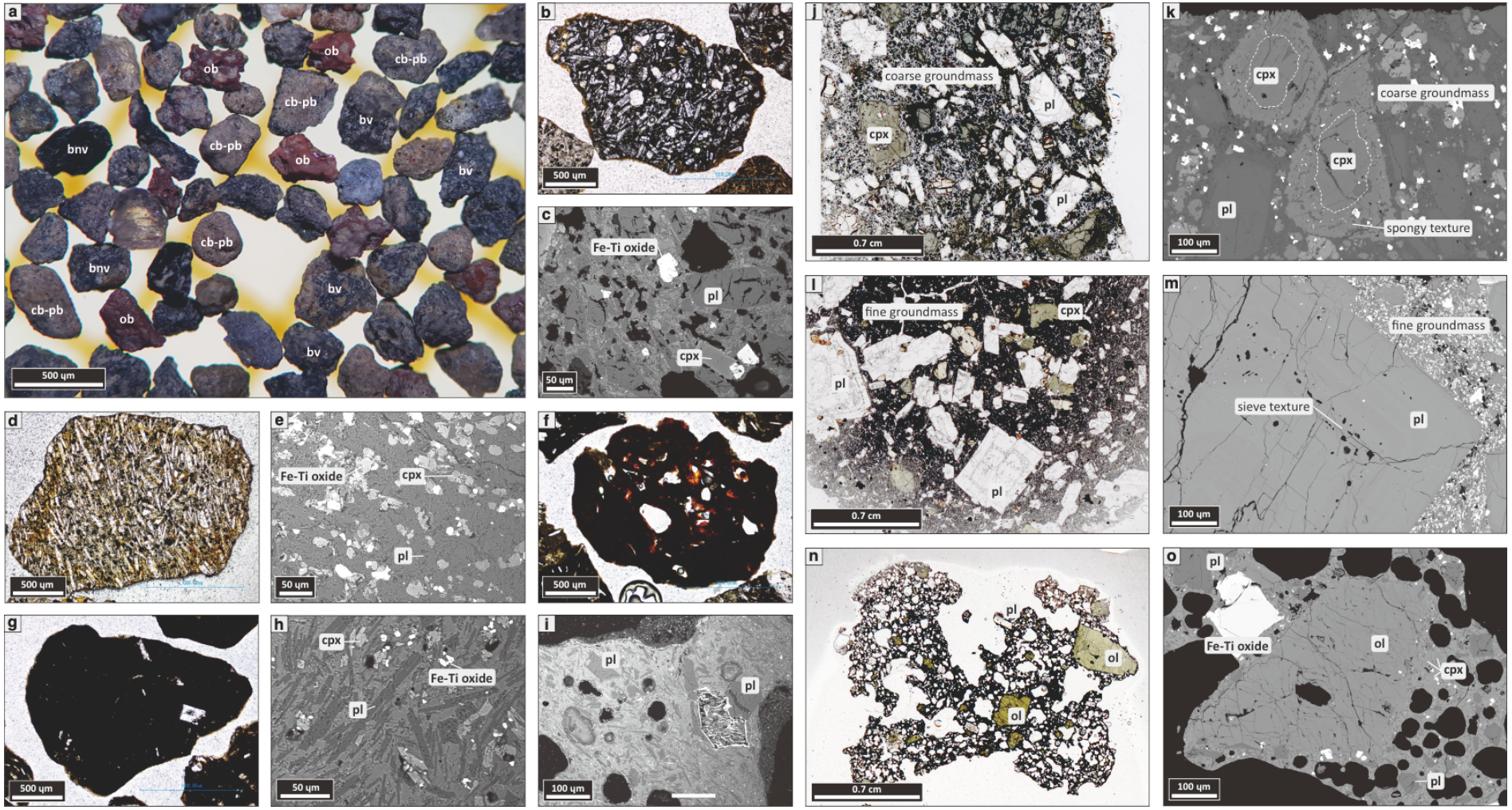

Figure 3. 2. Representative photograph of ash grains (**a**) and corresponding photomicrographs featuring backscattered electron (BSE) images. (**b-o**) from studied samples in the LVF maar complex. The images showcase various type of samples, including (**b-c**) bv ash, (**d-e**) cb-pb ash, (**g-h**) bnv ash, (**f-i**) ob ash, (**j-k**) east lava, (**l-m**) north lava, and (**n-o**) north scoria cone. The labels within the image indicate specific mineral components: pl= plagioclase, cpx= clinopyroxene, and ol= olivine.

3.3.2. Major element data

The bulk-rock composition of studied samples (ash, lava, and scoria) obtained from LVF maar complex exhibit a range of picrobasalt, basalt, and basaltic andesite compositions (Fig. 3.3), consistent with the volcanic products documented along the LVF complex by Carn and Pyle, 2001. Figure 3.4 presents the variations of major elements plotted against MgO for the samples. The volcanic ash samples demonstrate variations ranging from 44 to 55 wt% SiO_2 and 2.5 to 7.5 wt% MgO. Major elements such as SiO_2, CaO, Na_2O, K_2O, and P_2O_5 exhibit similar compatible trend with respect to MgO across the different magma types. The ob and bnv ash represent the most evolved compositions (>49 wt% SiO_2, <10 wt% CaO, >2.2 wt% Na_2O, >1 wt% K_2O, and >0.25 wt% P_2O_5) and share a relative similar composition with the samples from Bromo Tengger Caldera, Semeru, and LVF lavas (mainly historical lava flows and maar deposits identified by Carn and Pyle, 2001). Notably distinct patterns in relation to MgO are observed for the concentrations of Al_2O_3, FeO*, and TiO_2. Except for bnv and ob ash, the samples exhibit an increasing trend in alumina content as magnesium content decreases. The trends of iron and titanium with respect to magnesium in cb-pb, bv, gray ash and scoria samples generally display decreasing values, while ob and bnv ash show contrasting trends. The east lava sample is distinctly separated in these plots and exhibits similar characteristics to several prehistoric lava samples identified by Carn and Pyle, 2001.

There is a noticeable compositional gap at approximately 5 wt% MgO, which distinguishes the group of ash particles. The ob and bnv ash samples exhibit compositions medium-K picrobasalt to basalt, characterized by high SiO_2, Na_2O, K_2O, P_2O_5, TiO_2 and low Al_2O_3, CaO, and FeO*. Conversely, the cb-pb and gray ash samples fall within the range of medium-K to high-K basalt to basaltic andesite, displaying low SiO_2, Na_2O, K_2O, P_2O_5, TiO_2 and high Al_2O_3, CaO, and FeO*. The black vesicular (*bv*) ash samples are generally close to this compositional range, although some samples are plotted in the lower groups of ob and bnv

ash. The scoria cone samples demonstrate lower concentration of SiO_2 (41-44 wt%), Al_2O_3, P_2O_5, and higher CaO. Once again, the east lava sample stands out significantly from the other suites in terms of composition, with the highest concentrations of MgO (11%), high CaO, low SiO_2, Na_2O, K_2O, P_2O_5, TiO_2, and moderate FeO*.

When plotted on the modified Miyashiro diagram (FeO*/(FeO*+MgO) vs. SiO_2 (Fig. 3.5) (Miyashiro, 1974; Gill, 2010), the samples exhibit a declining trend of continuous iron enrichment. They are primarily classified as high iron tholeiitic basalt. However, the east lava sample stands out with the lowest value, indicating 53% iron/(iron-magnesium) with 45 wt% silica. Most of the pre-historical and historical lava samples identified by Carn and Pyle, 2001 fall within the category of medium iron tholeiitic basalt.

Figure 3.6 illustrates the spatial chemical variation observed in the studied samples. The different types of ash particle exhibit comparable concentration of MgO, Ni, and SiO_2 across various eruption centers (for example, the cb-pb ash has low magnesium and silica from west and north maars). Generally, the west and north maars display similar variation patterns, although Ranu Air (RA) exhibit slightly lower values. In contrast, the samples from the east maars have lower concentration of MgO, Ni, and SiO_2 compared to the samples from other maars. Notably, the north scoria cone samples exhibit the lowest silica content, ranging from 41 to 43 wt%, while the Ranu Agung lava (east lava) shows the highest concentrations of MgO (11 wt%) and Ni (~60 ppm).

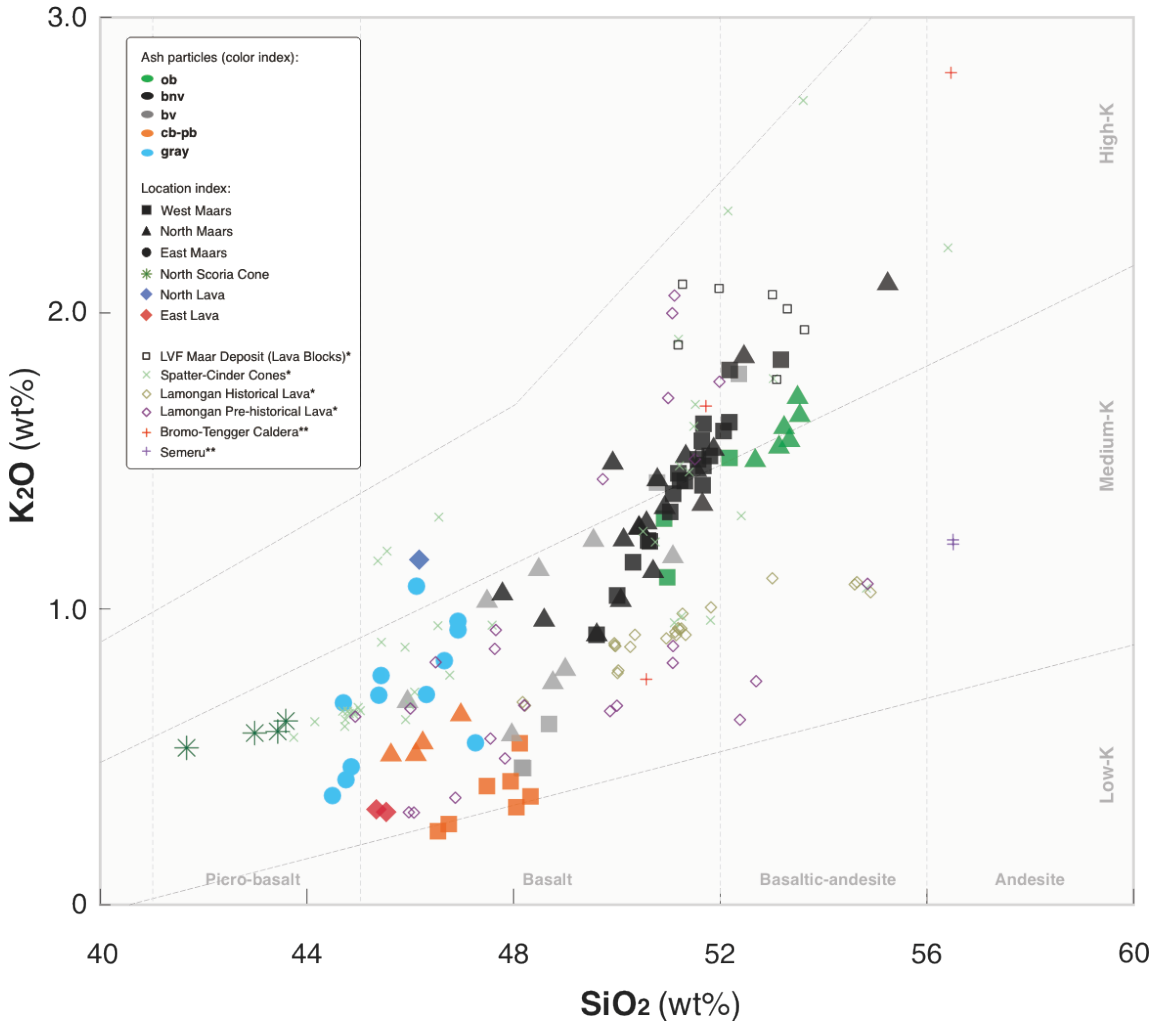

Figure 3. 3. Classification plots showing the sub-alkaline rock series for LVF maar complex samples (ash, lava, and scoria). The plots also include LVF samples examined by *Carn & Pyle (2001) and nearby volcanoes analyzed by **van Gerven & Pichler (1995), following the classification system of Le Maitre (2002).

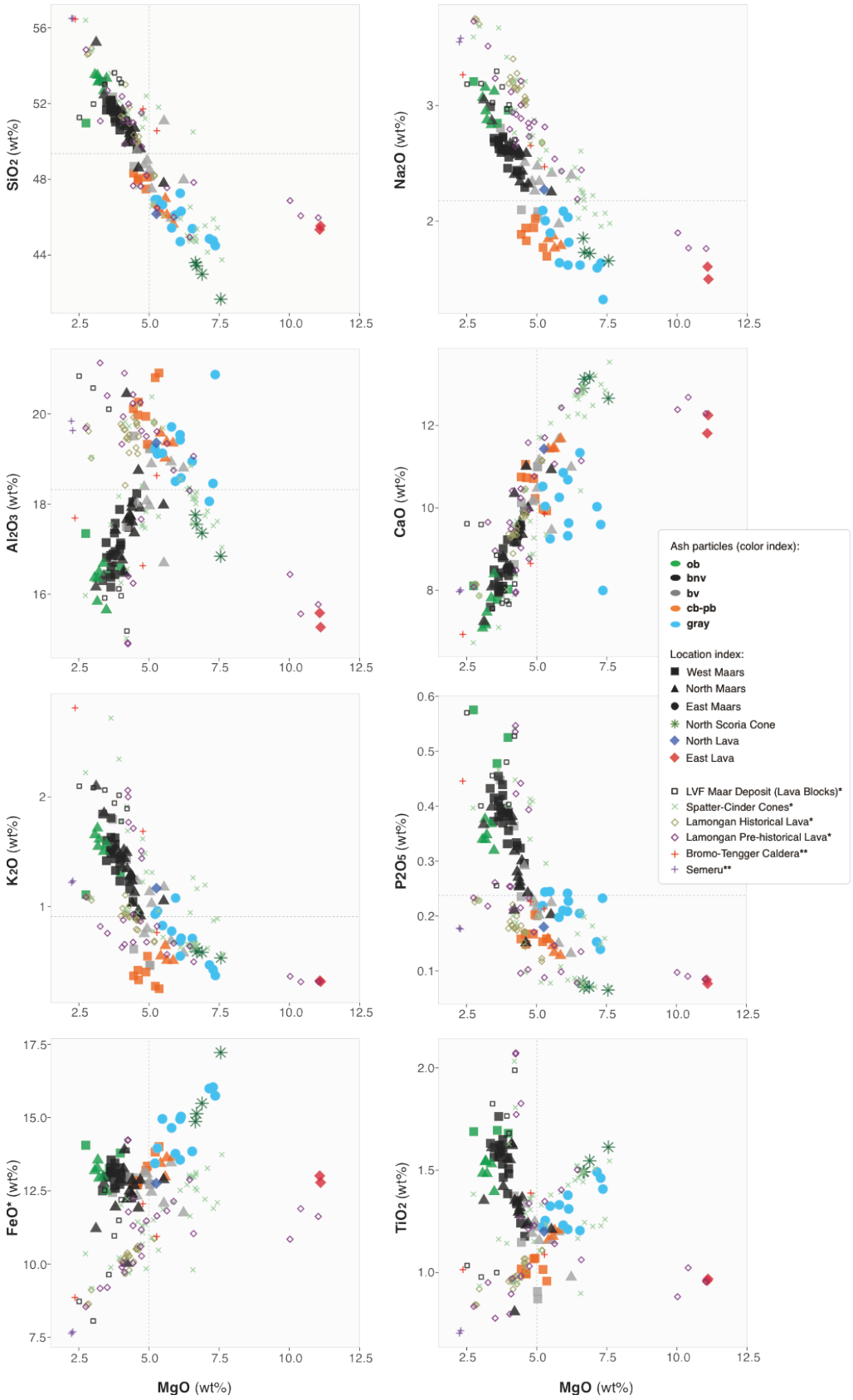

Figure 3. 4. Harker diagrams of the major element variation (vs. MgO) in LVF maar complex deposits.

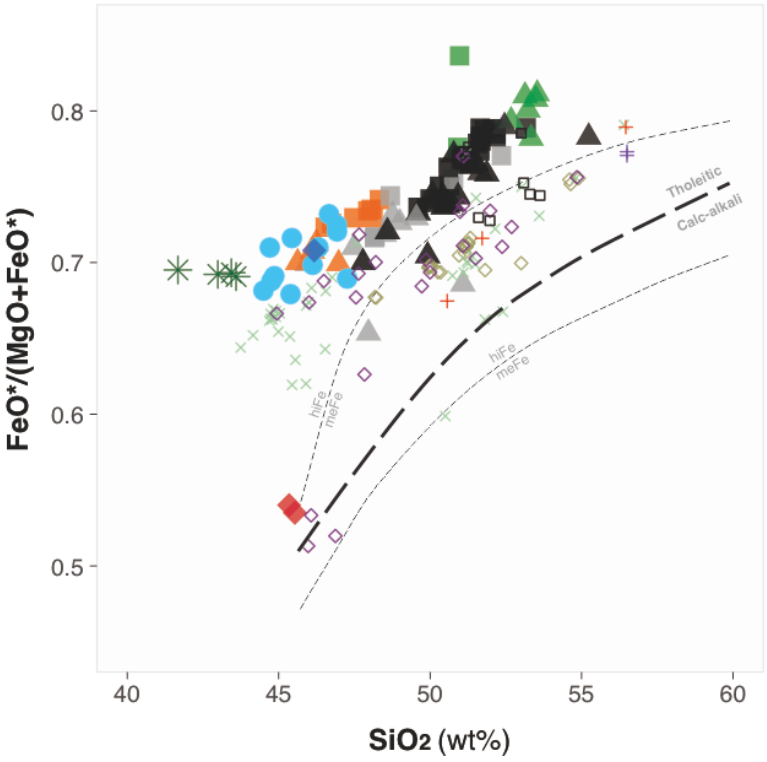

Figure 3. 5. Discrimination diagram between tholeiitic and calc-alkaline magma series diagram based on (FeO*/(FeO*+MgO) versus SiO_2 from Miyashiro (1974), modified by (Gill, 2010).

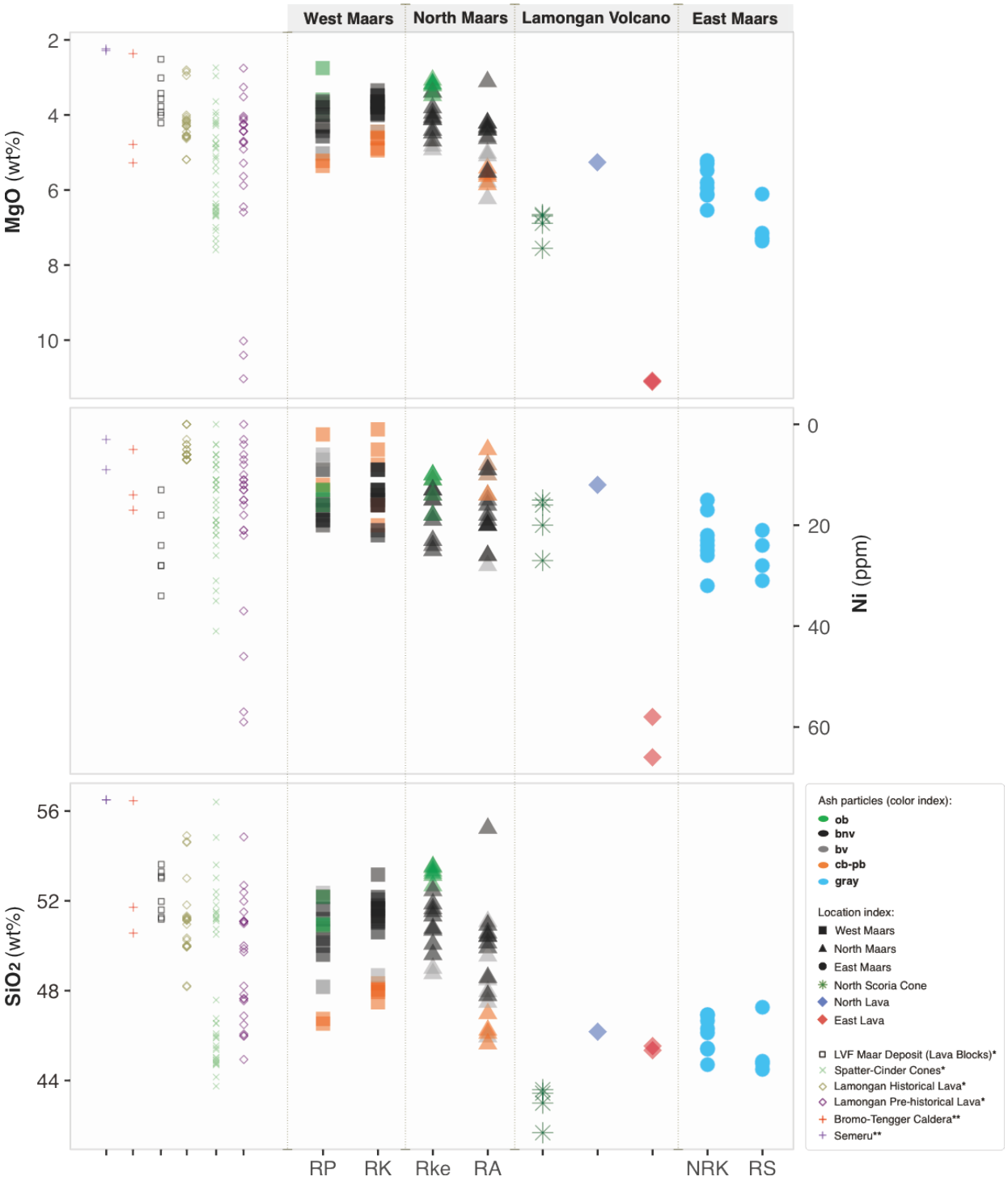

Figure 3. 6. Spatial variation of MgO, Ni, and SiO_2 in the studied samples from LVF maar complex. The observed trend reveals an increase in silica concentration within the maar deposits, particularly from east to north and west maars. Among the deposits, the east lava and scoria cone samples display the most primitive and near-primary (parental) magma compositions in this region. The abbreviations correspond to specific locations: RP= Ranu Pakis, RK= Ranu Klakah, Rke= Ranu Kering, RA= Ranu Air, NRK= Outcrop NE Ranu Kembar, RS= Ranu Segaran.

3.3.3. Trace element data

The variation in MgO is well reflected in the trace element compositions of the studied samples (Fig. 3.7). The ash samples from the maar complex exhibit similarities with the major element compositions, featuring a distinct separation gap at approximately at 5 wt% MgO. Compatible trace elements such as V, Ni, and Cr show slightly higher abundances in cb-pb, bv, and gray ash compared to ob and bnv ash. The east lava displays the highest concentrations of Cr and Ni, while V slightly lower (~500 ppm), suggesting it may represent as the most primitive magma found in the area. The Sr content varies among the studied samples. Two distinct trend are observed: a negative trend of decreasing MgO with increasing Sr content in east lava, scoria cone, and gray + *cb-pb* + *bv* ash samples, and a contrary trend in the bnv to ob ash particles, where decreasing MgO is correlated with increasing Sr content. On the other hand, the incompatible elements (Ba, Zr, Pb and Nb) in the exhibit negative trends. Apart from magnesium content, the *ob* + *bnv* ash can be characterized by specific concentrations of incompatible elements, with Ba at ~400 ppm, Zr at ~100 ppm, Pb at ~8 ppm, and Nb at ~4.5 ppm.

Figure 3.8 displays the primitive mantle-normalized trace element diagrams of nineteen representative samples. Overall, the samples exhibit similar trends of trace elements but with varying concentration ratios. The bnv and ob ash samples demonstrate higher concentration, followed by *cb-pb*, *bv* ash, north lava, gray ash, scoria cone, and east lava samples. The *ob* and *bnv* ash samples exhibit nearly flat spikes of Sr and Zr, accompanied by a negative anomaly of Ti. In contrast, the other samples display positive spikes of Sr and negative anomalies of Zr. Notably, the scoria cone, east lava, and one sample of gray ash exhibit a positive anomaly of Ti.

Figure 3.8b. illustrates the primitive mantle-normalized rare earth element (REE) patterns. The ash particle samples exhibit a strong enrichment of Light REE (LREE) relative to heavy

REE (HREE) compared to the scoria and east lava samples. The potential primitive samples of east lava and north scoria cone display a similar trend but with lower trace elements compared to the N-MORB sample from Sun and McDonough (1989). A negative Eu anomaly is evident in the evolved ash samples (*bnv* and *ob*), indicating significant fractionation of plagioclase.

To gain further insights into the patterns of major and trace elements, a Principal Component Analysis (PCA) was performed on nineteen selected samples from each type. The results, represented by the first two first principal components (PCs), account for 84.4% of the total variance and are shown in Figure 3.9. The PC1-PC2 plot reveals a strong correlation between each sample type and its chemical characteristics. There is an opposing correlation observed between the *ob* + *bnv* ash samples and the *cb-pb* + *bv* ash + north lava + gray ash + scoria cone deposits + east lava samples along the PC1 axis.

The first group corresponds to the incompatible trace elements (e.g. Zr, Ba, Pb, Nb, etc.) as well as major elements such as SiO_2, Na_2O, K_2O, P_2O_5, MnO, and TiO_2. The second group represents predominantly mafic components including MgO, CaO, FeO*, Ni, Cr and V. These group also exhibit a strong correlation to Al_2O_3 contents, and this correlation becomes even more pronounced when considering Sr in junction with high values along the PC2 axis, particularly for the *cb-pb* + *bv* ash + north lava samples.

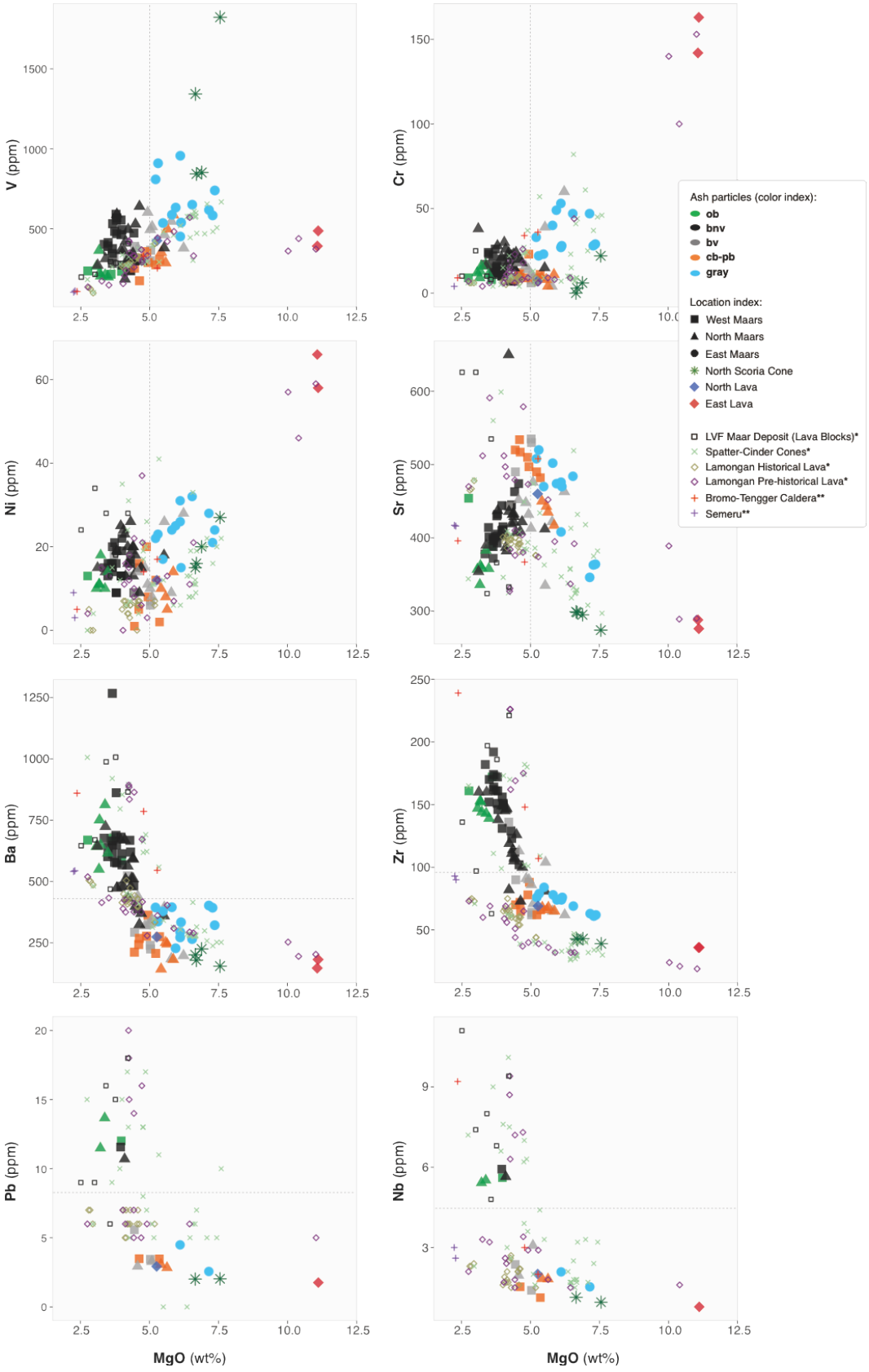

Figure 3. 7. Harker diagrams of the trace element variation (vs. MgO) in LVF maar complex deposits.

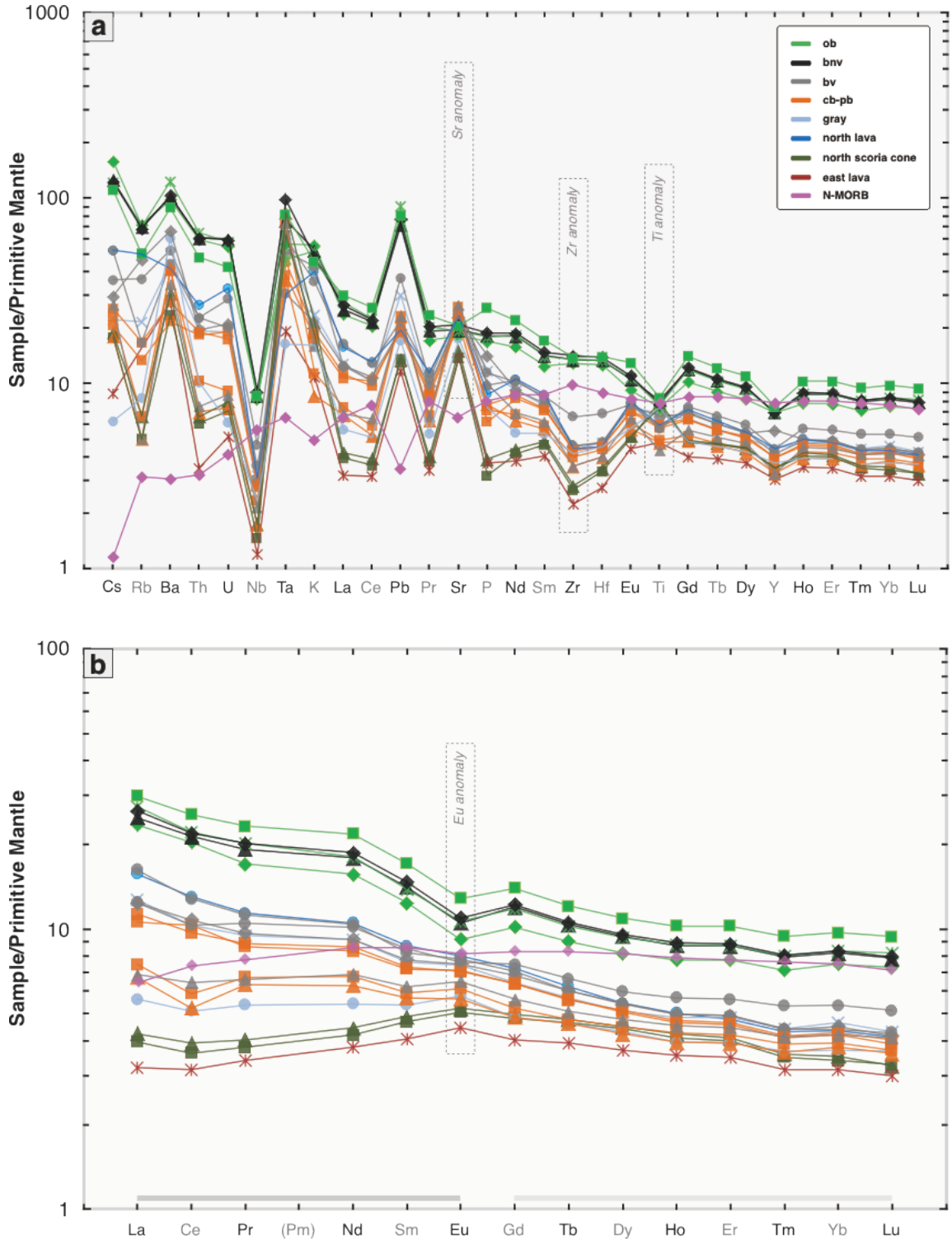

Figure 3. 8. Primitive mantle-normalized diagrams showing (**a**) multielement and (**b**) rare earth element (REE) pattern for representative samples obtained from LVF maar complex. The primitive mantle values utilized in the normalization are from McDonough and Sun, 1995. N-MORB trace element concentrations are from Sun and McDonough, 1989.

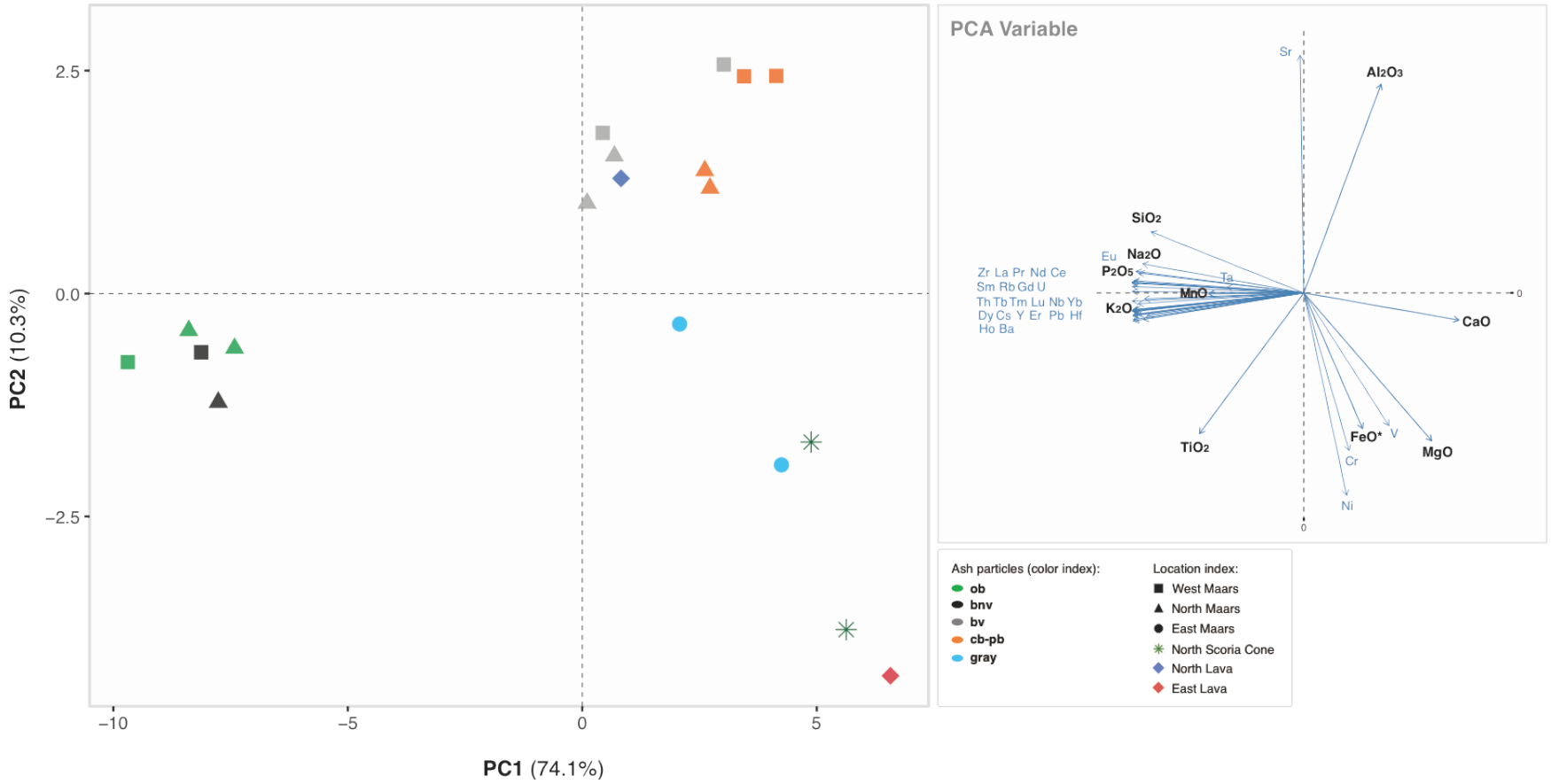

Figure 3. 9. Principal component analysis (PCA) of major and trace elements conducted on representative studied samples, including ash, north scoria cone and lava. The graph shows the first two principal components (PCs), which account for 84.4% of the total variance.

3.3.4. Mineralogy

The mineral compositions of plagioclase, pyroxene, and olivine were analyzed in the volcanic ash, lava, and scoria samples (Fig. 3.10 and 3.11). The crystals predominantly occur as microphenocrysts and/or microlites with minor phenocrysts, except for the lava and scoria cone samples.

Plagioclase exhibits a range of compositions from anorthite to andesine ($An_{36.1\text{-}94.3}Ab_{5.65\text{-}60.3}Or_{0.01\text{-}5.39}$). The north scoria cone and lava samples display relatively high An content ($An_{58\text{-}94}$), including anorthite, bytownite and minor labradorite compositions, compared to the ash particle samples. The plagioclase in the east lava sample has a lower An content ($An_{58\text{-}62}$), corresponding to a plagioclase rim that shares a similar composition with the microphenocrysts and microlites in the groundmass. On the other hand, the ash samples exhibit a wider range of plagioclase compositions. Each type of ash displays distinct compositions, which generally remain consistent even across different eruption vents. The black vesicular (*bv*) ash is the only ash sample that contains a proportion of anorthite composition. The orange-brown (*ob*) ash predominantly consists of labradorite composition with a narrow range of An content, with the exception of a phenocryst with bytownite composition.

Similar to plagioclase, the pyroxene crystals in each sample type exhibit a consistent variability and display distinct ranges of compositions. the pyroxenes in ash particle samples span a composition range from enstatite to diopside (Fig. 3.11). The black-vesicular (bv) and orange-brown (*ob*) ash predominantly consist of high-Ca clinopyroxene (augite-diopside), except for one microlite crystal in bv ash that has enstatite composition. The black non-vesicular (*bnv*), clear-pale brown (*cb-pb*), and gray ash exhibit similar compositions of clinopyroxene and orthopyroxene compositions, although orthopyroxene is absent in gray ash. The Mg# (magnesium number) ranges from high to low in *bv*, *bnv*, *ob*, to *cb-pb* ash, respectively.

Further, the north scoria cone and lava samples demonstrate a narrow composition range of high Ca-clinopyroxene (diopside) and are rich in magnesium (Mg_{65-83}). The clinopyroxene in the scoria cone sample also contains portions with high contents of Al_2O_3 and TiO_2, reaching up to 8 wt% and 1.5 wt%, respectively (Fig. 3.12b). In east lava sample, a contrast is observed between the higher Al_2O_3 of clinopyroxene phenocryst core compared to the rim and microlites, which are split at ~6 wt% alumina content.

Olivine crystals are typically present as phenocrysts in ash particles, although they can also be found as microphenocrysts and/or microlites. The Fo content plot is depicted in Figure 3.10. Among the ash particles, the majority of the black vesicular (*bv*) ash and black non-vesicular (*bnv*) ash samples from Ranu Pakis exhibit higher Fo (Fo_{63-75}) content compared to other ash particles. The microcrystals in the gray ash samples show significantly lower Fo content in olivine, ranging from Fo_{49} - Fo_{50}. In contrast, the olivine phenocrysts in the in north scoria cone samples display the highest Fo content, ranging from Fo_{69} to Fo_{79}.

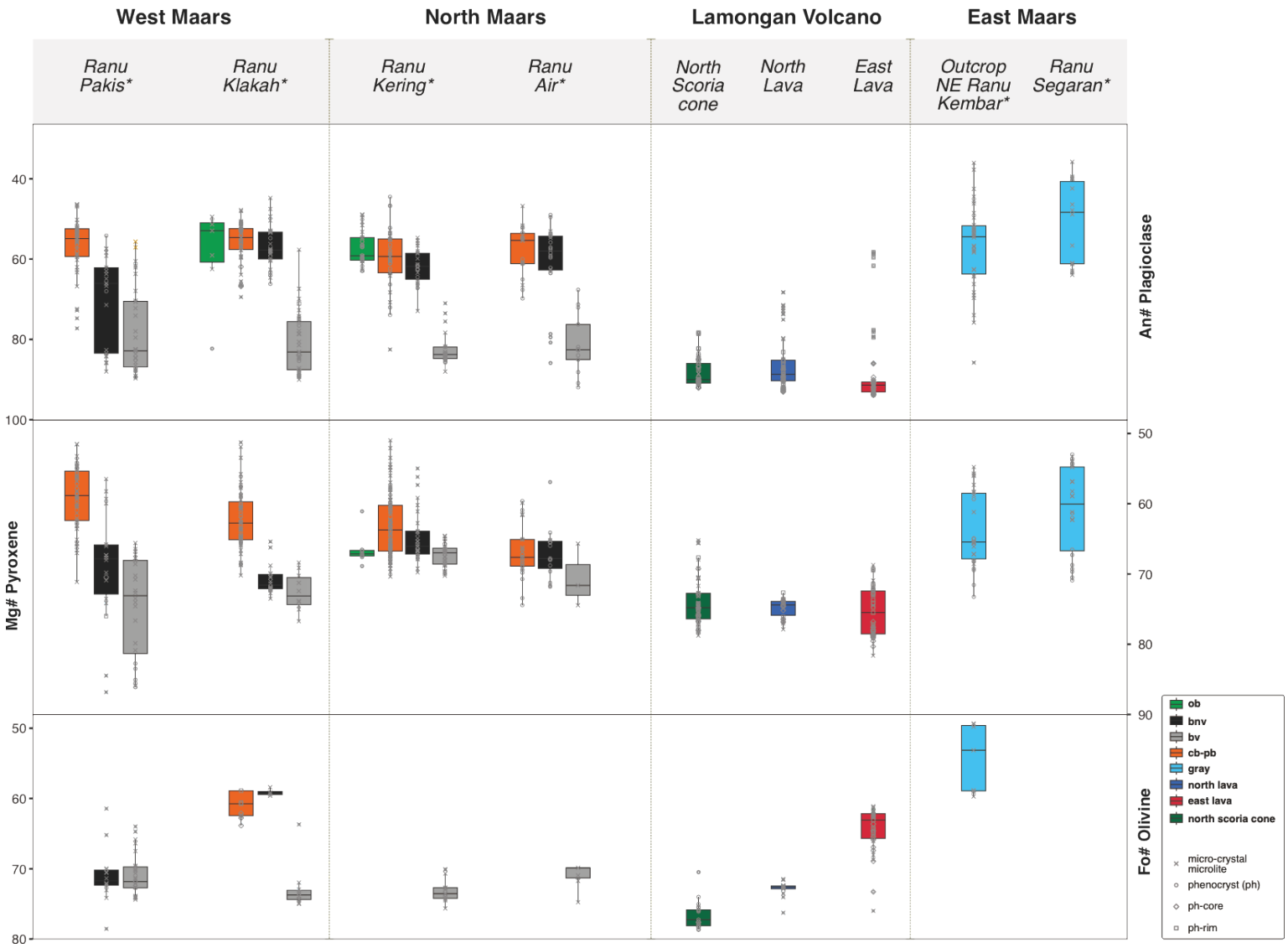

Figure 3. 10. Box plots of the anorthite (An) content of plagioclase, Mg number (Mg#) of pyroxene, and forsterite (Fo) content in the studied samples from LVF maar complex. The sample locations are arranged spatially from west maars, north maars, Lamongan volcano, and east maars.

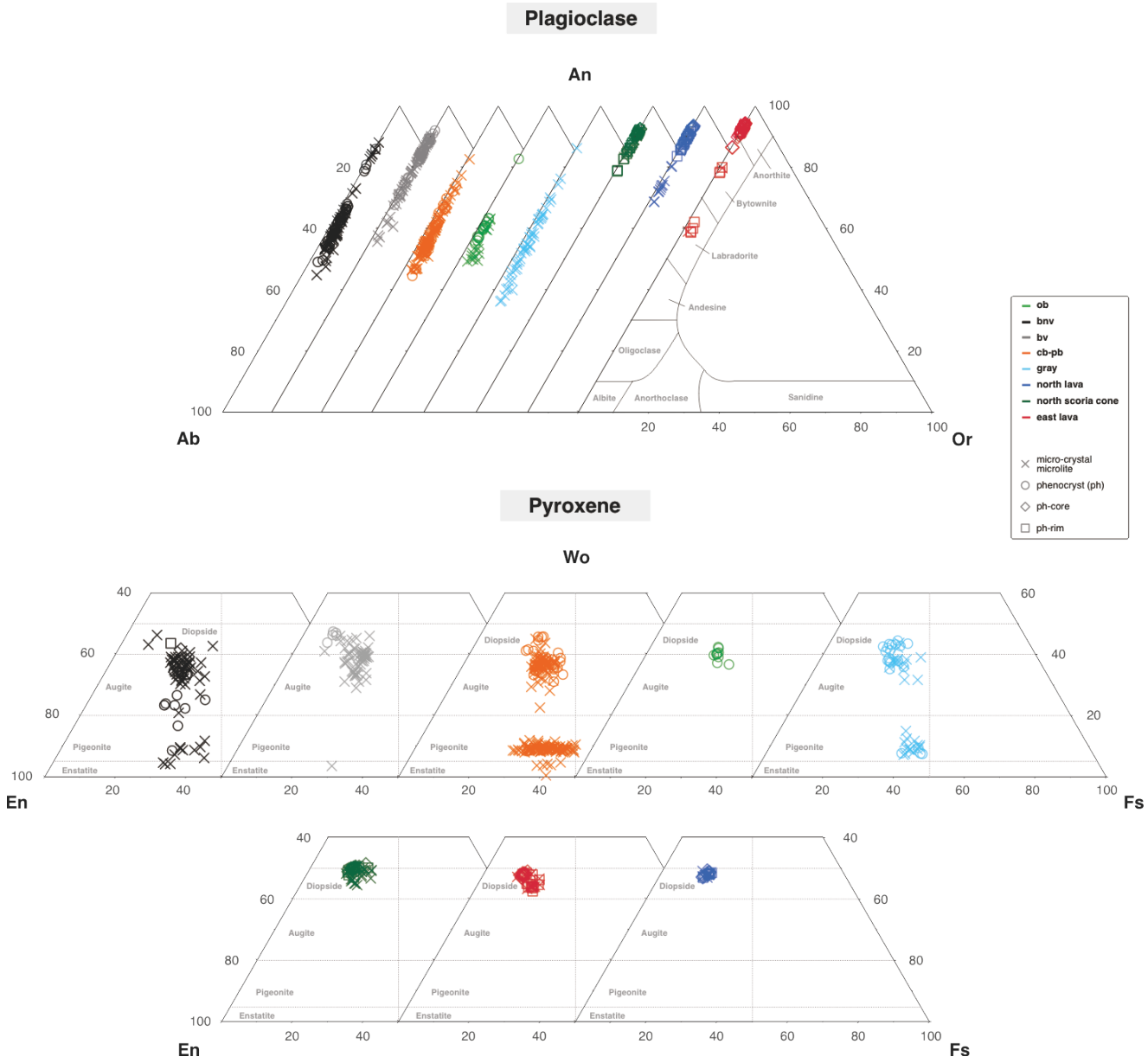

Figure 3. 11. Compositions of plagioclase and pyroxene in the studied samples, including phenocryst, phenocryst core, rim, and microcrystal/microlite phases.

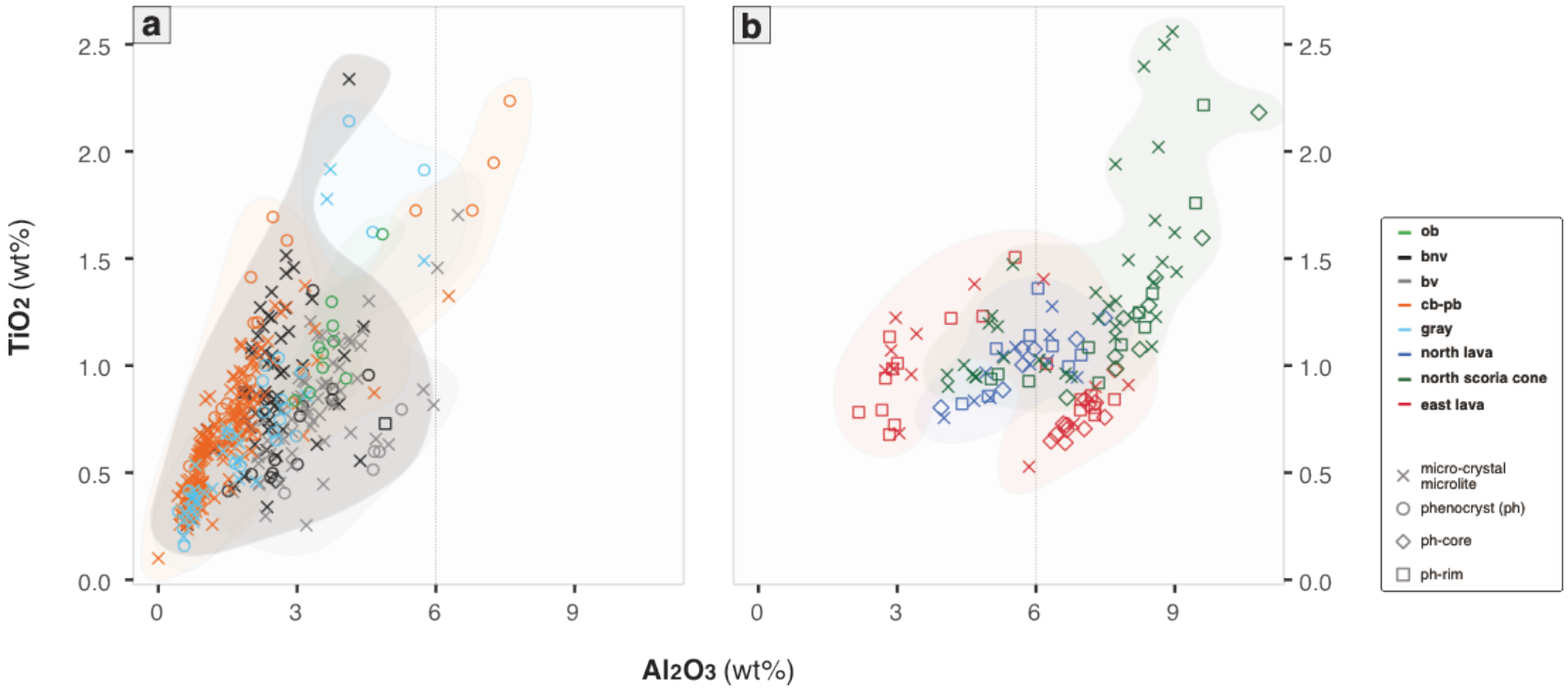

Figure 3. 12. Composition of pyroxene in the LVF maar complex, represented by TiO_2 vs. Al_2O3 (wt%) diagram. (**a**) Ash particles and (**b**) lava and north scoria cone samples. Majority of pyroxene in the ash samples exhibits low alumina content, generally below ~6 wt%. On the other hand, mostly pyroxene core in the lava and pyroxenes in north scoria cone samples exhibit higher alumina content (> 6 wt%), predominantly representing the presence of high Ca-pyroxene.

3.4. DISCUSSION

The petrography and geochemical study of the LVF maar complex reveal several geochemical patterns, which provide insights into the magmatic process that influenced the variation of erupted products. These findings also complement the missing geochemical information of maar products in the Lamongan Volcanic Field (LVF) reported by Carn and Pyle, 2001.

3.4.1. Crystal fractionation

The major and trace elements systematics, along with petrographic observations of the studied ash samples, suggest two distinct crystallization trends from the mafic endmembers (*cb-pb*, *bv*, and gray ash) to the more felsic endmembers (*bnv* and *ob* ash). In the mafic endmembers, the increasing of SiO_2 and Al_2O_3 content, along with the decreasing of CaO and compatible elements (Ni, V, and Cr), coupled with depleted MgO, are primarily attributed to olivine and clinopyroxene fractionation. On the other hand, the felsic endmembers exhibit contrasting positive decreasing trends in Al_2O_3 and Sr, while MgO shows an increasing trend. This suggests that felsic group is predominantly influenced by plagioclase fractionation, which is further supported by the negative anomalies in Eu concentrations observed in these samples (Fig. 3.8b). Furthermore, the changing trends of FeO* and TiO_2, with decreasing and increasing values, respectively in the mafic endmembers (except gray ash), imply a significant relationship between fractionated minerals and the iron and titanium contents. Overall, the major and minor compositions in the ash samples from LVF maar complex indicate a similar fractionation process of involving clinopyroxene ± olivine + plagioclase + Fe-Ti oxides, which aligns with the findings from studied historical lava flows by Carn and Pyle (2001).

The scoria cone and east lava samples can be considered as having a parental magma-like composition, particularly for the mafic endmembers ash particles. These samples mostly characterized by low concentrations of SiO_2, Na_2O, K_2O, P_2O_5, Sr, and incompatible elements,

along with high CaO, FeO*, and V in the case of scoria cone sample, and high Cr and Ni in the case of east lava sample. These elemental trends are primarily controlled by the process of olivine and clinopyroxene fractionation. The extreme low concentration of Al_2O_3 in the east lava sample indicates the presence of Al and Ca rich clinopyroxene phenocrysts. Additionally, the low FeO* and TiO_2 concentration in these samples suggest the occurrence of significant fractionation of Fe-Ti oxide phenocryst, which are typically of lager size (20-30 μm) and can be clearly observed (Fig. 3.2j and 3.2k).

The increasing concentration of highly incompatible elements (e.g. Rb, Ba, Nb, Pb) in ash samples suggests that the parental magmas likely underwent a closed-system fractional crystallization. However, these increasing trends could also indicate variations in partial melting of the source or assimilation-fractional crystallization (AFC) processes (Rasoazanamparany et al., 2016). In accordance with this, the enriched concentrations of LREE from mafic to felsic endmembers cannot be solely explained by the crystallization of olivine, pyroxene, and plagioclase (Dorendorf et al., 2000). Furthermore, it is observed that the variation range of MgO and FeO* is relatively smaller compared to the variation range of SiO_2, CaO, and most trace elements. The limited variation in MgO and the least variation of FeO* content, along with the contrasting trends between the mafic and felsic endmembers (e.g. Al_2O_3, FeO*, TiO_2, Sr), cannot be fully explained by crystallization differentiation alone. This suggest that other processes (e.g. magma assimilation, mixing, magma chamber dynamics) may have played role in shaping the observed geochemical variations.

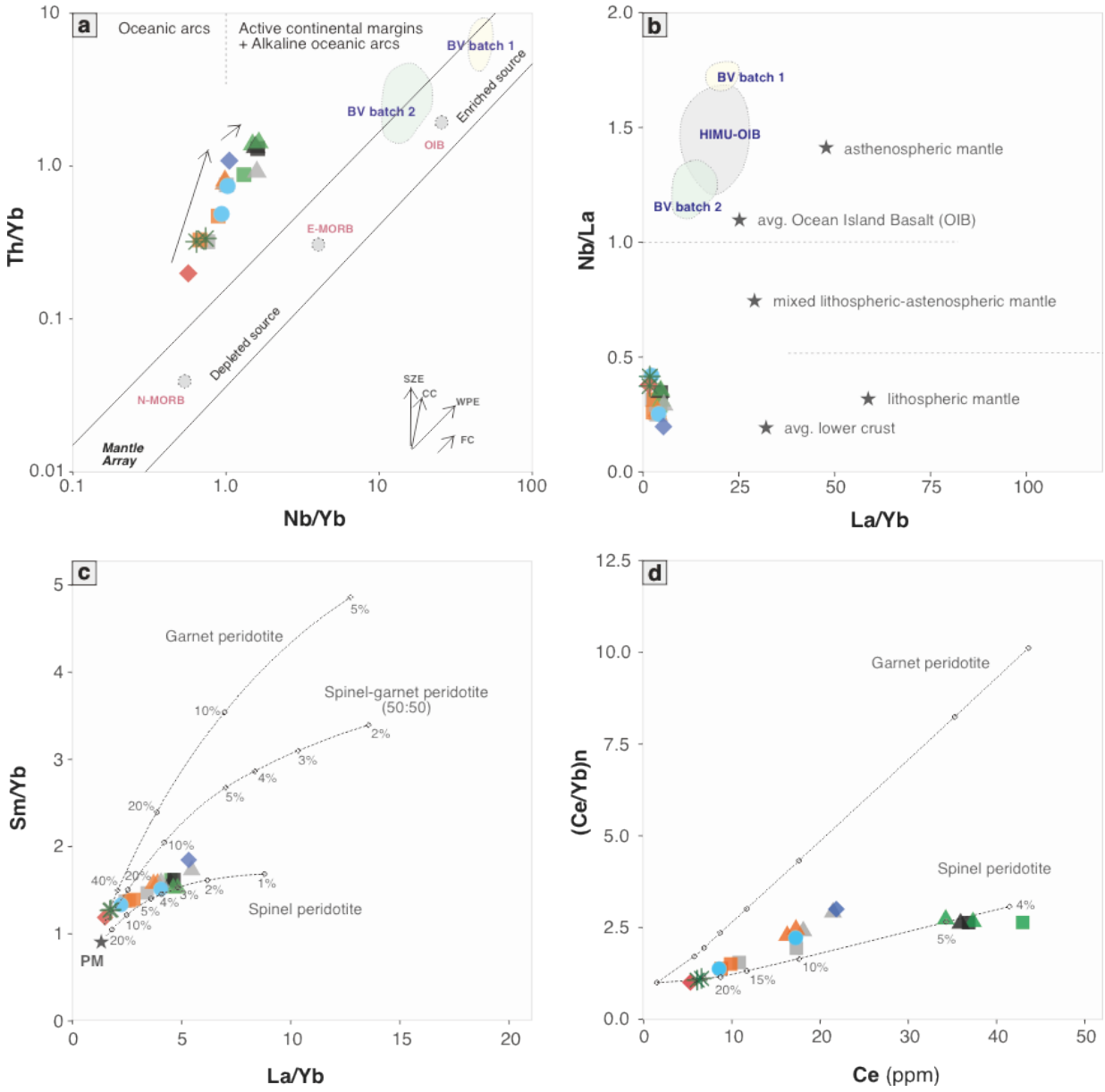

Figure 3. 13. (**a**) Th/Yb vs. Nb/Yb log-log diagram (Pearce, 2008). (**b**) Nb/La vs. La/Yb (Smith et al., 1999). (**c**) Sm/Yb vs. La/Yb and (**d**) PM-normalized Ce/Yb vs. Ce (ppm) showing the field and degree of melting of studied samples from LVF maar complex. PM = Primitive mantle is from Sun and McDonough, 1989. Melting curves are After Liu et al., 2014 and Nche et al., 2021.

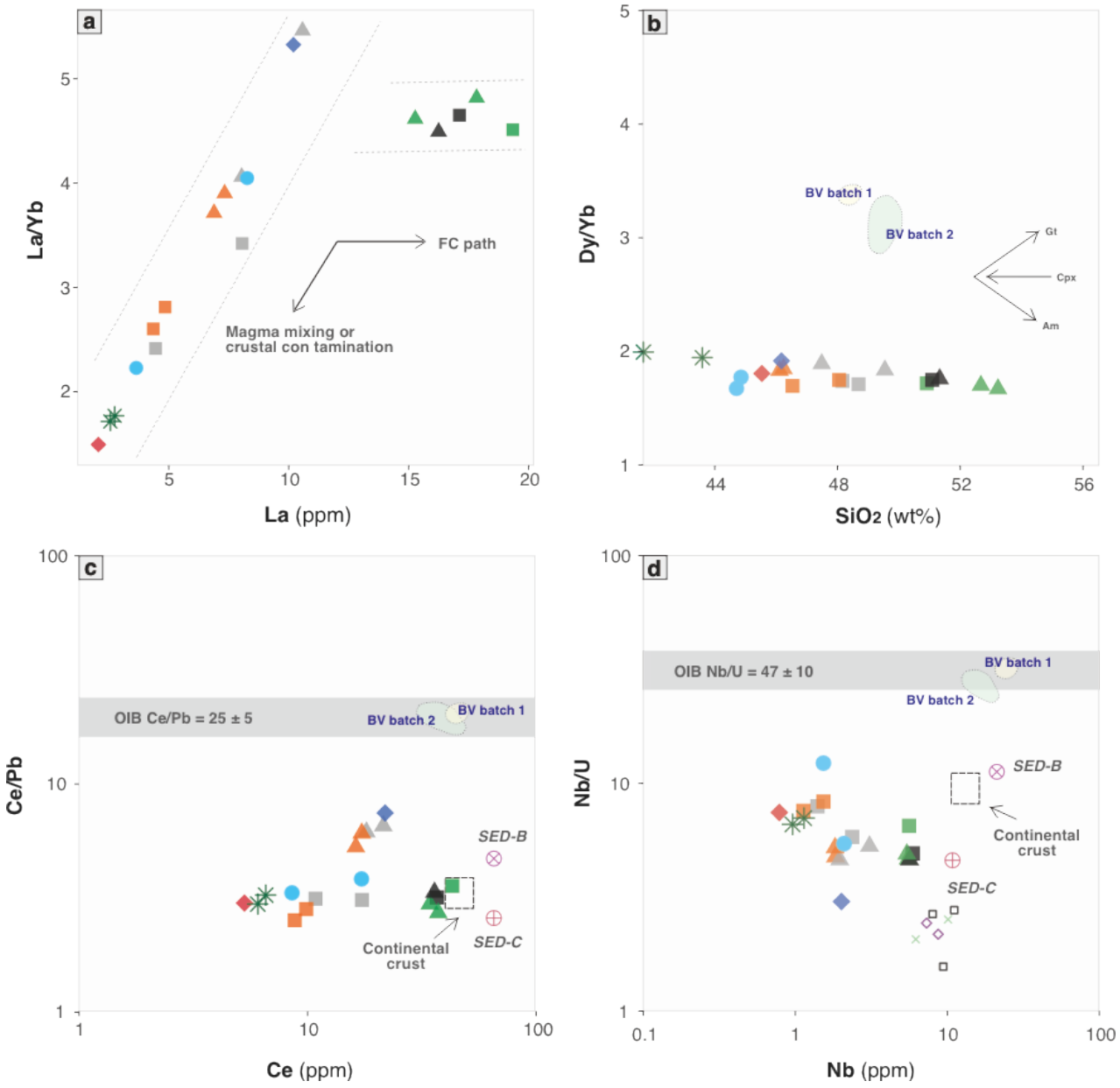

Figure 3. 14. Trace elements ratio plots of samples from LVF maar complex. (**a**) La/Yb vs La (ppm). (**b**) Dy/Yb vs SiO_2. (**c**) Ce/Pb vs. Ce (ppm). (**d**) Nb/U vs Nb (ppm). The shaded field represents OIB (oceanic basalts; Hofmann et al., 1986), while the dashed square represents the average continental crust (Rudnick and Gao, 2003). SED-B and SED-C represent as volcanic sandstone and mudstone, respectively from West Java upper crust sedimentary rocks (Handley et al., 2014).

3.4.2. Mantle source characteristics

The most primitive samples identified in this study are derived from the north scoria cones and east lava, exhibiting low SiO_2 contents (~41 wt% and ~45 wt%, respectively). In particular, the east lava sample displays elevated Ni and Cr contents. As mentioned earlier, the magma composition evolution of each ash types suggests the possibility of fractional crystallization process originating from a similar source, as indicated from silica, sodium, calcium, potassium, and phosphorous content. However, the increasing ratios of trace elements and rare earth elements (REE) concentrations from east lava samples to north scoria cone, gray ash, *cb-pb* ash, *bv* ash, north lava, *bnv* ash, and *ob* ash may be attributed to the enrichment of ash composition through the influence of other process, such as crustal contamination.

The investigation of Nb/Yb, N/La, and Th/Yb ratios is commonly employed to understand and differentiate the composition and origin of magmatic rocks, providing insights into the processes that have influenced the source compositions (Pearce, 1983; Condie, 2003; Cook et al., 2016). The analyzed in this study exhibit a narrow range of Nb/Yb ratios (~0.7-2.5), with a wider range of Th/Yb ratios (~0.2-2.5). Figure 3.13a illustrates that the samples are enriched and deviate from the typical from mantle array. Nche et al., 2021 suggest that this trend may be related to the influence of subduction enrichment and/or crustal contamination on the primitive components (east lava and north scoria cone samples). Notably, the *ob* + *bnv* ash samples show a relative gentle trend (Nb/Yb and Th/Yb = 1), aligning with indications of fractional crystallization. The plot of La/Yb versus Nb/La reveals that LVF samples have relatively low Nb/La (<0.5) ratios, placing them in a lithospheric to average lower crust source. This contrasts with the composition asthenosphere-like source (Nb/La >1) observed in HIMU-OIB and Bahariya volcanic products (Khalaf and Sano, 2020).

The mantle source and depth of melting for LVF samples were modelled using the melting equation by Shaw (1970), in combination with the ratio plots of REE elements. The

samples typically exhibit a low Ce/Yb ratio, which suggests insignificant garnet fractionation in the source rock. This is consistent with low HREE (Ce) fractionation (McKenzie and O'Nions, 1991; Gaetani et al., 2003) and a low Dy/Yb ratio (< 2). The low ratio of Ce/Yb versus La/Ta (not shown) plot for the LVF samples, confirms that the magmas were derived from spinel ± garnet peridotite source in the asthenospheric mantle (Dorais et al., 2017). These results also indicate that the melting process occurred within the stability field of spinel ± garnet peridotite stability field (Fig. 3.13c and 3.13d; La/Yb vs. Sm/Yb and (Ce/Yb) Primitive mantle-normalized vs. Ce). Both diagrams indicate that the primitive samples (east lava and north scoria cone) were produced by more than 20% melting, followed by *cb-pb* + gray + *bv* ash + north lava, which were generated through melting between 20-3%. On the other hand, the *ob* + *bnv* ash samples were produced through a relatively low degree (<5%) of partial melting of spinel peridotite.

3.4.3 Crustal contamination

The ash samples from LVF maar complex exhibit relatively high crystallinity (except for ob ash) which suggest the possibility of residence and/or assimilation within the crust prior to eruption. The interaction of mafic magma and surrounding rocks can lead to compositional modifications, including the addition of incompatible elements such as LILE (Large Ion Lithophile Elements), Th, and LREE (Taylor and McLennan, 1985; Cui et al., 2021).

The ratios of Nb/U and Ce/Pb are commonly used indicators of crustal contamination, as they tend to be higher in the mantle source compared to the continental crust (Rudnick and Gao, 2003). The high Pb contents observed in LVF samples result in low Ce/Pb ratios (~3-9) in comparison to the Ce/Pb ratio of 25 ± 5 observed in OIB (Ocean Island Basalts) (Fig. 3.14c) (Hofmann et al., 1986). Similarly, the high U contents imply low Nb/U ratios (~5-10) compared to the Nb/U ratio of 47 ± 10 observed in OIB (Hofmann, 2007) and the primitive mantle (PM)

ratio of ~37 (Nche et al., 2021). Several samples (scoria, lava, and maar deposits) from Carn and Pyle (2001) display even lower Nb/U ratios ranging from 2-5 (Fig. 3.14d). This indicates that the LVF samples undergone some degree of crustal contamination, approaching the average ratio of the continental crust (Rudnick and Gao, 2003).

The La/Yb ratio versus La (ppm) plots in Figure 3.14a show two distinct trends. The steep La/Yb trend suggest the influence of magma mixing or crustal contamination, which played a significant role in the differentiation of the magma composition within the LVF maar complex. This trend may also indicate an increasing amount of partial melting from the most primitive samples (east lava and north scoria cone) to ash samples (Thirlwall et al., 1994). On the other hand, the relative flat La/Yb trend observed in the *ob* and *bnv* ash particles indicates that these samples follow the fractional crystallization path.

Furthermore, the Th/Yb versus Nb/Yb ratios (Fig. 3.14b) (Pearce, 2008) are commonly used to assess variations in the mantle source compositions. Th and Nb are highly incompatible elements, while Yb is not significantly affected by partial melting and fractional crystallization process (Pearce and Peate, 1995). Figure 3.13a provides evidence of compositional variation within LVF maar complex, suggesting an enrichment source due to crustal contamination/assimilation-fractional crystallization (AFC) processes, as well as potential modification by subduction components together with fractional crystallization (FC) from a similar parental magma source.

In Figure 3.15, selected major element compositions of LVF samples are presented alongside MELTS models. The MELTS simulations were conducted using the PELE v.8.00 software, which is a version of the silicate liquid crystallization MELTS software program for the PC platform (Boudreau, 1999). The north scoria cone sample (22-5sc) was chosen as the starting composition for the models due to its possibility as the closest major elements composition to a parental magma (7.5 wt% MgO and 41.4 wt% SiO_2). The models were

calculated under isobaric conditions at different pressures (4 and 8 kbar), with varying initial H_2O-melt contents (0.5 and 1.5 wt%), fixed oxygen fugacity relative to QFM buffer, and the starting temperature based on the liquidus temperature obtained from the software.

To account for assimilation of continental crust, the composition of the SED-B (volcanic sandstone) from West Java upper crust sedimentary rocks (Handley et al., 2014) was used as the contaminant. Approximately 0.5 grams of assimilated material was added during each iteration (~50 iterations). The results obtained from the MELTS models demonstrate that that the trends of fractional crystallization (FC) and assimilation fractional crystallization (AFC) differ in terms of compositions and mineral assemblages.

As observe in the Figure 3.15, the FC models generally exhibit gentle slopes (e.g. SiO_2, Na_2O, CaO) with respect to changing MgO concentrations, which do not explain the steep slopes observed in the LVF maar complex samples. In this regard, the samples are better reproduced by the AFC models than the FC models. However, with an initial H_2O-melt content of 0.5 % (AFC model I and III), the LVF maar magma is best simulated, with the following fractionated phase: spinel + high Ca pyroxene + plagioclase + olivine ± low Ca pyroxene ± apatite. The use of higher initial H_2O-melt content (> 0.8%) in the parental magma for modelling seems to preclude olivine fractionation (e.g. model II and IV). Furthermore, notable discrepancies between the models and FeO* and TiO contents for ob and bv ash samples may be attributed to the absence of mineral fractionation of Fe-Ti oxides.

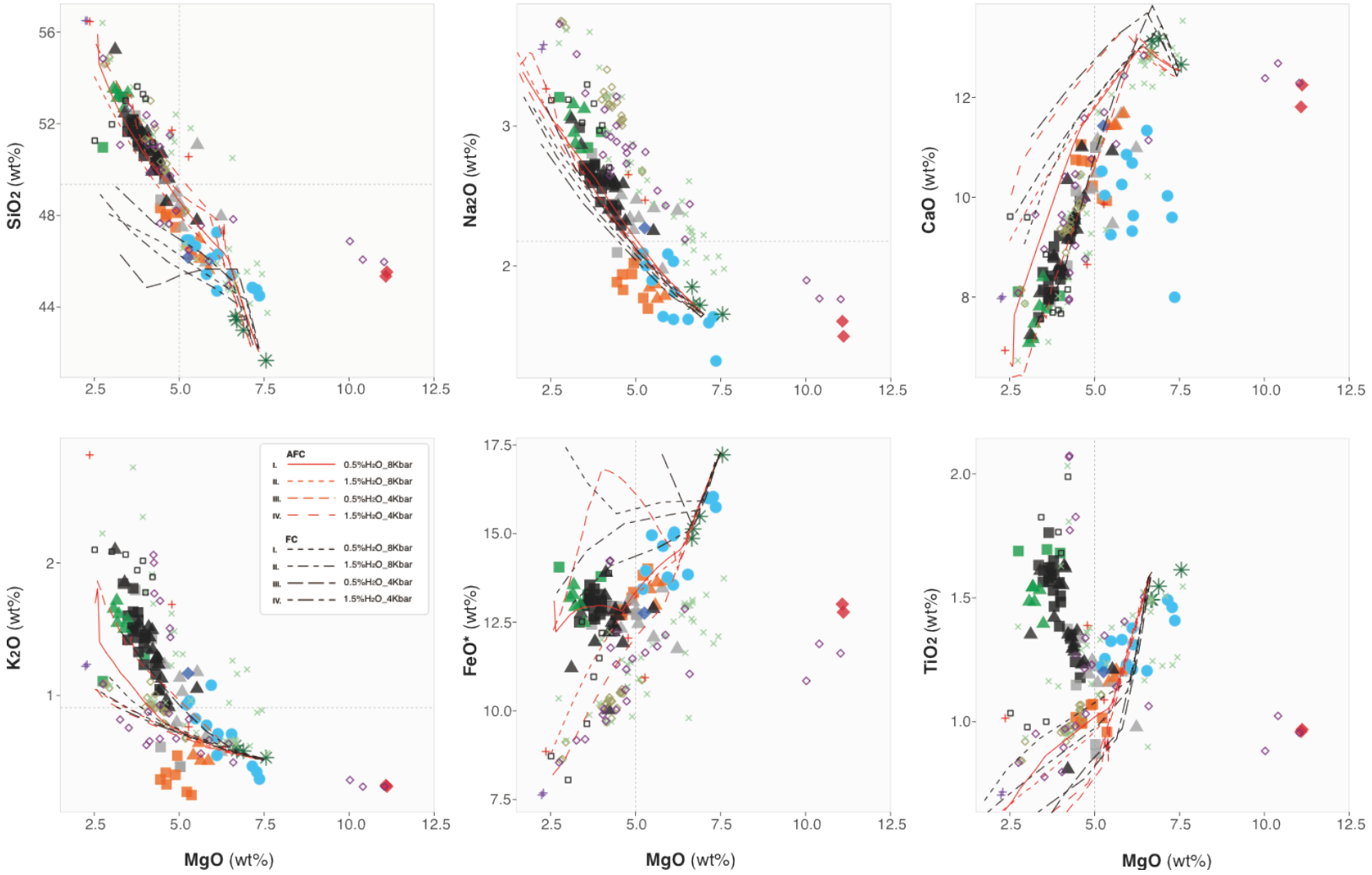

Figure 3. 15. Concentration of selected major elements versus MgO (wt%) for samples from LVF complex. The curves represent the evolution path of residual melts modelled using PELE software v.8.0 (a version of the silicate liquid crystallization MELTS software program for the PC platform by Boudreau, 1999). The simulations were carried out based on two differentiation models: fractional crystallization (FC) and assimilation fractional crystallization (AFC); see the text for the parameters used in the simulation.

3.4.4. Concluding remarks: The origin of ash particle

The analysis of major and trace elements in the volcanic ash based on the component framework from the LVF maar complex provides insights into its origin. The variations observed can be attributed to the processes of fractional crystallization and crustal assimilation. The magmas in the maar complex are derived from the melting of spinel ± garnet peridotite source, which then rise and assimilate crustal material while undergoing continued fractional crystallization. This scenario explains the evolution of eruption products observed in different ash types (*ob*, *bnv* < *bv*, *cb-pb*, gray). Additionally, pyroxene geothermobarometry was used to determine the temperature and pressure condition of each ash type, providing further support for the proposed scenario (Cpx only and Cpx-whole rock; Table 3.1). The primitive magma, represented by the north scoria cone, serves as the parental magma that stalled at various depths and undergo a specific process before erupting (Fig. 3.16). The *cb-pb*, *bv*, and gray ash magmas, which represent mafic end-members, are stored at relatively deeper crustal levels (3.1-8.6 kbar; 1085-1186°C) and have experienced assimilation fractional crystallization (AFC). On the other hand, the *ob* and *bnv* ash magmas, representing felsic-and members, indicate a shallower crustal storage (1.6-6.2 kbar; 1094-1140°C) and have predominantly undergone fractional crystallization (FC). Furthermore, Lamongan lavas (north and east) display a different magmatic system and storage conditions (6.5-8.6 kbar; 1124-1215°C), likely involving more complex processes such as magma chamber stratification, recharge, assimilation, and mixing. It worth nothing that the magma of the north scoria cone (average 5.95 kbar; 1136°C) is considered as the least differentiated and least affected magma by contamination and other processes due to its relatively short storage time before reaching the surface.

Figure 3.6 provides a spatial perspective on the characteristics of each maar within the LVF maar complex, highlighting their potential individual characteristics. In general, the east maars exhibit lower silica and magnesium content compared to those in the west and north

maars. This trend also observed in the pre-historic lava, spatter/scoria cone, historical lava, and maar deposits studied by Carn and Pyle (2001), suggesting a progressive evolution tendency of the LVF complex as whole. Carn and Pyle (2001) noted that there is a geochemical variation between cinder cone clusters within this complex, with the western cluster (KVT) potentially associated with the most enriched and least metasomatized mantle source compared to the eastern LVF cones. To further understand the spatial and temporal heterogeneities of the mantle source and the independent processes involved in each maar (such as fractionation, segregation, and ascent mechanisms), more detailed geochemical and isotope studies with high-resolution sampling of each center are needed.

The geochemical study on ash particles from the LVF maar complex has highlighted the significance of basic component analysis on the fine-sized eruption products. This approach revealed consistent geochemical properties within the ash sample types. Accordingly, this study offers the potential to obtain valuable geochemical data on the explosive eruptions that yield ash-dominated products. Such data can greatly contribute to our understanding of magmatic system associated with the dynamics of explosive eruptions.

Table 3. 1. Geothermobarometer calculation results for the LVF maar complex samples. Values of temperature and pressure are given as average and range.

		Ash types		bv			bnv			cb-pb			ob		
		Minerals	**Model**	T (C)	P (kbar)	n	T (C)	P (kbar)	n	T (C)	P (kbar)	n	T (C)	P (kbar)	n
West Region	Ranu Pakis	Cpx-whole rock	I	1156 (±28)	6.34 (±2.0)	6	1129 (±55)	3.7 (±1.4)	3	1085	5.3	1			
		Cpx only	II	-	-	-	1111 (±48)	4.5 (±0.7)	3	-	-	-			
		Cpx only	III	-	-	-	-	-	-	1133	4.6	1			
	Ranu Klakah	Cpx-whole rock	I	1167 (±63)	8.65 (±3.7)	14	1112 (±9.5)	3.8 (±0.5)		1137	6.3	1			
		Cpx only	II	-	-	-	-	-	-	1116 (±53)	3.2 (±4.1)				
North Maar	Ranu Kering	Cpx-whole rock	I	1158 (±49)	3.16 (±0.1)	3	1115	2.4	1	1121	3.53	1	1104 (±10)	3.0 (±1.5)	3
		Cpx only	II	1133 (±13)	3.7 (±2.1)	3	1110 (±14)	1.6 (±0.8)	2	-	-	-			
	Ranu Air	Cpx-whole rock	I	1132	5.6	1	1140 (±12)	4.2 (±2.0)	2	1158	7.7 (±0.2)	2			
		Cpx only	II	-	-	-	1094 (±27)	6.2 (±1.0)	3	1154 (±33)	5.6 (±2.3)	2			
				gray ash											
East Maar	o.n Ranu Kembar	Cpx-whole rock	I	1114 (±9)	5.5 (±0.8)	3									
		Cpx only	III	1150 (±13)	5.3 (±1.5)	2									
	Ranu Segaran	Cpx only	II	1186 ± (9)	6.4 (±1.7)	3									
				black scoria (lapilli)											
North scoria cone		Cpx-whole rock	I	1136 (±23)	5.95 (±1.4)	31									
				lava fragments											
North Lava		Cpx only	I	1124 (±9.5)	6.5 (±0.7)	19									
East Lava		Cpx only	II	1215 (±23)	8.6 (±1.9)	34									

Model	
I	Putirka (2008); Neave and Putirka (2017)
II	Putirka (2008) (Equation 32a & 32d)
III	Putirka (2008) (Equation 32c & 32d)

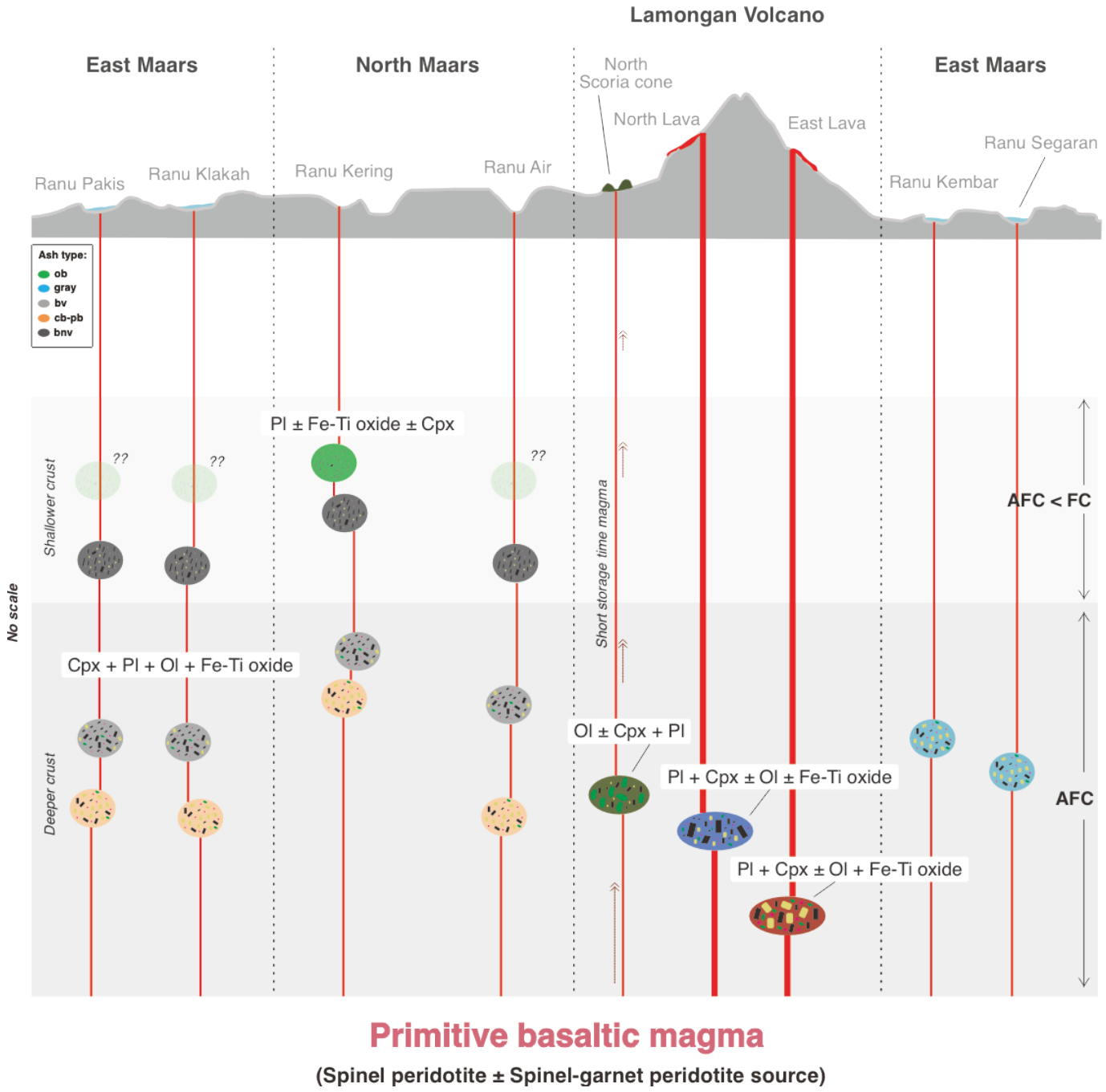

Figure 3. 16. Diagram of simplified magma petrogenesis at the LVF maar complex. Cross-section shown a spatial distribution of maars in the complex, along with Lamongan volcano. The diagram shows the presence of multi-level magma storage as the source heterogeneity observe in ash particles. Deeper-level magma storage is responsible for the formation of cb-pb, bv, and gray ash magmas, which have undergone varying degrees of assimilation fractional crystallization (AFC). In contrast, the ob and bnv ash magmas originate from a shallower level and have predominantly experienced fractional crystallization (FC). Lamongan lavas (north and east) exhibit distinct magmatic systems and storage conditions, involving more complex processes. The north scoria cone is likely to represent the least differentiated magma due to its shorter storage time.

3.5. REFERENCE

Beaumais, A., Bertrand, H., Chazot, G., Dosso, L., & Robin, C. (2016). Temporal magma source changes at Gaua volcano, Vanuatu island arc. *Journal of Volcanology and Geothermal Research*, *322*, 30–47. https://doi.org/10.1016/j.jvolgeores.2016.02.026

Brenna, M., Cronin, S. J., Smith, I. E. M., Sohn, Y. K., & Németh, K. (2010). Mechanisms driving polymagmatic activity at a monogenetic volcano, Udo, Jeju Island, South Korea. *Contributions to Mineralogy and Petrology*, *160*(6), 931–950. https://doi.org/10.1007/s00410-010-0515-1

Boudreau, A. E. (1999). PELE-a version of the MELTS software program for the PC platform. *Computers and Geosciences*, *25*(2), 201–203. https://doi.org/10.1016/S0098-3004(98)00117-4

Carn, S. A. (2000). The Lamongan volcanic field, East Java, Indonesia: Physical volcanology, historic activity and hazards. *Journal of Volcanology and Geothermal Research*, *95*(1–4), 81–108. https://doi.org/10.1016/S0377-0273(99)00114-6

Carn, S. A., & Pyle, D. M. (2001). Petrology and geochemistry of the Lamongan volcanic field, East Java, Indonesia: Primitive Sunda arc magmas in an extensional tectonic setting? *Journal of Petrology*, *42*(9), 1643–1683. https://doi.org/10.1093/petrology/42.9.1643

Chako-Tchamabé, B., Carrasco-Núñez, G., Gountié Dedzo, M., Kshirsagar, P., & Asaah, A. N. E. (2020). Geochemical characterization of alchichica maar volcano, Serdán-oriental Basin, eastern Trans-Mexican Volcanic Belt: Insights on polymagmatic evolution at monogenetic volcanic clusters. *Journal of South American Earth Sciences*, *104*. https://doi.org/10.1016/j.jsames.2020.102889

Cioni, R., Civetta, L., Marianelli, P., Metrich, N., Santacroce, R. and Sbrana, A., 1992. Compositional layering and syn-eruptive mixing of a periodically refilled shallow magma chamber: the AD 79 Plinian eruption of Vesuvius. Journal of Petrology, 33(4), pp.739-776. https://doi.org/10.1093/petrology/36.3.739

Condie, K. C. (2003). Incompatible element ratios in oceanic basalts and komatiites: Tracking deep mantle sources and continental growth rates with time. *Geochemistry, Geophysics, Geosystems*, *4*(1). https://doi.org/10.1029/2002GC000333

Cook, C., Briggs, R. M., Smith, I. E. M., & Maas, R. (2005). Petrology and geochemistry of intraplate basalts in the South Auckland Volcanic Field, New Zealand: Evidence for two coeval magma suites from distinct sources. *Journal of Petrology*, *46*(3), 473–503. https://doi.org/10.1093/petrology/egh084

Cook, Y. A., Sanislav, I. v., Hammerli, J., Blenkinsop, T. G., & Dirks, P. H. G. M. (2016). A primitive mantle source for the Neoarchean mafic rocks from the Tanzania Craton. *Geoscience Frontiers*, *7*(6), 911–926. https://doi.org/10.1016/j.gsf.2015.11.008

Coote, A., & Shane, P. (2018). Open-system magmatic behaviour beneath monogenetic volcanoes revealed by the geochemistry, texture and thermobarometry of clinopyroxene, Kaikohe-Bay of Islands volcanic field (New Zealand). *Journal of Volcanology and Geothermal Research*, *368*, 51–62. https://doi.org/10.1016/j.jvolgeores.2018.11.006

Cui, X., Sun, M., Zhao, G., Zhang, Y., & Yao, J. (2021). Two-Stage Mafic-Felsic Magma Interactions and Related Magma Chamber Processes in the Arc Setting: An Example From the Enclave-Bearing Calc-Alkaline Plutons, Chinese Altai. *Geochemistry, Geophysics, Geosystems*, *22*(12). https://doi.org/10.1029/2021GC009939

Dorais, M. J., Marvinney, R. G., & Markert, K. (2017). The age, petrogeneis and tectonic significance of the frontenac formation basalts, northern New Hampshire and western Maine. *American Journal of Science*, *317*(9), 990–1018. https://doi.org/10.2475/09.2017.02

Dorendorf, F., Churikova, T., Koloskov, A., & Wo Èrner, G. (2000). Late Pleistocene to Holocene activity at Bakening volcano and surrounding monogenetic centers (Kamchatka): volcanic geology and geochemical evolution. *Journal of Volcanology and Geothermal Research*, *104*, 131-151. https://doi.org/10.1016/S0377-0273(00)00203-1.

Gaetani, G. A., Kent, A. J. R., Grove, T. L., Hutcheon, I. D., & Stolper, E. M. (2003). Mineral/melt partitioning of trace elements during hydrous peridotite partial melting.

Contributions to Mineralogy and Petrology, *145*(4), 391–405. https://doi.org/10.1007/s00410-003-0447-0

Hamilton, W., 1979. Tectonics of the Indonesian region. US Government Printing Office.

Handley, H. K., Macpherson, C. G., Davidson, J. P., Berlo, K., & Lowry, D. (2007). Constraining fluid and sediment contributions to subduction-related magmatism in Indonesia: Ijen Volcanic Complex. *Journal of Petrology*, *48*(6), 1155–1183. https://doi.org/10.1093/petrology/egm013

Handley, H. K., Blichert-Toft, J., Gertisser, R., Macpherson, C. G., Turner, S. P., Zaennudin, A., & Abdurrachman, M. (2014). Insights from Pb and O isotopes into along-arc variations in subduction inputs and crustal assimilation for volcanic rocks in Java, Sunda arc, Indonesia. *Geochimica et Cosmochimica Acta*, *139*, 205–226. https://doi.org/10.1016/j.gca.2014.04.025

Hofmann, A. W. (2007). Sampling Mantle Heterogeneity through Oceanic Basalts: Isotopes and Trace Elements. In *Treatise on Geochemistry* (Vols. 2–9, pp. 1–44). Elsevier Inc. https://doi.org/10.1016/B0-08-043751-6/02123-X

Hofmann, W., Jochum, K. P., Seufert, M., & White, W. M. (1986). Nb and Pb in oceanic basalts: new constraints on mantle evolution. In *Earth and Planetary Science Letters* (Vol. 79).

Jankovics, M. É., Harangi, S., Németh, K., Kiss, B., & Ntaflos, T. (2015). A complex magmatic system beneath the Kissomlyó monogenetic volcano (western Pannonian Basin): Evidence from mineral textures, zoning and chemistry. *Journal of Volcanology and Geothermal Research*, *301*, 38–55. https://doi.org/10.1016/j.jvolgeores.2015.04.010

Khalaf, E. E. D. A. H., & Sano, T. (2020). Petrogenesis of Neogene polymagmatic suites at a monogenetic low-volume volcanic province, Bahariya depression, Western Desert, Egypt. *International Journal of Earth Sciences*, *109*(3), 995–1027. https://doi.org/10.1007/s00531-020-01849-1

Kirchenbaur, M., Schuth, S., Barth, A. R., Luguet, A., König, S., Idrus, A., Garbe-Schönberg, D., & Münker, C. (2022). Sub-arc mantle enrichment in the Sunda rear-arc inferred from

HFSE systematics in high-K lavas from Java. *Contributions to Mineralogy and Petrology*, *177*(1). https://doi.org/10.1007/s00410-021-01871-9

Kugaenko, Y., & Volynets, A. O. (2019). Magmatic plumbing systems of the monogenetic volcanic fields: A case study of Tolbachinsky Dol, Kamchatka. *Journal of Volcanology and Geothermal Research*, *383*, 63–76. https://doi.org/10.1016/j.jvolgeores.2018.03.015

Larrea, P., Widom, E., Siebe, C., Salinas, S., & Kuentz, D. (2019). A re-interpretation of the petrogenesis of Paricutin volcano: Distinguishing crustal contamination from mantle heterogeneity. *Chemical Geology*, *504*, 66–82. https://doi.org/10.1016/j.chemgeo.2018.10.026

Liu, B., Ma, C. Q., Zhang, J. Y., Xiong, F. H., Huang, J., & Jiang, H. A. (2014). 40Ar-39Ar age and geochemistry of subduction-related mafic dikes in northern Tibet, China: Petrogenesis and tectonic implications. *International Geology Review*, *56*(1), 57–73. https://doi.org/10.1080/00206814.2013.818804

Lötter, F. J. P., Lenhardt, N., Viereck, L., Münker, C., Marien, C. S., & Altigani, M. A. H. (2022). The Quaternary monogenetic Bayuda Volcanic Field, Sudan – Insights into mantle and crustal processes during magma petrogenesis. *Lithos*, *410–411*. https://doi.org/10.1016/j.lithos.2021.106563

McGee, L. E., Beier, C., Smith, I. E. M., & Turner, S. P. (2011). Dynamics of melting beneath a small-scale basaltic system: A U-Th-Ra study from Rangitoto volcano, Auckland volcanic field, New Zealand. *Contributions to Mineralogy and Petrology*, *162*(3), 547–563. https://doi.org/10.1007/s00410-011-0611-x

McKenzie D, O'Nions RK (1991) Partial melt distributions from inversion of rare Earth element concentrations. *Journal of Petrology*, *32*, 1021–1091. https://doi.org/10.1093/petrology/32.5.1021

Moore, N. E., Grunder, A. L., Bohrson, W. A., Carlson, R. W., & Bindeman, I. N. (2020). Changing Mantle Sources and the Effects of Crustal Passage on the Steens Basalt, SE Oregon: Chemical and Isotopic Constraints. *Geochemistry, Geophysics, Geosystems*, *21*(8). https://doi.org/10.1029/2020GC008910

Nche, L. A., Hasegawa, T., Aka, F. T., Kobayashi, T., Németh, K., Asaah, A. N. E., Kaneda, Y., Nishihara, A., Bate-Tibang, E. E., Lebga, A. K., Tiabou, A. F., Ngwa, C. N., & Suh, C. E. (2021). Lithostratigraphy and geochemistry of Aojiki volcano and Sumiyoshiike and Yonemaru maars, Kamo Volcanic Field (Southern Kyushu), Japan. *Journal of Volcanology and Geothermal Research*, *412*. https://doi.org/10.1016/j.jvolgeores.2020.107170

Neave, D. A., & Putirka, K. D. (2017). A new clinopyroxene-liquid barometer, and implications for magma storage pressures under Icelandic rift zones. *American Mineralogist*, *102*(4), 777–794. https://doi.org/10.2138/am-2017-5968

Németh, K., White, J. D. L., Reay, A., & Martin, U. (2003). Compositional variation during monogenetic volcano growth and its implications for magma supply to continental volcanic fields. *Journal of the Geological Society*, *160*(4), 523–530. https://doi.org/10.1144/0016-764902-131

Németh, K., & Kereszturi, G. (2015). Monogenetic volcanism: personal views and discussion. *International Journal of Earth Sciences*, *104*(8), 2131–2146. https://doi.org/10.1007/s00531-015-1243-6

Óladóttir, B. A., Larsen, G., & Sigmarsson, O. (2012). Deciphering eruption history and magmatic processes from tephra in Iceland. In *Jokull* (Vol. 2012, Issue 62, pp. 21–38). Iceland Glaciological Society. https://doi.org/10.33799/jokull2012.62.021

Óladóttir, B. A., Sigmarsson, O., Larsen, G., & Thordarson, T. (2008). Katla volcano, Iceland: Magma composition, dynamics and eruption frequency as recorded by Holocene tephra layers. *Bulletin of Volcanology*, *70*(4), 475–493. https://doi.org/10.1007/s00445-007-0150-5

Özdemir, Y., & Güleç, N. (2014). Geological and geochemical evolution of the quaternary süphan stratovolcano, Eastern Anatolia, Turkey: Evidence for the lithosphere-asthenosphere interaction in post-collisionalvolcanism. *Journal of Petrology*, *55*(1), 37–62. https://doi.org/10.1093/petrology/egt060

Pearce, J. A. (1983) Role of the sub-continental lithosphere in magma genesis at active continental margins. pp 230–249

Pearce, J. A. (2008). Geochemical fingerprinting of oceanic basalts with applications to ophiolite classification and the search for Archean oceanic crust. *Lithos*, *100*(1–4), 14–48. https://doi.org/10.1016/j.lithos.2007.06.016

Pearce, J. A., and Peate, D. W. (1995). Tectonic implications of the composition of volcanic arc magmas. *Annual Review of Earth and Planetary Sciences. 23*, 251-285. https://doi.org/10.1146/annurev.ea.23.050195.001343

Preece, K., Gertisser, R., Barclay, J., Berlo, K., Herd, R. A., & Edinburgh Ion Microprobe Facility. (2014). Pre- and syn-eruptive degassing and crystallisation processes of the 2010 and 2006 eruptions of Merapi volcano, Indonesia. *Contributions to Mineralogy and Petrology*, *168*(4), 1–25. https://doi.org/10.1007/s00410-014-1061-z

Putirka, K. D. (2008). Thermometers and barometers for volcanic systems. *Reviews in Mineralogy and Geochemistry*, *69*, 61–120. https://doi.org/10.2138/rmg.2008.69.3

Rasoazanamparany, C., Widom, E., Siebe, C., Guilbaud, M. N., Spicuzza, M. J., Valley, J. W., Valdez, G., & Salinas, S. (2016). Temporal and compositional evolution of Jorullo volcano, Mexico: Implications for magmatic processes associated with a monogenetic eruption. *Chemical Geology*, *434*, 62–80. https://doi.org/10.1016/j.chemgeo.2016.04.004

Rasoazanamparany, C., Widom, E., Kuentz, D., Raharimahefa, T., Rakotondravelo, K., & Rakotondrazafy, A. M. F. (2021). Geochemistry and mantle source characteristics of the itasy volcanic field: Implications for the petrogenesis of basaltic magmas in intra-continental-rifts. *Geochimica et Cosmochimica Acta*, *300*, 137–163. https://doi.org/10.1016/j.gca.2021.02.025

Romero, J. E., Ureta, G., Fuentes, P., Corgne, A., Naranjo, J. A., Ramírez, C. F., Chako-Tchamabé, B., Cáceres, M., & Lazcano, J. (2022). The eruptive history and magma composition of Pleistocene Cerro Negro volcano (Northern Chile): Implications for the complex evolution of large monogenetic volcanoes. *Journal of Volcanology and Geothermal Research*, *429*. https://doi.org/10.1016/j.jvolgeores.2022.107618

Rudnick, R.L. and Gao, S. (2003) The Composition of the Continental Crust. In: Holland, H.D. and Turekian, K.K., Eds., Treatise on Geochemistry, Vol. 3, The Crust, Elsevier Pergamon, Oxford, 1-64.http://dx.doi.org/10.1016/b0-08-043751-6/03016-4

Sun, S. -s., & McDonough, W. F. (1989). Chemical and isotopic systematics of oceanic basalts: implications for mantle composition and processes. *Geological Society, London, Special Publications, 42(1), 313–345* https://doi.org/10.1144/GSL.SP.1989.042.01.19

Taylor, S. R., and McLennan, S. M. (1985) The continental crust: Its composition and evolution. United States: N. p., 1985.

Thirlwall, M. F., Smith, T. E., Graham, A. M., Theodorou, N., Hollings, P., Davidson, J. P., & Arculus, R. J. (1994). High Field Strength Element Anomalies in Arc Lavas: Source or Process?. *Journal of Petrology*, *35*(3), 819-838. https://doi.org/10.1093/petrology/35.3.819

Torres-Sánchez, D., Sosa-Ceballos, G., Bolós, X., & Macías, J. L. (2022). Petrogenesis of mafic-intermediate magmatism of the Michoacán–Guanajuato volcanic field in Western Mexico. A geochemical review. In *Frontiers in Earth Science* (Vol. 10). Frontiers Media S.A. https://doi.org/10.3389/feart.2022.932588

Ureta, G., Németh, K., Aguilera, F., Kósik, S., González, R., Menzies, A., González, C., & James, D. (2021). Evolution of a magmatic to a phreatomagmatic volcanic system: The birth of a monogenetic volcanic field, Tilocálar volcanoes, northern Chile. *Journal of Volcanology and Geothermal Research*, *414*. https://doi.org/10.1016/j.jvolgeores.2021.107243

Ureta, G., Németh, K., Aguilera, F., Zimmer, M., & Menzies, A. (n.d.). *A window on mantle-derived magmas within the Central Andes: eruption style transitions at Cerro Overo maar and La Albóndiga lava dome, northern Chile*. https://doi.org/10.1007/s00445-021-01446-3/Published

Van Gerven, M., & Pichler, H. (1995). Some aspects of the volcanology and geochemistry of the Tengger Caldera, Java, Indonesia: eruption of a K-rich tholeiitic series. In *Journal Sourheast Asian Earth Sciences* (Issue 2).

Van Otterloo, J., Cas, R. A. F., & Sheard, M. J. (2013). Eruption processes and deposit characteristics at the monogenetic Mt. Gambier Volcanic Complex, SE Australia: Implications for alternating magmatic and phreatomagmatic activity. *Bulletin of Volcanology*, *75*(8), 1–21. https://doi.org/10.1007/s00445-013-0737-y

Varol, E., Temel, A., Yürür, T., Gourgaud, A., & Bellon, H. (2014). Petrogenesis of the Neogene bimodal magmatism of the Galatean Volcanic Province, Central Anatolia, Turkey. *Journal of Volcanology and Geothermal Research*, *280*, 14–29. https://doi.org/10.1016/j.jvolgeores.2014.04.014

White, J. C., Neave, D. A., Rotolo, S. G., & Parker, D. F. (2020). Geochemical constraints on basalt petrogenesis in the Strait of Sicily Rift Zone (Italy): Insights into the importance of short lengthscale mantle heterogeneity. *Chemical Geology*, *545*. https://doi.org/10.1016/j.chemgeo.2020.119650

Chapter IV - Ash aggregate diversity and formation processes in phreatomagmatic eruptions: Evidence from the Ranu Klakah maar, Lamongan Volcanic Field (LVF), Indonesia

4.1. INTRODUCTION

Ash aggregation is a common process in phreatomagmatic eruptions, in which fine volcanic particles adhere and accrete into larger aggregates (Brown et al., 2010). The eruptions result from the interaction between external water and rising magma, which generates wet, turbulent eruption plumes. The eruption promotes moisture condensation and electrostatic forces, enabling fine ash particles to collide and stick together (James et al., 2003; Van Eaton et al., 2012). Aggregation reduces the dispersal of fine ash, promoting more proximal deposition and altering atmospheric sedimentation rates (Rose & Durant, 2011; Telling et al., 2013; Zhu et al., 2020; Rossi et al., 2021). Additionally, aggregates' internal structure and exterior rims provide evidence of eruption dynamics, water availability, and phreatomagmatic intensity (Schumacher & Schmincke, 1991; Mueller et al., 2016).

Particle aggregation is most efficient in wet, turbulent plumes containing abundant condensed water droplets. The presence of liquid water promotes moisture adhesion and the accretion of fine particles (<64 μm) into larger aggregates (Gilbert & Lane, 1994; Van Eaton et al., 2012), which is common with progressive growth layer-by-layer (Brown et al., 2010). This process results in diverse aggregates of textures. The textures range from massive and unstructured forms lacking internal laminations to well-laminated concentric aggregates (e.g. Moore and Peck, 1962; Schumacher & Schmincke, 1991; 1995; Brown et al., 2010). Mueller et al. (2016) suggest that the abundance of ash aggregates in pyroclastic deposits indicates the phreatomagmatic intensity; well-laminated aggregates (accretionary lapilli) signify explosive wet eruptions, while massive unstructured ash pellets suggest a periodic shift to drier conditions. In addition, aggregates frequently contain recycled lithic clasts and hydrothermally altered

materials from prior eruptions, which were incorporated through vent-clearing explosions (Mueller et al., 2017; Thivet et al., 2020).

Although prior research has provided important insights into ash aggregation processes, there still needs to be more understanding regarding the relationship between aggregate characteristics and evolving phreatomagmatic eruption dynamics in maar volcanoes and their hazard implications. Furthermore, a thorough analysis of the significance of complex ash components present in aggregates is required, particularly regarding the role of recycled altered clasts originating from previous eruptive activity or hydrothermal alteration processes. This study aims to characterize variations in ash aggregate attributes preserved in erupted products at Ranu Klakah maar, to better constrain changing eruption dynamics over time and improve the assessment of volcanic hazards.

Three stratified pyroclastic units at Ranu Klakah maar preserve changing eruptive conditions within Lamongan Volcanic Field (LVF). These units were characterized by microtextural, componentry, morphometric, mineralogical, and geochemical analyses. These integrated results aim to reconstruct fluctuation in eruption styles, the aggregation process, and the role of recycled or altered materials in changing eruption dynamics. Our study provides new insights into how the ash aggregation tracked and fingerprinted shifts phreatomagmatic activity. Such results enhance our understanding of the past eruptive evolution of maar eruptions and help address aggregation-eruption links, with implications for hazard assessment in this region.

4.2. METHODS

Samples were collected from maar crater outcrops in the Lamongan Volcanic Field (LVF) in East Java, Indonesia. The sampling locations included the Ranu Klakah, Ranu Kembar, and an outcrop NE of Ranu Air maars. Detailed stratigraphic sections were identified

at each maar outcrop, focusing on the deposits of Ranu Klakah, which displayed the most complete sequence of stratigraphic units. Ash aggregate-bearing layers were targeted for sampling across multiple stratigraphic units at Ranu Klakah in order to identify the variations in aggregates (e.g. type, distribution) across the entire eruption sequence. Due to their incomplete stratigraphic exposures, more limited sampling was undertaken at Ranu Kembar and an outcrop northeast of Ranu Air maars.

The deposits are generally dense and compact to extract intact accretionary lapilli samples. The samples of ash aggregate-bearing layer were epoxy-impregnated and prepared as polished thin sections for detailed observation of ash aggregate features. The polish thin section samples were observed using an optical microscope and SEM imaging. The aggregate types were categorized based on internal textures, clast components, and coating or rims. The relative proportion of the ash aggregate types was observed in the tephra layer samples and polish thin sections. SEM imaging supplemented the optical analysis, providing higher resolution details, including texture and dimension.

The 125-250 μm grain size ash components from each ash aggregate-bearing layer were prepared into thin sections. The relative abundances of juvenile clasts (black non-vesicular [*bnv*], black vesicular [*bv*], clear-brown [*cb*], pale-brown [*pb*], and orange-brown [*ob*]) and non-juvenile clasts (ash aggregates [*aa*], free-crystal [*fc*], and altered/weathered clast [*alt*]) were quantified by point counting from each thin section sample (>2000 grains per sample). Additionally, the same samples were used for morphometric (shape) analysis on individual ash particles from each type (fc and alt clasts were excluded). We used the CorelDraw software to manually trace particle outlines, from which the shape parameters could be calculated. Key shape parameters (Liu et al., 2015) quantified using PARTISAN software (Dürig et al., 2018) included convexity, solidity, and form factor for all juvenile clast types.

The bulk and clay mineralogy of intact accretionary lapilli were analyzed by X-ray diffraction (XRD) methods. SEM-EDS analysis was performed to identify the mineral compositions. In addition, elemental mapping was used to determine the compositional zoning within individual aggregates, targeting the distinct rim, mantle, and core areas.

4.3. RESULTS

4.3.1. Stratigraphy and tephra units

The examined deposits display a detailed stratigraphy from Ranu Klakah, Ranu Air, and an outcrop northeast of Ranu Kembar maar crater, comprising multiple alternating sequences of medium-coarse ash to lapilli layers (Fig. 4.1a). Based on the observed lithological variations, the deposits are categorized into three tephra units (Units 1-3), as labeled in Figure 4.1. The most complete sequence comprising all three units is present at Ranu Klakah maar. Ranu Air maar contains only Unit 2 deposits, while the northeast Ranu Kembar outcrop contains Units 2 and 3.

Unit 1 is characterized by interbedded coarse ash to lapilli layers with modest weathering. The unit displays a repetition of the fining upward grain size trend. It possesses a matrix-supported structure with scattered lithic clasts up to 3-5 cm near the base. Ash aggregates less than 5 mm in diameter occur but are relatively sparse, primarily within finer-grained portions.

Unit 2 comprises interbedded coarse ash to lapilli layers with abundant ash aggregates. It has a gray-brownish color and is matrix-supported and compact. Both coarsening and fining upward grain size trends are exhibited at different stratigraphic levels. More abundant lithics ranging from 0.3 to 3 cm are present in lower portions. The uppermost layers of Unit 2 (e.g. layers 4-5, 4-6) are dominated by medium ash with sparse lithic and contain abundant ash aggregates under 3 mm in diameter.

Medium ash-rich grain layers with grain-supported texture and lithic-rich constituents characterize unit 3. Ash aggregated less than 2 mm in diameter occurs but is sparse, primarily within finer-grained thin layers.

4.3.2. Ash aggregate types

Detailed optical analysis (Fig. 4.2) revealed a diverse assemblage of ash aggregate varieties within the phreatomagmatic deposits at the Ranu Klakah maar. Figure 4.3 illustrates three predominant aggregate types based on their internal structures, exterior coatings, and constituent clast components: accretionary lapilli, ash pellets, and coalesced ash pellets zones (including coated clasts).

1. Accretionary lapilli (*AL*)

   Accretionary lapilli are characterized by spherical to sub-spherical forms with conspicuous concentric laminations of fine to coarse ash. Three sub-types are discernible based on contrasts in their detailed internal textures.

   Accretionary lapilli type 1 (*AL-1*) contains a core of altered, unstructured, relatively coarse white ash material enveloped by a laminated brown ash layer forming a mantle over the inner core (Fig. 4.2a and 4.2d). This mantle is rimmed by a fully to partially developed outer layer or coating of fine white ash material with low porosity. The white material in the core commonly consists of altered /weathered clasts. This aggregate type occurs mostly in a relatively big size ranging from 2 to 5 mm in diameter.

   Accretionary lapilli type 2 (*AL-2*) exhibits similar texture features, with an unstructured white altered core and surrounding brown laminated ash mantle (Fig. 4.2g). However, *AL-2* lacks a pronounced white outer rim, showing an extension brown laminated ash mantle. *AL-2* is typically 1.5 to 2.5 mm in diameter.

Accretionary lapilli type 3 (*AL-3*) possess a brown laminated core and mantle akin to the mantle of *AL-1* and *AL-2* but are coated by a relatively thin white outer layer rather than a well-defined rim (Fig. 4.2e and 4.2f). *AL-3* has diameters spanning 1.5 to 3.5 mm.

2. Ash pellets (*AP*)

   Ash pellet occurs as roughly spherical to ellipsoidal forms lacking internal concentric laminations (Fig. 4.2c). Two distinct varieties are present based on their color and clast components: brown ash pellets (*AP-b*) and white ash pellets (*AP-w*). *AP-b* consists predominantly of fresh, unaltered material, while *AP-w* contains more abundant altered ash clasts analogous to the white cores of *AL-1* and *AL-2*. Ash pellets range from 1 to 2.5 mm in diameter.

3. Coalesced/cored pellets (*CP*)

   Zones of coalesced ash pellets are also identified, comprising either brown (*CP-b*; Fig. 4.2h) or white (*CP-b*; Fig. 4.2b) ash pellets adhered to a single or cluster of clasts. Like other aggregate types, the white coalesced ash pellets (*CP-w*) are enriched in altered clasts compared to the fresher brown varieties (*CP-b*). Individually coated clasts range to 2.5 mm, while the coalesced zones extend to 6 mm.

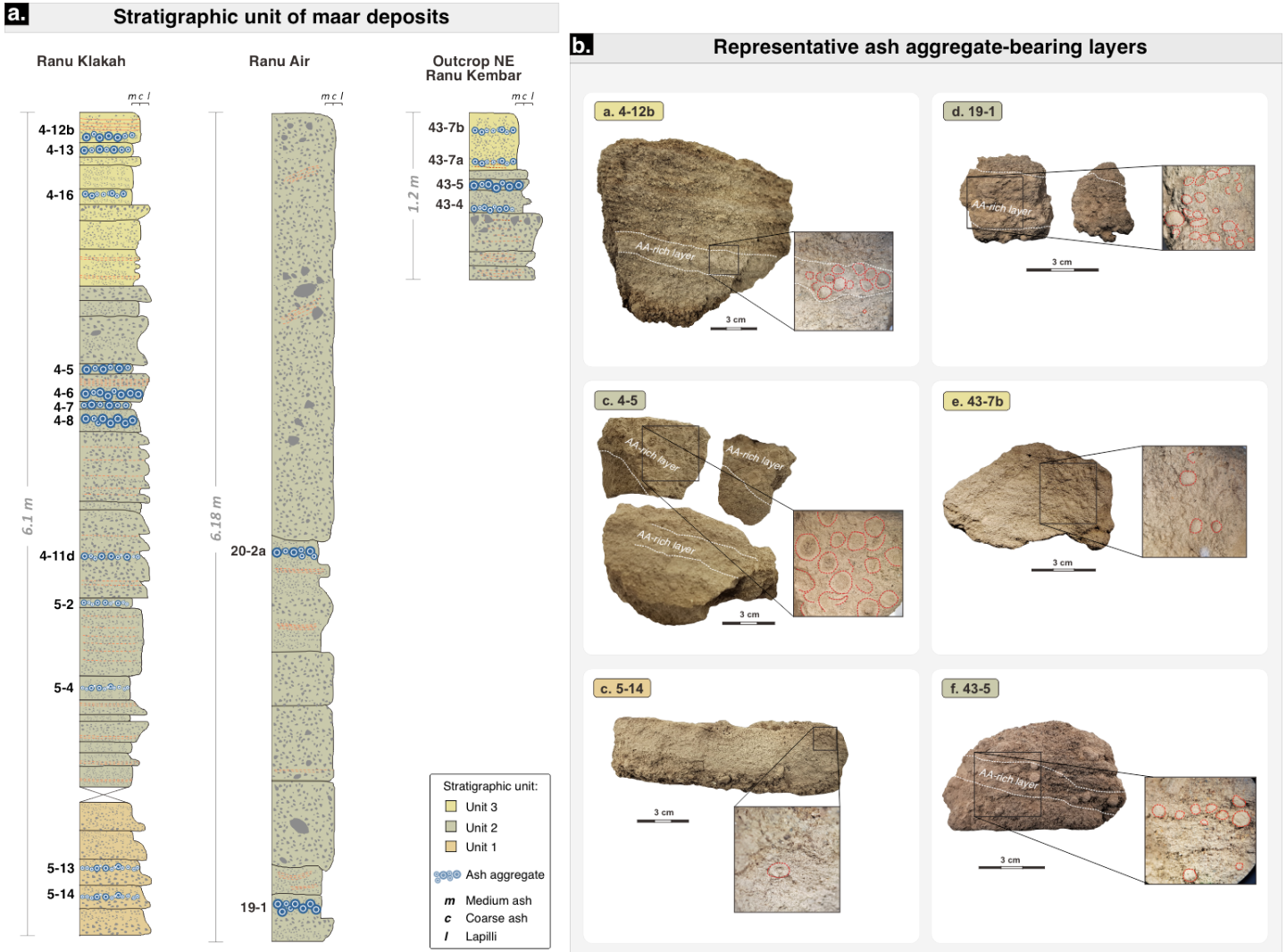

Figure 4. 1. Detailed stratigraphic logs (**a**) through the ash aggregate-bearing pyroclastic layers (**b**) of the proximal maars in LVF maar complex. The series subdivided into three stratigraphic tephra units. The Ranu Klakah maar shows the most complete stratigraphic units (Units 1, 2, and 3), while Ranu Air only consists of unit 2 and Outcrop NE of Ranu Kembar maar consist of units 2 and 3. The tephra layers used in this study are only the ash-aggregate bearing layers.

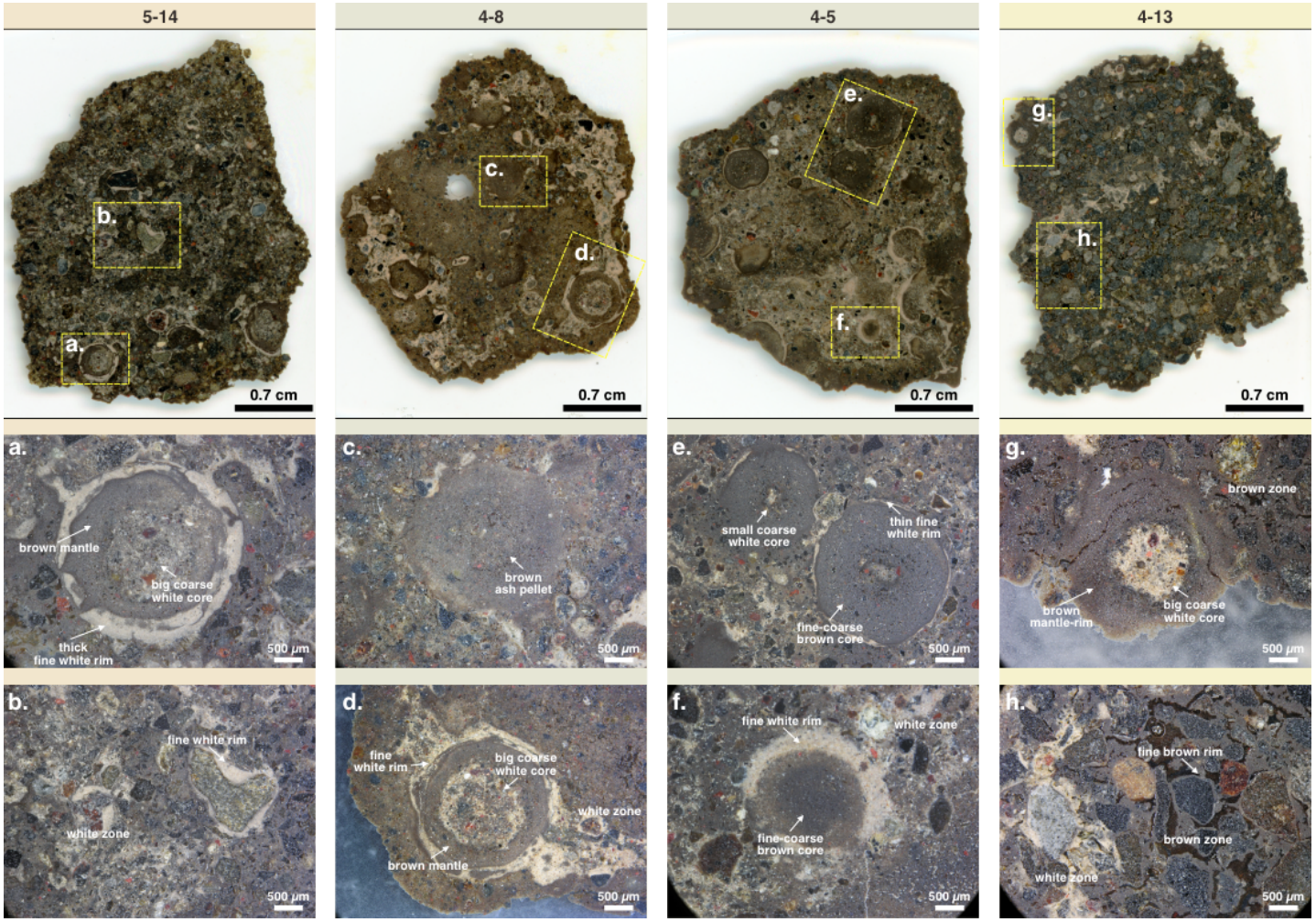

Figure 4. 2. Examples of impregnated polish thin sections of tephra layer samples (upper images). (**a-h**) Closeup images of ash aggregate cross-sections. (**a, d**) Accretionary lapillus with relatively big coarse white core, brown mantle, and thick fine white rim. (**b**) Clasts coated by fine white material, (**c**) brown ash pellets that has no rim, (**e**) Accretionary lapillus similar to a and b with smaller coarse white core and thinner fine white rim, (**f**) Fine-coarse brown ash pellets as a core and coated by relatively thick sine white rim, (**g**) A big coarse white ash pellet as a core coated by moderately developed concentric brown mantle-rim, and (**h**) Clasts coated by fine brown material.

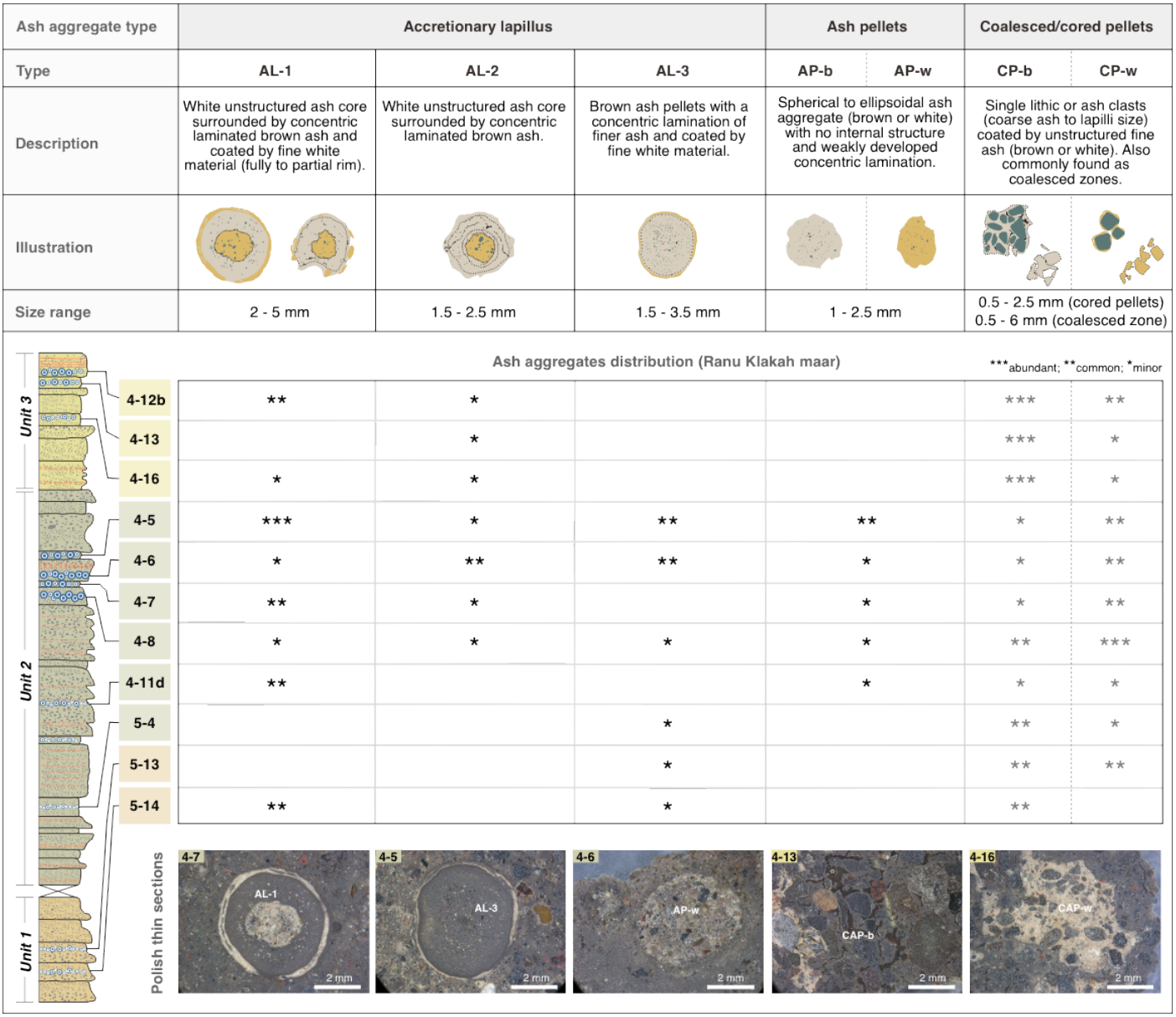

Figure 4. 3. Categories of ash aggregate types identified in the Ranu Klakah maar, with descriptions, typical range of diameters, ash aggregates distribution within stratigraphic units, and representative polish thin section images of ash aggregates.

4.3.3. Ash components and morphology

Quantitative analysis characterized the ash components and morphology (shape) within the aggregate-bearing layers at Ranu Klakah maar, which preserves deposits from all three stratigraphic units.

The componentry analysis involved point counting of over 2000 grains per sample, categorized into juvenile and non-juvenile clast types. The juvenile clasts are black non-vesicular (*bnv*), black vesicular (*bv*), clear-brown (*cb*), pale-brown (*pb*), and orange-brown (*ob*). Non-juvenile clasts are ash aggregates (*aa*), free crystals (*fc*), and altered/weathered clasts (*alt*). Overall, across all samples (Fig. 4.4a), the most abundant juvenile clast types based on average proportions are pale-brown ash (*pb*) at 27.2% (ranging from 13.5% to 41.8%), black non-vesicular (*bnv*) at 24.4% (11.7% to 37.7%), and black vesicular (*bv*) at 3.1% (0.6% to 8.8%). Additional juvenile components present in lower modal abundances include orange-brown (*ob*), averaging 2.2% (1.2% to 3.1%), and clear-brown (*cb*) at 2.2% (0.9% to 3.7%). The non-juvenile fractions are dominated by ash aggregates (*aa*) averaging 32.5% (12.5% to 57.2%), with lesser free crystals (*fc*) at 5.5% (3.9% to 6.7%) and altered lithic clasts (*alt*) comprising 3.0% on average (1.2% to 5.0%).

However, distinct stratigraphic variations exist in the relative proportions of these clast types. In Unit 1, higher average abundances occur of *bnv* (34.1%) and *pb* (31.0%), with subordinate *bv* (2.4%) and *ob* (1.56%), alongside minimum *alt* (1.4%). Comparatively, Unit 2 exhibits decreased average *bnv* (16.0%) and *pb* (24.5%) but slightly increased *cb* (2.3%), *ob* (2.4%), *fc* (5.4%), and *alt* (3.6%). Most notably, *aa* clasts significantly spike in Unit 2 to 43.46% on average. An anomalous sample, layer 4-6, shows an unusually elevated *pb* content of 39.8%. Finally, Unit 3 presents a return to elevated average *bnv* (34.7%) and *pb* (30.1%), alongside increased *bv* (4.8%) and *fc* (6.21%), alongside a notable reduction in *aa* (17.1%) and *alt* (2.6%). These quantified variations in clast populations between stratigraphic units reflect

fluctuations in the relative proportions of juvenile to non-juvenile components. Specifically, Unit 2 exhibits the lowest ratio of juvenile to non-juvenile clasts based on the elevated ash aggregate content, indicating distinct eruption dynamics compared to Units 1 and 3.

Morphometric analysis was conducted on 3425 juvenile ash particles ranging from 125-250 μm in size. Quantitative shape parameters, including convexity, solidity, and form factor (Liu et al., 2015), were obtained for ash particles from representative layers (Fig. 4.4b). Across all units, the samples have median values of form factor ranging from 0.67 to 0.72, convexity spans from 0.95 to 0.97, and solidity spans from 0.94 to 0.95. However, some variations between units are discernible. Ash particles from Unit 1 exhibit high median values of form factor (average 0.72), convexity (average 0.97), and solidity (average 0.95), indicating they are the least irregular particles. By contrast, Unit 2 displays a broader range of shape parameter values, with samples possessing relatively low median values of form factor (average 0.68), convexity (average 0.96), and solidity (average 0.94). Unit 3 particles show nearly similar median values with Unit 1 but slightly lower in form factor (average 0.70). While Unit 2 broadly displays more irregular shapes than other units, one sample – layer 4-6 – exhibits a distinct wide range of shape parameter values. This layer has the lowest median form factor (0.67), convexity (0.95), and solidity (0.94) of any Unit 2 sample, indicating particularly the occurrence of angular and irregular particles.

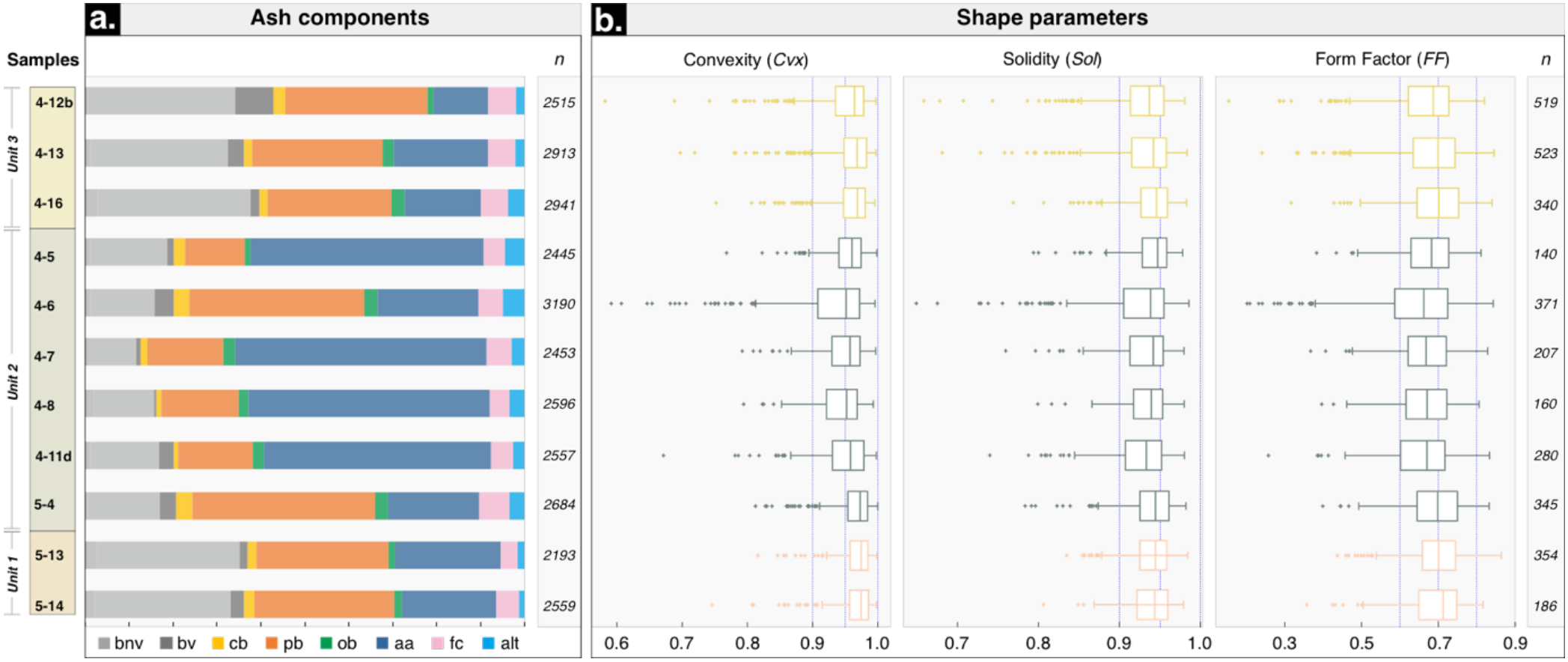

Figure 4. 4. (**a**) Ash component distribution of ash aggregate-bearing tephra layers at Ranu Klakah maar. (**b**) Representative shape parameters for each layer, in terms of convexity, solidity and form factor. All juvenile components (*bnv*, *bv*, *cb*, *pb*, and *ob* ash) were used for the shape measurements. Vertical line within the boxes represents the median of each dataset.

4.3.4. Internal characteristics of ash aggregates

Detailed observation of ash aggregates reveals complexity in the internal texture zonation of the ash aggregates. BSE images indicate distinct domains, including cores, mantles, and outer rims.

White cores comprise unstructured assemblages of coarse fragments ranging from 50-100 μm in diameter (Fig. 4.5a and 4.5d). Individual fragments display angular and blocky morphologies packed with fresh juvenile, altered material, and crystals (e.g. plagioclase, pyroxene, Fe-Ti oxide). Fine materials commonly adhere to the edges of altered particles in the white cores. **White rims** represent the finest-grained component, composed of cemented fragments typically less than 20 μm in diameter (Fig. 4.5a, 4.5e, and 4.5h). The rims exhibit low porosity and variable gradation contacts with inner regions (mantle), ranging from sharp boundaries to gradational zones up to 150 μm wide.

Brown cores contain structureless, mostly juvenile material and crystals up to 60 μm in size, with abundant pores between fragments (Fig. 4.5e). **Brown mantles** display weakly concentric lamination of fragments <30 μm in size (Fig. 4.5a and 4.5e). They possess high porosity with the void between the laminated fragments. **Brown rims** are texturally continuous with the brown mantles, comprising smaller fragments in concentric and unconsolidated zones up to 100 μm thick (Fig. 4.5i). They exhibit higher porosity than the dense white rims, lacking the fine adhered particles in the white rims.

The morphometric analysis quantified the dimensional parameters of internal components of different ash aggregate types (Fig. 4.6). As shown in Figure 4.6a, the ash pellets (AP) and coalesced/cored pellets (*CP*) types exhibit relatively thin rim zones, most under 0.3 mm. In comparison, the *AL* type possesses more developed rim zones up to 0.5 mm.

Additionally, detailed measurements indicate textural variations in the dimensional sizes of AL and AP across representative stratigraphic layers (Fig. 4.6c). In unit 1, the

aggregates have a median diameter of around 2.5 mm, with relatively small median core dimensions of around 1.3 mm, thin mantles (0.3 mm), and rims (2 mm). In unit 2, the median size of aggregates is broader from 1.5 to 3.3 mm, with wider median core sizes (0.5-2 mm), thicker mantles (0.3-0.5 mm), and rims (0.25-0.32 mm). In Unit 2, layer 4-6 notably display the smallest median core (~0.7 mm) and mantle (~0.3 mm) dimensions. Finally, in Unit 3, the median diameter is ~2.6 mm, relatively similar to Unit 1, but with a larger median core size (~1.7 mm), thicker mantles (~0.5 mm), and rims (~0.25 mm). These quantitative data indicate that Unit 2, in particular, exhibits distinctively thick rim development.

4.3.5. Ash aggregate compositions

Bulk mineralogy analysis by X-ray diffraction (XRD) reveals that the predominant crystalline phases within the accretionary lapilli comprise common silicate minerals, including plagioclase feldspar, clinopyroxene, and magnetite (Fig. 4.7a). The presence of these peaks indicates the abundance of unaltered igneous mineral clasts within the aggregates. However, detecting vermiculite clay diffraction patterns indicates alteration of primary mafic minerals. Supplementary SEM-EDS spectra (Fig. 4.8a-c) confirm vermiculite compositions (Mg-Ca-Fe-Si-Al) concentrated within white core and rim regions, binding cement between larger grains. Additionally, SEM-EDS elemental mapping illustrates intricate chemical zoning in chlorine (Cl) across the accretionary lapilli (Fig. 4.9). Elevated chlorine contents within brown inner mantle domains relative to white outer rims and cores reflect gradational volatile zonation.

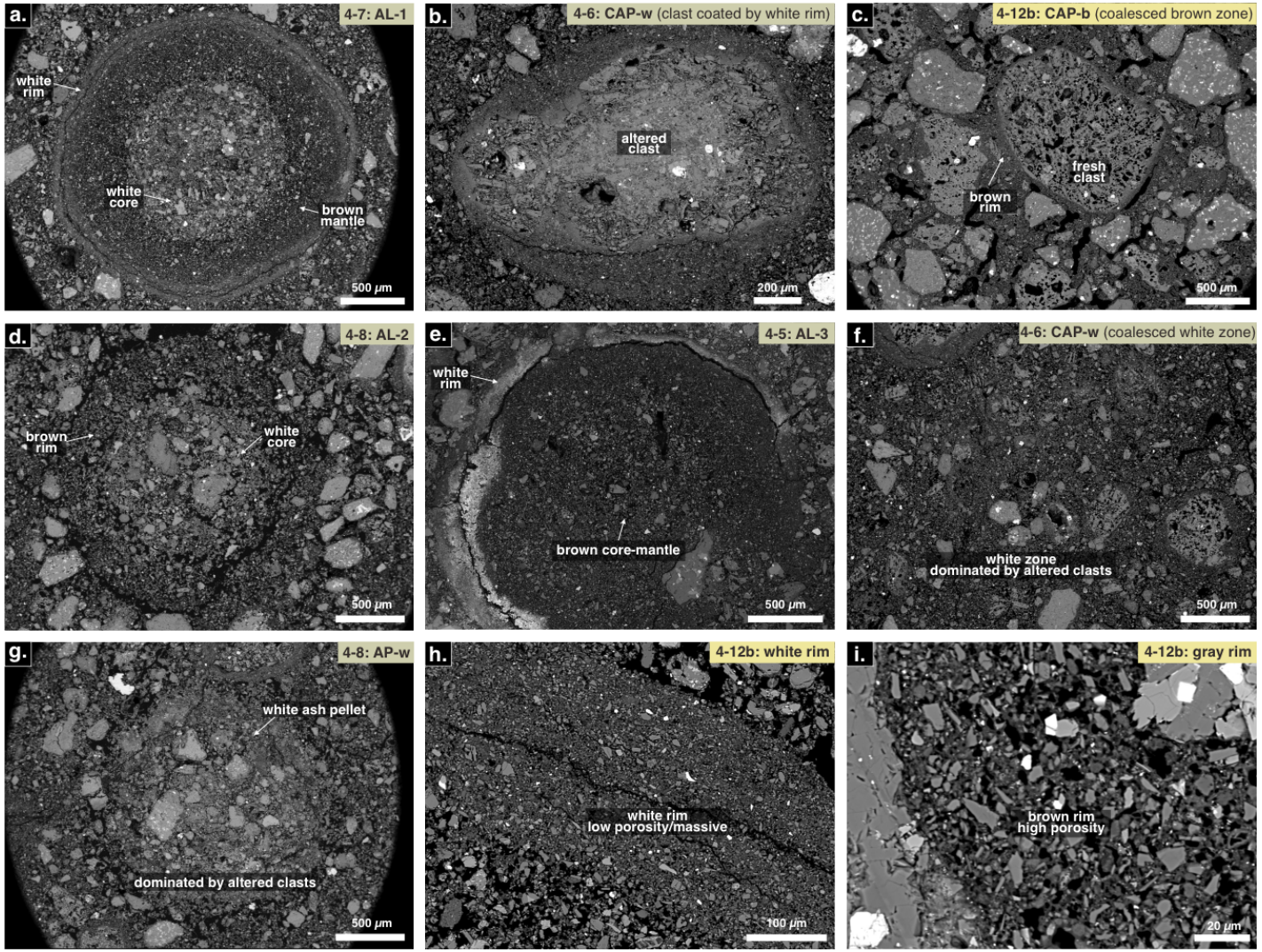

Figure 4. 5. SEM-BSE images of internal textures of ash aggregates: (**a**) typical of accretionary lapilli type I, (**b**) altered clast coated by fine white material, (**c**) coalesced brown zone which ash clasts are coated by fine brown material, (**d**) coarse altered white core coated by finer brown material, (**e**) brown core-mantle with white rim, (**f**) coalesced white zone which ash clasts are relatively altered and coated by fine white material, (**g**) coarse white ash pellet dominated by altered material, (**h**) fine white rim with low porosity and massive structure, and (**i**) brown rim with high porosity.

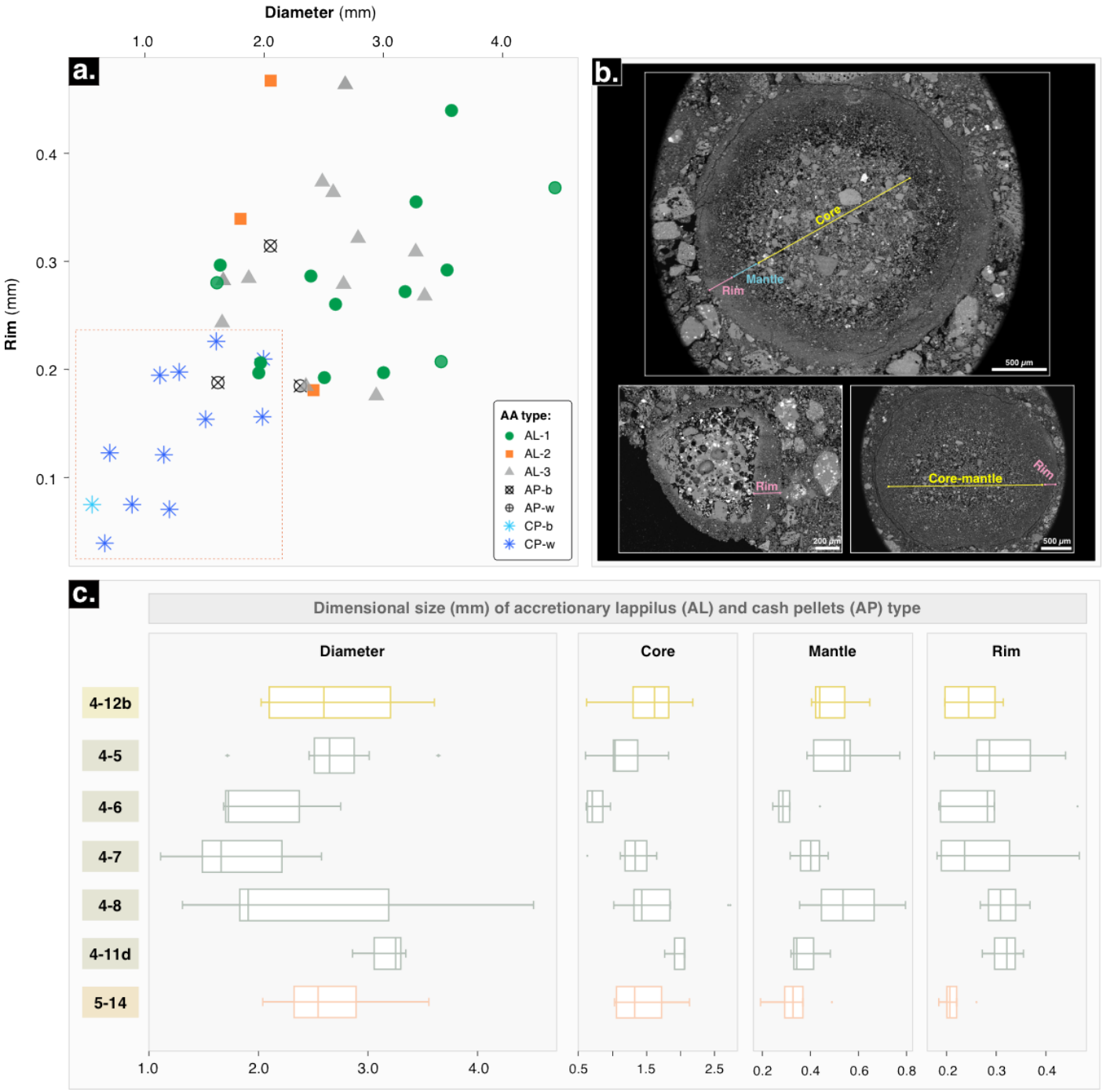

Figure 4. 6. Compiled morphological data from 54 aggregates from Ranu Klakah maar, shown with respect to (**a**) whole-aggregate diameter vs rim, (**b**) example of dimensional measurements, (**c**) detailed dimensional size of accretionary lapillus (AL) and ash pellets (AP) type.

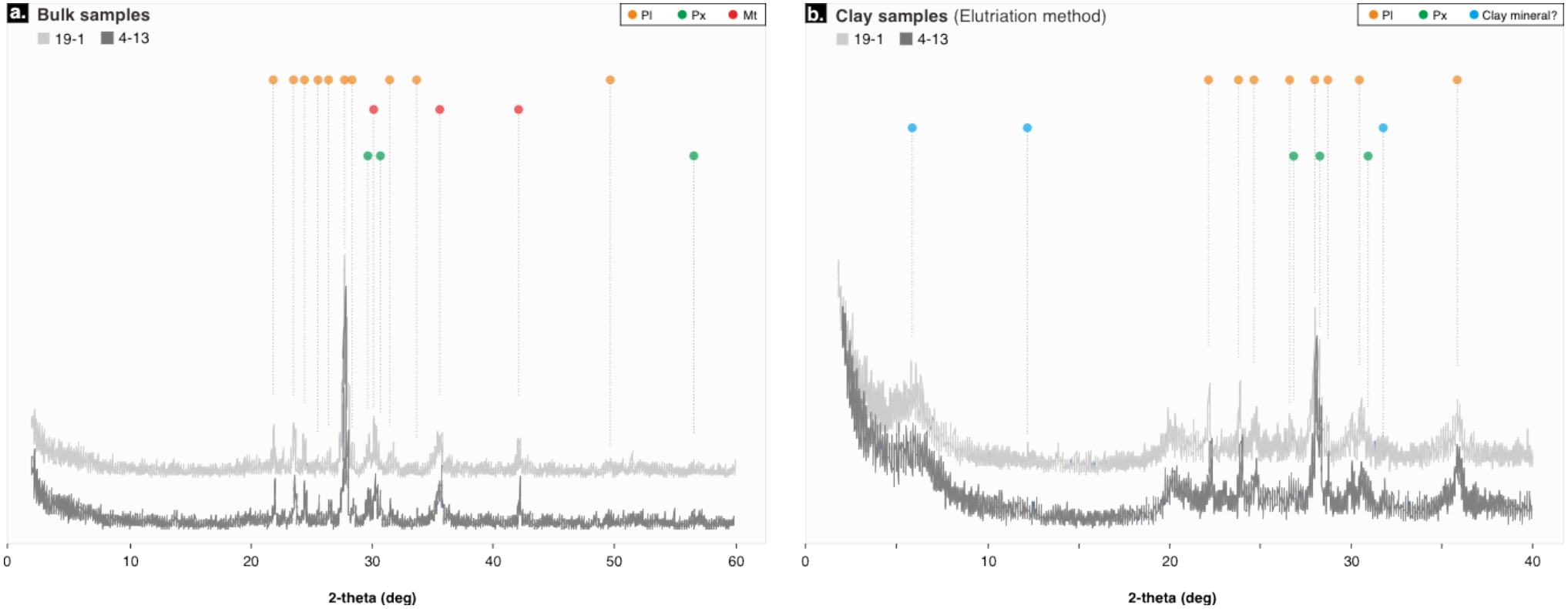

Figure 4. 7. Representative X-ray diffraction (XRD) patterns of the accretionary lapilli (**a**= bulk powder samples, **b**= clay samples) collected from Ranu Klakah (4-13) and Ranu Air (19-1). Circle points above the curves are the diffraction peaks. The colors are attributed to each phase as: orange= plagioclase (Pl), green= pyroxene (Px), red= magnetite (Mt), and blue= Clay mineral.

4.4. DISCUSSION

4.4.1. Stratigraphic variations and eruption style transitions

Detailed stratigraphic identification in the deposits on the Ranu Klakah, Ranu Air, and NE Ranu Kembar outcrops reveals a sequence of three tephra units that represent their eruptive activity over time (Fig. 4.1). At Ranu Klakah, maar deposits show complete vertical variations of stratigraphy units (Fig. 4.1), ash components (Fig. 4.4a), and ash morphology (Fig. 4.4b). These variations may provide evidence for typical evolving eruption styles during the maar-forming sequence in the LVF.

Unit 1 deposits represent the earlier eruption activity, mostly composed of lapilli with large-sized lithics and relatively high in juvenile clasts. Wohletz and Sheridan (1983) observed that lapilli-rich deposits typically represent initial maar eruptions driven primarily by magma influx. This unit includes minimal aggregation products, as evidenced by the low occurrence of ash aggregates (*aa*) particles, consistent with the lower relative intensity of magma-water interaction interpreted from assemblages in Ranu Air and Ranu Kembar deposits. On the other side, the elevated abundance of *aa* clasts in Unit 2 (average 43.5%), compared to the lower occurrence in Units 1 and 3 (17.1-32.5%), implies a relatively wet, water-dominated condition on phreatomagmatic activities (Van Eaton & Wilson, 2013; Schmith & Swanson, 2023). It is consistent with the association of aggregate-rich layers in Unit 2 (Fig. 4.1, 4.3, and 4.4a) and accompanied by the low abundance of juvenile components (Fig. 4.4a). Notably, the significant increase of juvenile components and decreasing *aa* clasts on layer 4-6 of Unit 2 may indicate changes in increasing magma influx or decreasing water availability. Further, Unit 3, the latter eruption activity product, shows a similar drier phreatomagmatic activity as Unit 1 produced component distribution with high juvenile rather than non-juvenile clasts. Overall, the identification through stratigraphic units indicates a signature of transition between drier (Unit 1 and 3) and wetter (Unit 2) phreatomagmatic activities during Ranu Klakah maar eruptions.

The ash morphology of juvenile particles, performed on the 125-250 μm size fraction (Fig. 4.4b) from each ash aggregate-bearing layer in stratigraphic units at Ranu Klakah maar provides insight into its eruption dynamics. As the phreatomagmatic products, particles from examined layers show high median values of convexity (*Cvx*), solidity (*Sol*), form factor (*FF*), and axial ratio (*AR*) at > 0.95, > 0.93, > 0.67, and > 0.68, respectively, reflecting the presence of fine-grained, blocky, and round particles associated with brittle fragmentation (e.g. Maria & Carey, 2002; Liu et al., 2015; Nurfiani & de Maisonneuve, 2018; Thivet et al., 2020a; 2020b). Despite the similarity in measured shape parameters, juvenile particles in Unit 2 show small differences in more irregular morphology with slightly lower median values of *Cvx* (average 0.95) and *Sld* (average 0.94), suggesting a change in fragmentation conditions. In this case, the phreatomagmatic eruptions producing more irregular ash shapes may have been attributed to increasing water/magma ratios compared to lower water scenarios. Combined with the elevated ash aggregates and lower juvenile clast in Unit 2, this implies a transition to relatively higher water/magma ratios, driving more intensive wet phreatomagmatism (Wohletz et al., 2012). This condition also elevates vapor and condensed water fractions on eruption plumes, which are efficient for ash aggregate formation (Van Eaton & Wilson, 2013; Schmith & Swanson, 2023).

4.4.2. Origins and significance of white and brown materials in ash aggregates

Observation of textural variations within ash aggregates from Ranu Klakah maar deposits reveals the presence of two compositionally distinct domains: altered white materials and unaltered brown materials forming cores, mantles, and rims. Detailed SEM imagery shows that the white domains contain altered ash and clay minerals, whereas the brown domains are dominated by fresh glass and crystal. Distinguishing between hydrothermally modified versus primary juvenile components preserved in ash aggregates provides insights into eruption

dynamics, such as the relative contributions of recycled material versus newly fragmented magma. Quantifying and characterizing the petrologic differences between these domains enhance the interpretation of changing eruption conditions.

White domains in the cores and rims of accretionary lapilli and structureless domains in ash pellets contain abundantly altered minerals, indicating hydrothermal modification (Fig. 4.2a, d, f, g; Fig. 4.5a, b, d, g, h). SEM-EDS analysis of these white materials detects the presence of clay minerals and partially altered ash clasts. XRD spectra of accretionary lapilli also indicate the occurrence of most likely vermiculite clay minerals. This clay mineral and altered ash suggest their origin from recycled crater materials and/or wall rocks in the subsurface conduit system that were hydrothermally modified prior to the excavation event (e.g. D'Oriano et al., 2011; 2014; Thivet et al., 2020b). Vent-clearing explosions remobilized these altered materials from the subsurface, incorporating the clay-rich clasts into eruption columns. Their subsequent accretion is recorded by preserving aggregates deposited during eruption intervals (Mueller et al., 2016; 2017).

In contrast, brown mantle domains of accretionary lapilli and brown rims of ash pellets or coated ash particles contain predominantly fresh, unaltered juvenile clasts, including glass shards and mineral phenocryst fragments lacking clay minerals. These fractions textures resemble the typical products of magma fragmentation (Ross et al., 2022). The lack of clay minerals indicates derivation directly from magma, as eruptions were driven by magma intersecting external water. The concentric growth of brown mantles and rims around cores (Fig. 4. 2c and 4. 2g) records accretion within the turbulent, wet plumes above the vent (Schumacher & Schmincke, 1995).

Distinct white altered clast-rich and brown fresh juvenile-rich aggregate components provide textural evidence of two different material cycling processes during maar eruptions (Schumacher & Schmincke, 1995; D'Oriano et al., 2014). Firstly, excavation and incorporation

of older altered products into eruption columns through vent-clearing explosions. Secondly, ongoing aggregation of newly fragmented magma occurs above the vent. These capture the complex, cyclic nature of maar eruption dynamics driven by fluctuating magma-water conditions (Wohletz & Sheridan, 1983). Variations in the relative proportions of brown versus white aggregates between stratigraphic units suggest oscillating contributions from direct magma fragmentation versus recycling of wall rocks and/or crater materials (Fig. 4.4).

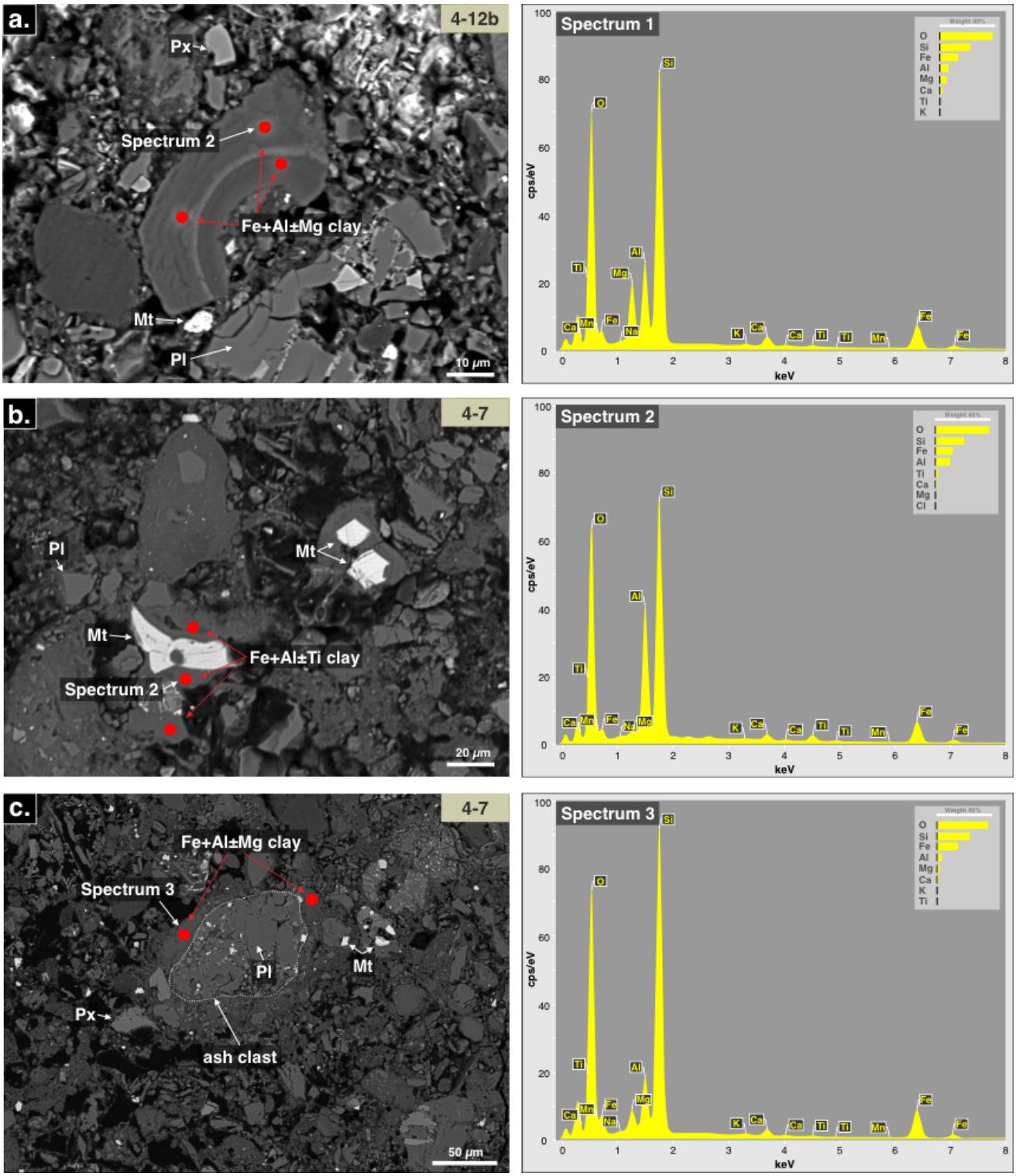

Figure 4. 8. In the left part of the figure, BSE images collected from white part of ash aggregates which displayed the occurrence of clay (Fe+Al±Mg±Ti) minerals. In the right part of the figure, SEM-EDS spectrum points indicate vermiculite mineral compositions. The abbreviations on the BSE images mean: Px= pyroxene, Pl= plagioclase, and Mt= magnetite.

4.4.3. Formation of ash aggregates and its implication on Ranu Klakah maar eruptions

In phreatomagmatic eruptions, vigorous steam production from magma-water interaction results in relatively cool, moist eruption surge clouds. In these conditions, liquid water films can condense on ash grains, causing them to stick together through liquid bonding rather than disperse (Schumacher & Schmincke, 1995). Aggregates larger than 1 mm are more likely generated by these liquid bonding forces than electrostatic forces, which typically only produce diameters under tens of micrometers (James et al., 2002; Mueller et al., 2018). The subsequent cementation process may then help in establishing strong interparticle bridges to preserve aggregates within the eruption process (e.g. Mueller et al., 2016). These mechanisms involving moisture-induced grain aggregation and cementation most likely explain the formation of the observed ash aggregate assemblages at the LVF maar complex.

Ash aggregates from Ranu Klakah maar exhibit three distinct groups: accretionary lapilli (*AL*), ash pellets (*AP*), and coalesced/cored pellets (*CP*). They are similar to the descriptions of aggregate types in many previous studies as *AP2*, *AP1*, and *CP*, respectively (e.g. Brown et al., 2010; Van Eaton & Wilson, 2013; Mueller et al., 2016; 2017; 2018). Spherical accretionary lapilli (*AL/AP2*) with well-developed lamination structures of fine-grained particles around the unstructured ash core indicate significant external water interaction. It generates wet, turbulent eruption plumes, enabling efficient moisture condensation and continuous ash aggregation (Schumacher & Schmincke, 1995; Brown et al., 2011; Van Eaton et al., 2012; Van Eaton & Wilson, 2013; Mueller et al., 2018). Moreover, the variation in *AL* textures signifies differences in plume conditions (i.e. residence time, eruptive intensity, locations on the ash plume, and water availability) influencing aggregate growth (Schumacher & Schmincke, 1995; Brown et al., 2010; 2012; Burns et al., 2017). *AL-1* with thicker mantles and rims represents continuous accretionary growth under sustained, powerful blasts within highly turbulent plumes (Mueller et al., 2018). The growth is also favored by

varying transport between eruption plumes and turbulent ash and pyroclastic flows. In contrast, *AL-2* and *AL3* with thinner, incomplete rims and mantles suggest periodic weaker plume interactions insufficient to fully develop rims before deposition (e.g. Van Eaton & Wilson, 2013; Mueller et al., 2016; Burns et al., 2012). However, ash pellets (*AP/AP1*) represent incomplete *AL* aggregates with no internal structure and weakly developed concentric lamination. This type was likely deposited on eruption plumes during a short residence time before the fine-grained concentric rim was fully established (e.g. Van Eaton et al., 2012; Mueller et al., 2016).

The ability of *AL* aggregates to survive during eruption processes likely requires strong interparticle connections. The increasing amount of salt (NaCl) loads acts as the binding agent, promoting the stability of ash aggregate preservation (Mueller et al., 2016). A key observation of the presence of white domains is that they are enriched in clay minerals and hydrothermally altered clasts throughout ash aggregates, as shown in BSE images (e.g. Fig. 4. 5b and 4.8a-c). The alteration of ash clasts is implicated as a source of cement-like material that establishes strong interparticle connections. The white materials were possibly formed through low-temperature alteration coating these clasts, which were excavated into eruption columns and incorporated into white cores and zones. Furthermore, the formation of laminated white rims remains intricate. Possibilities include (1) the hydrothermally altered area of particles reacting with condensed water during wet eruption conditions and/or (2) the mixture of water and clay minerals liberating the eruption plumes and adhering to the fine-grained particles (Schumacher & Schmincke, 1995). Either could form liquid bonding layers, stick adjacent fine-grained juvenile fractions, and altered clasts. It is attaching them through a process analogous to curing concrete by hydrating cement compounds. Other possibilities include similar rapid alteration of particle surfaces in contact with water, producing amorphous silica coatings (Van Eaton et al., 2012; Mueller et al., 2017), potentially implicated by XRD results (Fig. 4.7).

Ash aggregates identified in Ranu Klakah maar deposits provide insights into the formation process during variable maar eruptions (Fig. 4.3). Unit 2 contains the highest proportion of most ash aggregate types and is dominated by accretionary lapilli (*AL*) (Fig. 4.3). This indicates increased aggregation efficiency during the Unit 2 eruption phase, driven by extended wet phreatomagmatic eruptions, enabling moisture condensation and ash aggregation in eruption plumes (e.g. Schumacher and Schmincke, 1995; Burns et al., 2017). This unit exhibits a prevalence of well-developed laminated mantles and abundantly fine white outer rims. Schumacher and Schmincke (1995) showed that such textures reflect moderate water availability (between 15 and 25 wt.%), allowing repeated accretion and densification of fine ash into core particles. Thicker rims of *AL* and *AP* in Unit 2 (median: 0.25-0.32 mm) compared to Units 1 and 3 (median: 0.20-0.25 mm) may also indicate more sustained low-energy ash recycling above the vent (Burns et al., 2017; Morgavi et al., 2019). Hence, eruptions in Unit 2 promoted accretionary lapilli growth through continuous aggregation. However, abundant ash pellets and coated clasts in Units 1 and 3 indicate intermittent shifts into drier regimes unfavorable for vapor condensation and aggregation (e.g. Mueller et al., 2016).

The accretionary lapilli characteristics of the Ranu Klakah maar deposits reflect a complex, time-transgressive evolution of the eruptions. They progressed from initial drier phreatomagmatic phases to a peak of intensive water-influenced (with less magmatic influx) explosive activity and then again to the drier phase as the water reservoir was depleted.

4.4.4. Ash aggregates composition and post-eruptive alteration

The XRD and SEM-EDS techniques analyzed the composition of ash aggregates (intact accretionary lapilli) from Ranu Klakah and Ranu Air maars. The results found compositions of silicate minerals, including plagioclase, pyroxene, and magnetite (Fig. 4.7 and 4.8). These minerals are interpreted as fragmented juvenile fractions. Moreover, these mineral assemblages

most likely represent mafic to intermediate volcanic composition, which aligns with previous geochemical studies in LVF by Carn and Pyle (2000) and presents geochemical data in Chapter 3 in Figures 3.3 and 3.4.

Clay mineral compositions (Fe+Al±Mg±Ti) were identified in ash aggregates from Ranu Klakah and Ranu Air maar (Fig. 4.7b and 4.8). It indicates that post-eruption alteration activities occurred. The clay compositions were mostly found in the white cores and occasionally in the white rim regions of the ash aggregates, as confirmed by EDS spectra (Fig. 4.8a–c). In this context, these clay minerals could have served as a binding cement between grains (Fig. 4.8b–c) or as a coating material on the exterior of altered clasts (Fig. 4.5b and 4.8c). Our identification of this alteration product provides valuable insight into the subsequent evolution of the volcanic system during typical short-term maar eruptions.

Elemental mapping of the accretionary lapilli shows a relatively increasing chlorine concentration within the brown domains compared to the white outer rims and cores (Fig. 4.9a–c). The presence of chlorine can indicate the transport and deposition of volcanic aerosols and the involvement of magmatic fluids rich in volatile components (Yaguchi et al., 2015; 2019). Studies by Nogami et al. (2001) and Yaguchi et al. (2015; 2019) found chlorine is a water-soluble component derived from magmatic volatiles that adhere to volcanic ash particles. Yaguchi et al. (2015; 2019) also found that elevated chlorine concentrations, along with other water-soluble components, are associated with eruptions influenced by liquid-volatile-rich conditions (e.g. Kusatsu-Shirane and Asama volcanoes, Japan). It suggests the observed variation in chlorine distribution pattern within accretionary lapilli from the Ranu Klakah and Ranu Air maars reflects evidence of multiple alteration stages. This pattern indicates that volatile-rich magmatic fluids may have influenced the primary fragmented magma of brown materials more strongly than the altered white materials. Moreover, the lower chlorine in the

white materials could result from leaching during recycling and post-eruption alteration processes.

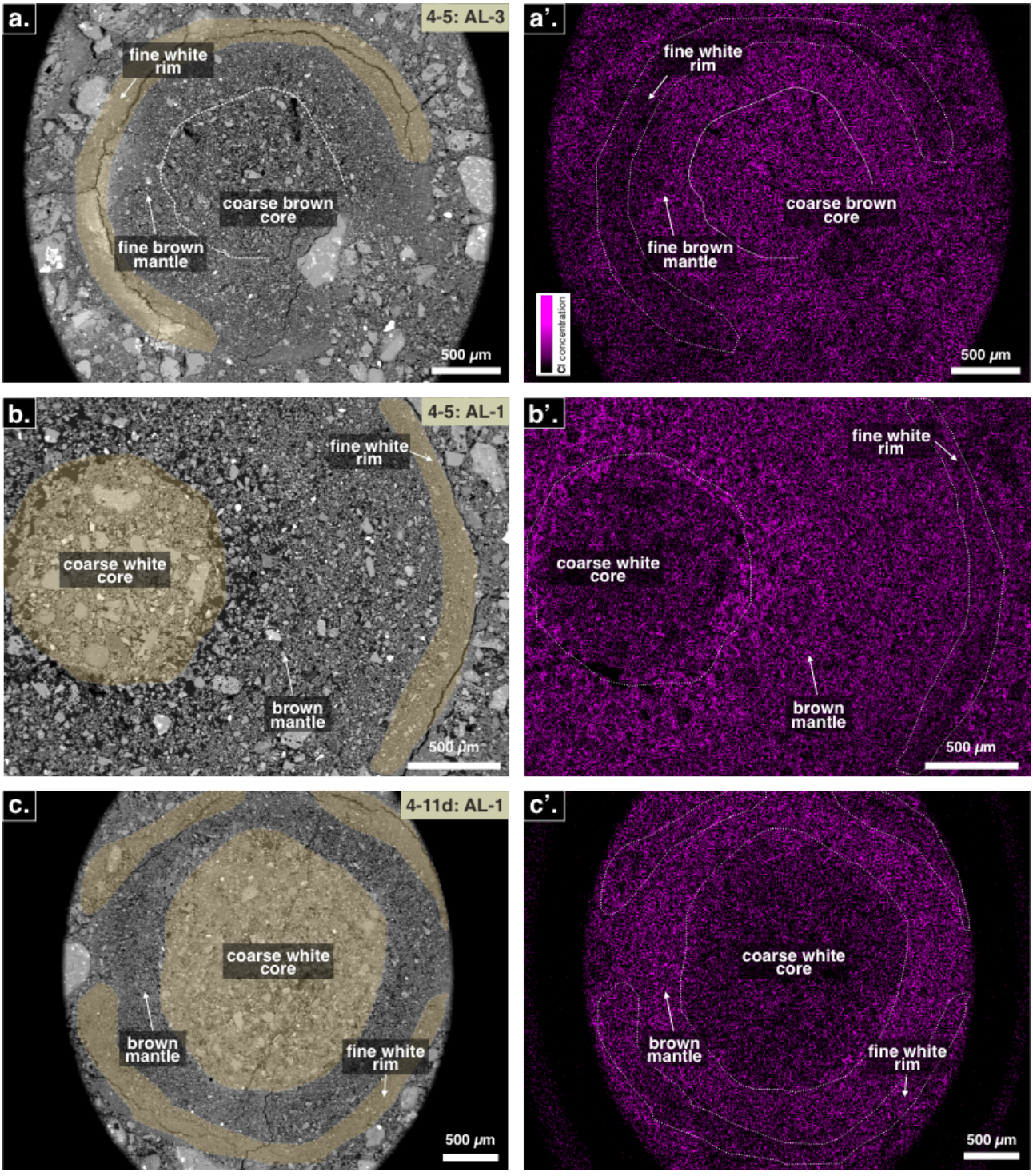

Figure 4. 9. In the left part of the figure are the representative sample of accretionary lapillus that show the occurrence of white and brown material. In the right part of the figure are represented the elemental chemical mapping of chlorine (Cl) related to the SEM-BSE images.

4.5. CONCLUSION

1. This integrated study aimed to elucidate the evolving eruptive dynamics at Ranu Klakah maar by characterizing the attributes of ash aggregates preserved in distinct stratigraphic units. Detailed logging and quantification of compositional variations between Units 1-3 enabled the reconstructing of shifting eruption styles over the deposit sequence.
2. Unit 1 exhibited an abundance of juvenile components, indicating phreatomagmatic activity driven primarily by magmatic influx. In contrast, Unit 2 featured elevated ash aggregate abundances with decreased juvenile contents, attributable to intensive wet conditions conducive to aggregation processes. Subsequent Unit 3 suggested waning external water influence, resembling Unit 1 conditions.
3. Component and textural examination identified variable abundances of altered versus juvenile materials, offering insight into concurrent primary fragmentation and recycling through vent-clearing explosions. Examining internal aggregate textures provided a changing structure linked to fluctuating moisture regimes within eruption columns over time. Well-developed mantles and rims within Unit 2 indicated sustained wet conditions ideal for aggregation efficiency.
4. Supplemental mineralogical data identified secondary alteration phases, such as Fe+Al±Mg±Ti clay minerals, illuminating post-eruption system evolution. The clay minerals detected within altered ash domains may have acted as a cement, helping preserve aggregates.
5. These integrated stratigraphic, textural, and geochemical lines of evidence enhanced understanding of the complex, temporally variable maar eruptive dynamics through fingerprinting in preserved ash aggregates. Such findings carry implications for reconstructing transient hazards at analogous monogenetic volcanic fields.

4.6. REFERENCE

Barone, G., Mazzoleni, P., Corsaro, R. A., Costagliola, P., di Benedetto, F., Ciliberto, E., Gimeno, D., Bongiorno, C., & Spinella, C. (2016). Nanoscale surface modification of Mt. Etna volcanic ashes. *Geochimica et Cosmochimica Acta*, *174*, 70–84. https://doi.org/10.1016/j.gca.2015.11.011

Brown, R. J., Bonadonna, C., & Durant, A. J. (2012). A review of volcanic ash aggregation. *Physics and Chemistry of the Earth*, *45–46*, 65–78. https://doi.org/10.1016/j.pce.2011.11.001

Brown, R. J., Branney, M. J., Maher, C., & Dávila-Harris, P. (2010). Origin of accretionary lapilli within ground-hugging density currents: Evidence from pyroclastic couplets on Tenerife. *Bulletin of the Geological Society of America*, *122*(1–2), 305–320. https://doi.org/10.1130/B26449.1

Burns, F. A., Bonadonna, C., Pioli, L., Cole, P. D., & Stinton, A. (2017). Ash aggregation during the 11 February 2010 partial dome collapse of the Soufrière Hills Volcano, Montserrat. *Journal of Volcanology and Geothermal Research*, *335*, 92–112. https://doi.org/10.1016/j.jvolgeores.2017.01.024

Campos, A., Moreno, S., & Molina, R. (2009). Earth sciences research journal characterization of vermiculite by XRD and spectroscopic techniques. In *Earth Sci. Res. J* (Vol. 13, Issue 2: 108-118).

Gislason, S. R., Hassenkam, T., Nedel, S., Bovet, N., Eiriksdottir, E. S., Alfredsson, H. A., Hem, C. P., Balogh, Z. I., Dideriksen, K., Oskarsson, N., Sigfusson, B., Larsen, G., & Stipp, S. L. S. (2011). Characterization of Eyjafjallajökull volcanic ash particles and a protocol for rapid risk assessment. *Proceedings of the National Academy of Sciences of the United States of America*, *108*(18), 7307–7312. https://doi.org/10.1073/pnas.1015053108

James, M. R., Gilbert, J. S., & Lane, S. J. (2002). Experimental investigation of volcanic particle aggregation in the absence of a liquid phase. *Journal of Geophysical Research: Solid Earth*, *107*(B9), ECV 4-1-ECV 4-13. https://doi.org/10.1029/2001jb000950

James, M. R., Lane, S. J., & Gilbert, J. S. (2003). Density, construction, and drag coefficient of electrostatic volcanic ash aggregates. *Journal of Geophysical Research: Solid Earth*, *108*(B9). https://doi.org/10.1029/2002jb002011

Lane, S. J. (1994). *The origin of accretionary lapilli* (Vol. 56). Springer-Verlag.

Morgavi, D., Valentini, L., Porreca, M., Zucchini, A., di Michele, A., Ielpo, M., Costa, A., Rossi, S., Landi, P., & Perugini, D. (2018). Volcanic ash aggregation enhanced by seawater interaction: The case of the Secche Di Lazzaro phreatomagmatic deposit (stromboli). *Annals of Geophysics*, *61*(6). https://doi.org/10.4401/ag-7874

Mueller, S. B., Kueppers, U., Ayris, P. M., Jacob, M., & Dingwell, D. B. (2016). Experimental volcanic ash aggregation: Internal structuring of accretionary lapilli and the role of liquid bonding. *Earth and Planetary Science Letters*, *433*, 232–240. https://doi.org/10.1016/j.epsl.2015.11.007

Mueller, S. B., Ayris, P. M., Wadsworth, F. B., Kueppers, U., Casas, A. S., Delmelle, P., Taddeucci, J., Jacob, M., & DIngwell, D. B. (2017). Ash aggregation enhanced by deposition and redistribution of salt on the surface of volcanic ash in eruption plumes. *Scientific Reports*, *7*. https://doi.org/10.1038/srep45762

Mueller, S. B., Kueppers, U., Huber, M. S., Hess, K. U., Poesges, G., Ruthensteiner, B., & Dingwell, D. B. (2018). Aggregation in particle rich environments: a textural study of examples from volcanic eruptions, meteorite impacts, and fluidized bed processing. *Bulletin of Volcanology*, *80*(4). https://doi.org/10.1007/s00445-018-1207-3

Nakatani, T., Sugaya, S., Yasui, M., Okumura, S., & Nakamura, M. (2021). Amorphous silica coating on flank deposits of the 1783 CE eruption at Asama volcano. *Journal of Volcanology and Geothermal Research*, *411*. https://doi.org/10.1016/j.jvolgeores.2020.107149

Rose, W. I., & Durant, A. J. (2011). Fate of volcanic ash: Aggregation and fallout. *Geology*, *39*(9), 895–896. https://doi.org/10.1130/focus092011.1

Rossi, E., Bagheri, G., Beckett, F., & Bonadonna, C. (2021). The fate of volcanic ash: premature or delayed sedimentation? *Nature Communications*, *12*(1). https://doi.org/10.1038/s41467-021-21568-8

Schmith, J., & Swanson, D. A. (2023). Complex styles of phreatomagmatic explosions at Kīlauea Volcano, Hawaii, controlled by magma structure. *Frontiers in Earth Science*, *11*. https://doi.org/10.3389/feart.2023.1153288

Schumacher, R., & Schmincke, H.-U. (1991). Internal structure and occurrence of accretionary lapilli-a case study at Laacher See Volcano. *Bulletin of Volcanology, 53 (612-634)*.

Schumacher, R., & Schmincke, H.-U. (1995). Models for the origin of accretionary lapilli. *Bulletin of Volcanology, 53 (626-639).*

Scolamacchia, T., & Dingwell, D. B. (2014). Sulfur as a binding agent of aggregates in explosive eruptions. *Bulletin of Volcanology*, *76*(10). https://doi.org/10.1007/s00445-014-0871-1

Surtees, A. P. H., Swindles, G. T., Savov, I. P., Scowen, I. J., Edwards, H. G. M., & Munshi, T. (2016). Raman spectroscopy for the discrimination of tephras from the Hekla eruptions of AD 1510 and 1947. *Holocene*, *26*(3), 432–438. https://doi.org/10.1177/0959683615609744

Telling, J., Dufek, J., & Shaikh, A. (2013). Ash aggregation in explosive volcanic eruptions. *Geophysical Research Letters*, *40*(10), 2355–2360. https://doi.org/10.1002/grl.50376

Thivet, S., Carlier, J., Gurioli, L., di Muro, A., Besson, P., Smietana, M., Boudon, G., Bachèlery, P., Eychenne, J., & Nedelec, J. M. (2022). Magmatic and phreatomagmatic contributions on the ash-dominated basaltic eruptions: Insights from the April and November–December 2005 paroxysmal events at Karthala volcano, Comoros. *Journal of Volcanology and Geothermal Research*, *424*. https://doi.org/10.1016/j.jvolgeores.2022.107500

Thivet, S., Gurioli, L., di Muro, A., Derrien, A., Ferrazzini, V., Gouhier, M., Coppola, D., Galle, B., & Arellano, S. (2020). Evidences of Plug Pressurization Enhancing Magma Fragmentation During the September 2016 Basaltic Eruption at Piton de la Fournaise (La Réunion Island, France). *Geochemistry, Geophysics, Geosystems*, *21*(2). https://doi.org/10.1029/2019GC008611

Tomita, K., Kanai, T., Kobayashi, T., & Oba, N. (1985). Accretionary lapilli formed by the eruption of Sakurajima volcano. *J. Japan, Assoc. Min, Petr. Econ. Geol. 80 (49-54).*

Van Eaton, A. R. (2012). *Dynamics Of Large, Wet Volcanic Clouds: The 25.4 Ka Oruanui Eruption Of Taupo Volcano, New Zealand*.

Van Eaton, A. R., Mastin, L. G., Herzog, M., Schwaiger, H. F., Schneider, D. J., Wallace, K. L., & Clarke, A. B. (2015). Hail formation triggers rapid ash aggregation in volcanic plumes. *Nature Communications*, *6*. https://doi.org/10.1038/ncomms8860

Van Eaton, A. R., Muirhead, J. D., Wilson, C. J. N., & Cimarelli, C. (2012). Growth of volcanic ash aggregates in the presence of liquid water and ice: An experimental approach. *Bulletin of Volcanology*, *74*(9), 1963–1984. https://doi.org/10.1007/s00445-012-0634-9

Van Eaton, A. R., & Wilson, C. J. N. (2013). The nature, origins and distribution of ash aggregates in a large-scale wet eruption deposit: Oruanui, New Zealand. *Journal of Volcanology and Geothermal Research*, *250*, 129–154. https://doi.org/10.1016/j.jvolgeores.2012.10.016

Wohletz, K. H., & Sheridan, M. F. (1983). Hydrovolcanic explosions II. Evolution of basaltic tuff rings and tuff cones. *American Journal of Science*, *283*(5), 385–413. https://doi.org/10.2475/ajs.283.5.385

Zhu, Y., Toon, O. B., Jensen, E. J., Bardeen, C. G., Mills, M. J., Tolbert, M. A., Yu, P., & Woods, S. (2020). Persisting volcanic ash particles impact stratospheric SO2 lifetime and aerosol optical properties. *Nature Communications*, *11*(1). https://doi.org/10.1038/s41467-020-18352-5

Chapter V - Summary and Conclusions

This thesis aimed to characterize the pyroclastic deposits from the maar complex of the Lamongan Volcanic Field (LVF) in East Java, Indonesia, in order better to understand maar eruption processes and the underlying magmatic system. An integrated analytical approach was employed utilizing the componentry, physical properties, and geochemistry of ash particles derived from six maars within the LVF: Ranu Pakis, Ranu Klakah, Ranu Kering, Ranu Air, an outcrop northeast of Ranu Kembar, and Ranu Segaran. Three main chapters addressed specific objectives to 1) determine the factors controlling ash particle variability, 2) elucidate the magmatic system through ash geochemistry, and 3) examine ash aggregate diversity and evolution of eruption styles.

Chapter II provided new insights into the factors influencing ash particle morphology by analyzing their textural, geochemical, and rheological properties. It was found that juvenile A ash particles (*cb*, *pb*, *bnv*, *bv*) exhibited typical blocky shapes and textures resulting from phreatomagmatic fragmentation. In contrast, juvenile B particles (*ob*) had irregular shapes denoting distinct magmatic fragmentation. Particle shapes were primarily controlled by fragmentation dynamics rather than magma properties.

Chapter III showed that fine ash geochemistry revealed consistent trends within types, indicating that the magmatic system comprised heterogeneous magma sources or batches. Mafic endmembers ashes (*cb-pb*, *bv*, and gray) represented fractional crystallization from relatively primitive magmas stored at depth, whereas more felsic ashes (*bnv* and *ob*) crystallized from shallower storage involving assimilation fractional crystallization. Scoria and eastern lavas represented parental magmas, limiting initial compositions before fractionation.

Chapter IV characterized units at Ranu Klakah and found increasing ash aggregate abundances correlated to shifts from drier to wetter eruptive conditions over time. Well-laminated aggregates highlighted peak water interactions. Varied brown juvenile and white

altered materials within aggregates fingerprinted fluctuating conduit processes and changing contributions of magma versus post-eruptive materials during phreatomagmatic activity.

In conclusion, this study demonstrates how the characterization of phreatomagmatic deposits provides insights into eruption dynamics and magmatic processes over short (eruption) and long (magmatic evolution) timescales. Ash particles morphology enabled distinguishing fragmentation mechanisms related to styles (magmatic vs. phreatomagmatic). Ash aggregates tracked escalating then waning hydrovolcanic activity. Geochemistry identified the magmatic system comprising variable storages and assimilation depths that crystallized compositionally diverse magmas. Future geochemical, textural, and mineralogical analyses could elucidate petrogenesis further. This research enhances scientific understanding of small-scale basaltic volcanism in LVF and other similar monogenetic volcanic fields.

APPENDICES

Appendix 1. Morphology parameters results of ash particles from the LVF maar complex. The calculation was done using PARTISAN Software by Dürig et al. (2018) ($_{LI}$ = Liu et al., 2015; $_{DL}$ = Dellino & La Volpe, 1996). The abbreviation means *Sol*= solidity; *Con*= convexity; *AR*= axial ratio; *FF*= form factor; *Com*= compactness; *Circ*= circularity; and *Rec*= rectangularity. The data was used for conventional shape descriptor plots and HCA analysis.

Samples	*No.*	*Type*	Sol_{LI}	Con_{LI}	AR_{LI}	*FF*	Elo_{DL}	Com_{DL}	$Circ_{DL}$	Rec_{DL}
1-9	2	cb	0.95	0.90	0.65	0.71	2.10	0.73	1.19	0.89
1-9	3	cb	0.97	0.95	0.57	0.74	2.38	0.71	1.16	0.85
1-9	4	cb	0.93	0.94	0.64	0.68	2.60	0.62	1.21	0.83
1-9	5	pb	0.94	0.91	0.71	0.71	2.10	0.71	1.18	0.87
1-9	6	pb	0.96	0.92	0.56	0.68	2.27	0.58	1.21	0.82
1-9	7	pb	0.96	0.94	0.85	0.78	1.67	0.69	1.13	0.83
1-9	8	pb	0.94	0.94	0.65	0.72	2.39	0.71	1.18	0.87
1-9	9	pb	0.93	0.93	0.43	0.61	3.00	0.64	1.28	0.87
1-9	10	pb	0.97	0.94	0.75	0.79	1.96	0.71	1.13	0.84
1-9	11	pb	0.90	0.92	0.44	0.59	2.78	0.58	1.31	0.86
1-9	12	bv	0.89	0.86	0.49	0.54	2.78	0.69	1.36	0.95
1-9	13	bv	0.92	0.92	0.63	0.64	2.46	0.61	1.25	0.86
1-9	14	bv	0.90	0.83	0.77	0.57	2.00	0.64	1.32	0.93
1-9	15	bv	0.90	0.83	0.77	0.58	1.78	0.68	1.31	0.96
1-9	16	bv	0.89	0.80	0.75	0.47	2.45	0.60	1.46	1.00
1-9	17	bv	0.93	0.85	0.72	0.62	2.03	0.65	1.27	0.91
1-9	18	bv	0.93	0.91	0.83	0.73	1.85	0.66	1.17	0.84
1-9	19	bnv	0.92	0.92	0.65	0.67	2.09	0.68	1.23	0.89
1-9	20	bnv	0.87	0.89	0.70	0.58	2.19	0.62	1.32	0.92
1-9	21	bnv	0.91	0.94	0.80	0.66	2.06	0.61	1.23	0.85
1-9	22	bnv	0.95	0.95	0.65	0.73	2.17	0.63	1.17	0.82
1-9	23	bnv	0.96	0.94	0.63	0.73	2.33	0.64	1.17	0.83
1-9	24	bnv	0.92	0.91	0.67	0.64	2.33	0.62	1.25	0.86
1-9	25	bnv	0.95	0.93	0.94	0.76	1.63	0.66	1.14	0.82
3-6	3	cb	0.90	0.90	0.54	0.63	2.43	0.64	1.26	0.89
3-6	4	cb	0.95	0.91	0.81	0.73	1.86	0.74	1.17	0.89
3-6	5	cb	0.88	0.88	0.63	0.57	2.55	0.64	1.32	0.93
3-6	6	pb	0.97	0.92	0.56	0.70	2.22	0.63	1.19	0.83
3-6	7	pb	0.97	0.93	0.82	0.77	1.78	0.80	1.14	0.89
3-6	8	pb	0.95	0.92	0.83	0.74	1.68	0.71	1.16	0.87
3-6	9	pb	0.93	0.93	0.57	0.64	2.59	0.64	1.25	0.87
3-6	10	bv	0.97	0.95	0.60	0.76	2.28	0.77	1.15	0.87
3-6	11	bv	0.94	0.93	0.84	0.75	1.87	0.74	1.16	0.88
3-6	12	bv	0.91	0.89	0.79	0.62	2.04	0.71	1.27	0.94
3-6	13	bv	0.87	0.86	0.46	0.52	2.82	0.65	1.39	0.95
3-6	14	bv	0.91	0.86	0.56	0.54	2.57	0.55	1.35	0.89
3-6	15	bnv	0.96	0.94	0.91	0.79	1.64	0.66	1.13	0.81

Appendix 1 - continues

3-6	16	bnv	0.93	0.93	0.54	0.63	2.94	0.59	1.26	0.85
3-6	17	bnv	0.97	0.93	0.86	0.80	1.60	0.74	1.11	0.85
3-6	18	bnv	0.95	0.94	0.61	0.72	2.27	0.77	1.18	0.90
3-6	19	bnv	0.96	0.92	0.76	0.75	1.81	0.72	1.15	0.86
3-6	20	bnv	0.96	0.94	0.64	0.76	2.17	0.71	1.15	0.84
3-6	21	bnv	0.96	0.93	0.82	0.75	1.78	0.70	1.15	0.85
3-6	22	bnv	0.95	0.93	0.76	0.74	1.86	0.71	1.16	0.86
3-6	23	bnv	0.95	0.91	0.75	0.70	1.87	0.75	1.20	0.91
3-6	24	bnv	0.96	0.94	0.67	0.78	2.04	0.74	1.13	0.84
4-6	2	cb	0.88	0.91	0.38	0.49	3.80	0.45	1.43	0.85
4-6	3	cb	0.87	0.90	0.69	0.63	2.22	0.65	1.26	0.89
4-6	4	pb	0.93	0.88	0.64	0.65	2.14	0.62	1.24	0.87
4-6	5	pb	0.97	0.93	0.92	0.80	1.52	0.70	1.12	0.83
4-6	6	bv	0.92	0.91	0.54	0.62	2.74	0.64	1.27	0.86
4-6	7	bv	0.94	0.93	0.93	0.73	1.69	0.69	1.17	0.86
4-6	8	bv	0.93	0.89	0.68	0.66	2.01	0.68	1.23	0.89
4-6	9	bv	0.93	0.81	0.87	0.58	1.71	0.67	1.32	0.95
4-6	10	bv	0.92	0.93	0.53	0.66	2.37	0.74	1.23	0.90
4-6	11	bnv	0.94	0.92	0.78	0.74	1.87	0.71	1.16	0.87
4-6	12	bnv	0.97	0.94	0.83	0.81	1.79	0.78	1.11	0.87
4-6	13	bnv	0.93	0.93	0.53	0.69	2.36	0.57	1.21	0.80
4-6	14	bnv	0.96	0.92	0.78	0.73	1.99	0.66	1.17	0.83
4-6	15	bnv	0.90	0.85	0.63	0.51	2.53	0.55	1.40	0.92
4-6	16	bnv	0.95	0.93	0.82	0.76	1.69	0.65	1.15	0.82
4-6	17	bnv	0.96	0.93	0.50	0.69	2.60	0.60	1.20	0.83
5-4	3	cb	0.94	0.93	0.83	0.75	1.77	0.61	1.15	0.80
5-4	4	cb	0.96	0.94	0.74	0.77	2.05	0.78	1.14	0.89
5-4	5	cb	0.96	0.94	0.86	0.76	1.82	0.66	1.15	0.82
5-4	6	pb	0.97	0.94	0.89	0.83	1.56	0.79	1.10	0.87
5-4	7	pb	0.97	0.95	0.78	0.81	1.67	0.77	1.11	0.86
5-4	8	pb	0.95	0.93	0.63	0.72	2.15	0.79	1.18	0.91
5-4	9	pb	0.91	0.92	0.53	0.64	2.71	0.57	1.25	0.82
5-4	10	bv	0.94	0.93	0.62	0.71	2.10	0.66	1.18	0.85
5-4	11	bv	0.93	0.89	0.90	0.69	1.82	0.65	1.21	0.86
5-4	12	bv	0.93	0.84	0.84	0.62	1.73	0.64	1.27	0.90
5-4	13	bv	0.98	0.94	0.90	0.81	1.53	0.81	1.11	0.89
5-4	14	bv	0.95	0.92	0.64	0.71	2.13	0.67	1.19	0.85
5-4	15	bv	0.96	0.88	0.63	0.62	2.37	0.64	1.27	0.90
5-4	16	bv	0.94	0.92	0.74	0.73	1.80	0.69	1.17	0.86
5-4	17	bnv	0.93	0.90	0.67	0.67	2.18	0.65	1.22	0.86
5-4	18	bnv	0.95	0.94	0.59	0.71	2.31	0.75	1.19	0.90
5-4	19	bnv	0.93	0.93	0.57	0.66	2.61	0.63	1.23	0.84
5-4	20	bnv	0.96	0.92	0.67	0.74	1.89	0.68	1.16	0.85
5-4	21	bnv	0.90	0.92	0.41	0.51	4.05	0.48	1.40	0.84
5-4	22	bnv	0.96	0.93	0.84	0.72	1.92	0.59	1.18	0.81
5-4	23	bnv	0.92	0.93	0.52	0.64	2.77	0.71	1.25	0.89
5-4	24	bnv	0.96	0.95	0.89	0.78	1.81	0.66	1.13	0.81
13-11	2	ob	0.58	0.65	0.54	0.20	3.63	0.39	2.25	1.24
13-11	3	ob	0.71	0.84	0.33	0.37	3.81	0.44	1.64	0.94

Appendix 1 - continues

13-11	4	ob	0.76	0.54	0.86	0.21	2.00	0.53	2.20	1.42
13-11	5	ob	0.89	0.86	0.45	0.49	3.29	0.55	1.43	0.92
13-11	6	ob	0.84	0.86	0.60	0.49	2.92	0.54	1.42	0.90
13-11	7	ob	0.71	0.58	0.55	0.21	3.16	0.51	2.20	1.36
13-11	8	cb	0.94	0.92	0.72	0.64	2.27	0.62	1.25	0.86
13-11	9	pb	0.88	0.89	0.43	0.54	3.18	0.54	1.36	0.87
13-11	10	pb	0.94	0.89	0.90	0.70	1.68	0.70	1.20	0.89
13-11	11	pb	0.95	0.92	0.92	0.76	1.62	0.70	1.15	0.85
13-11	12	pb	0.86	0.90	0.48	0.54	3.11	0.57	1.36	0.87
13-11	13	pb	0.94	0.94	0.79	0.67	2.06	0.61	1.22	0.84
13-11	14	bv	0.93	0.91	0.58	0.65	2.33	0.75	1.24	0.92
13-11	15	bv	0.92	0.94	0.43	0.59	3.25	0.52	1.30	0.83
13-11	16	bv	0.87	0.74	0.52	0.40	2.83	0.58	1.58	1.07
13-11	17	bv	0.98	0.95	0.97	0.84	1.50	0.79	1.09	0.86
13-11	18	bv	0.96	0.87	0.90	0.67	1.63	0.76	1.22	0.94
13-11	19	bv	0.94	0.91	0.88	0.74	1.71	0.75	1.16	0.89
13-11	20	bv	0.93	0.81	0.53	0.51	2.41	0.63	1.40	0.96
13-11	21	bv	0.94	0.93	0.69	0.72	1.98	0.82	1.18	0.93
13-11	22	bnv	0.94	0.93	0.62	0.72	2.02	0.68	1.18	0.86
13-11	23	bnv	0.91	0.91	0.84	0.67	1.70	0.62	1.23	0.85
13-11	24	bnv	0.88	0.83	0.58	0.49	2.89	0.63	1.43	0.98
13-11	25	bnv	0.96	0.93	0.96	0.77	1.64	0.67	1.14	0.82
13-11	26	bnv	0.98	0.95	0.65	0.79	2.10	0.69	1.12	0.82
13-11	27	bnv	0.95	0.94	0.91	0.74	1.76	0.67	1.16	0.84
13-11	28	bnv	0.87	0.91	0.74	0.65	2.08	0.65	1.24	0.88
13-11	29	bnv	0.92	0.93	0.68	0.70	2.23	0.64	1.20	0.85
13-11	30	bnv	0.97	0.94	0.81	0.79	1.59	0.67	1.12	0.81
13-11	31	bnv	0.91	0.91	0.67	0.66	2.01	0.62	1.23	0.85
14-4a	2	ob	0.79	0.71	0.88	0.34	2.26	0.49	1.72	1.06
14-4a	3	ob	0.75	0.78	0.55	0.37	2.99	0.49	1.65	1.01
14-4a	4	ob	0.47	0.48	0.76	0.09	4.27	0.31	3.28	1.63
14-4a	5	ob	0.89	0.74	0.87	0.46	1.74	0.66	1.48	1.06
14-4a	6	ob	0.61	0.59	0.81	0.18	3.17	0.41	2.37	1.35
14-4a	7	ob	0.86	0.81	0.60	0.48	2.45	0.59	1.44	0.97
14-4a	8	ob	0.73	0.77	0.58	0.36	3.30	0.51	1.68	1.06
14-4a	9	cb	0.95	0.90	0.74	0.71	1.96	0.69	1.19	0.87
14-4a	10	cb	0.94	0.90	0.86	0.69	1.86	0.66	1.21	0.86
14-4a	11	cb	0.94	0.92	0.83	0.72	1.80	0.65	1.18	0.84
14-4a	12	pb	0.98	0.94	0.87	0.82	1.67	0.77	1.10	0.86
14-4a	13	pb	0.95	0.92	0.67	0.72	2.10	0.66	1.17	0.84
14-4a	14	pb	0.97	0.95	0.95	0.79	1.52	0.69	1.13	0.83
14-4a	15	pb	0.96	0.94	0.73	0.78	1.78	0.70	1.13	0.84
14-4a	16	pb	0.93	0.91	0.47	0.61	2.87	0.53	1.28	0.83
14-4a	17	bv	0.93	0.84	0.69	0.59	1.95	0.62	1.30	0.91
14-4a	18	bv	0.96	0.92	0.58	0.67	2.41	0.56	1.22	0.81
14-4a	19	bv	0.84	0.82	0.70	0.46	2.75	0.56	1.47	0.97
14-4a	20	bv	0.84	0.85	0.76	0.48	2.67	0.56	1.44	0.95
14-4a	21	bv	0.89	0.81	0.54	0.47	2.55	0.53	1.46	0.94
14-4a	22	bv	0.95	0.92	0.57	0.67	2.33	0.58	1.22	0.83

Appendix 1 - continues

14-4a	23	bv	0.96	0.94	0.80	0.77	1.76	0.73	1.14	0.86
14-4a	24	bv	0.93	0.92	0.68	0.72	1.99	0.65	1.18	0.84
14-4a	25	bv	0.95	0.92	0.82	0.75	1.66	0.74	1.16	0.88
14-4a	26	bv	0.91	0.84	0.50	0.55	2.61	0.65	1.35	0.94
14-4a	27	bv	0.96	0.93	0.71	0.78	1.86	0.72	1.13	0.84
14-4a	28	bv	0.78	0.82	0.47	0.43	3.06	0.63	1.53	1.04
14-4a	29	bnv	0.94	0.93	0.84	0.74	1.90	0.64	1.17	0.83
14-4a	30	bnv	0.93	0.90	0.93	0.71	1.72	0.73	1.19	0.90
14-4a	31	bnv	0.94	0.84	0.77	0.62	1.93	0.74	1.27	0.97
14-4a	32	bnv	0.97	0.93	0.73	0.78	1.93	0.70	1.13	0.83
14-4a	33	bnv	0.96	0.93	0.70	0.75	2.03	0.66	1.15	0.83
14-4a	34	bnv	0.96	0.94	0.60	0.71	2.34	0.64	1.19	0.83
14-4a	35	bnv	0.95	0.94	0.75	0.76	1.91	0.67	1.15	0.83
14-4a	36	bnv	0.82	0.86	0.43	0.45	3.27	0.52	1.49	0.92
19-3	2	cb	0.94	0.92	0.81	0.76	1.64	0.67	1.15	0.83
19-3	3	pb	0.95	0.88	0.73	0.69	1.91	0.68	1.20	0.88
19-3	4	pb	0.97	0.94	0.82	0.80	1.69	0.69	1.12	0.82
19-3	5	pb	0.94	0.92	0.74	0.73	1.94	0.66	1.17	0.84
19-3	6	pb	0.92	0.91	0.81	0.69	2.08	0.63	1.20	0.84
19-3	7	bv	0.94	0.93	0.50	0.65	2.57	0.71	1.24	0.89
19-3	8	bv	0.88	0.90	0.61	0.59	2.53	0.58	1.30	0.87
19-3	9	bv	0.93	0.86	0.64	0.62	2.07	0.64	1.27	0.90
19-3	10	bv	0.95	0.89	0.71	0.69	1.90	0.75	1.20	0.91
19-3	11	bv	0.84	0.77	0.60	0.43	2.76	0.61	1.53	1.04
19-3	12	bv	0.96	0.90	0.70	0.73	1.82	0.69	1.17	0.86
19-3	13	bv	0.95	0.93	0.53	0.70	2.54	0.61	1.20	0.82
19-3	14	bv	0.96	0.92	0.94	0.77	1.60	0.70	1.14	0.85
19-3	15	bv	0.94	0.90	0.46	0.60	2.70	0.63	1.29	0.89
19-3	16	bv	0.94	0.92	0.68	0.70	2.09	0.64	1.20	0.85
19-3	17	bnv	0.93	0.89	0.61	0.65	2.04	0.71	1.24	0.92
20-2a	3	cb	0.97	0.93	0.77	0.79	1.75	0.76	1.13	0.86
20-2a	4	cb	0.95	0.92	0.54	0.67	2.65	0.69	1.22	0.87
20-2a	5	cb	0.90	0.86	0.53	0.56	2.46	0.65	1.34	0.93
20-2a	6	cb	0.94	0.93	0.68	0.70	2.36	0.65	1.20	0.85
20-2a	7	pb	0.96	0.91	0.77	0.73	1.95	0.65	1.17	0.83
20-2a	8	pb	0.94	0.93	0.74	0.73	2.06	0.72	1.17	0.87
20-2a	9	pb	0.94	0.92	0.74	0.71	2.08	0.65	1.19	0.85
20-2a	10	pb	0.96	0.94	0.72	0.78	2.00	0.71	1.14	0.85
20-2a	11	pb	0.94	0.92	0.77	0.74	1.98	0.65	1.16	0.83
20-2a	12	bv	0.96	0.89	0.53	0.59	2.57	0.68	1.30	0.92
20-2a	13	bv	0.95	0.94	0.61	0.71	2.28	0.62	1.18	0.83
20-2a	14	bv	0.97	0.94	0.48	0.66	3.09	0.65	1.23	0.84
20-2a	15	bv	0.92	0.91	0.88	0.68	1.77	0.66	1.21	0.87
20-2a	16	bv	0.95	0.94	0.70	0.78	1.85	0.69	1.13	0.83
20-2a	17	bv	0.96	0.90	0.82	0.74	1.73	0.71	1.16	0.87
20-2a	18	bv	0.91	0.88	0.59	0.61	2.24	0.63	1.28	0.89
20-2a	19	bv	0.97	0.93	0.78	0.78	1.85	0.77	1.13	0.88
20-2a	20	bv	0.91	0.92	0.44	0.61	2.70	0.70	1.28	0.92
20-2a	21	bv	0.92	0.88	0.86	0.67	1.77	0.64	1.23	0.87

Appendix 1 - continues

20-2a	22	bv	0.92	0.87	0.73	0.64	1.88	0.66	1.25	0.90
20-2a	23	bv	0.95	0.90	0.63	0.67	2.06	0.69	1.22	0.89
20-2a	24	bv	0.97	0.94	0.86	0.81	1.65	0.73	1.11	0.84
20-2a	25	bv	0.91	0.85	0.72	0.58	2.04	0.71	1.32	0.97
20-2a	26	bv	0.97	0.94	0.86	0.81	1.59	0.74	1.11	0.85
20-2a	27	bv	0.94	0.90	0.68	0.68	2.03	0.65	1.21	0.87
20-2a	28	bnv	0.96	0.93	0.51	0.68	2.61	0.65	1.21	0.84
20-2a	29	bnv	0.98	0.95	0.89	0.83	1.54	0.75	1.10	0.84
20-2a	30	bnv	0.95	0.94	0.70	0.77	1.97	0.66	1.14	0.81
20-2a	31	bnv	0.95	0.94	0.60	0.73	2.22	0.64	1.17	0.82
43-3a	2	cb	0.94	0.85	0.80	0.63	1.84	0.64	1.26	0.90
43-3a	3	cb	0.92	0.84	0.82	0.60	1.77	0.71	1.30	0.96
43-3a	4	pb	0.92	0.89	0.66	0.60	2.35	0.59	1.29	0.88
43-3a	5	pb	0.85	0.77	0.41	0.34	3.66	0.55	1.72	1.06
43-3a	6	pb	0.89	0.89	0.46	0.50	3.38	0.53	1.42	0.90
43-3a	7	pb	0.96	0.92	0.62	0.72	2.28	0.66	1.18	0.85
43-3a	8	pb	0.95	0.92	0.48	0.61	3.02	0.56	1.28	0.84
43-3a	9	bv	0.91	0.86	0.63	0.59	2.31	0.58	1.30	0.87
43-3a	10	bv	0.89	0.87	0.72	0.62	1.97	0.61	1.27	0.88
43-3a	11	bv	0.92	0.80	0.81	0.56	1.70	0.71	1.33	0.99
43-3a	12	bv	0.91	0.88	0.76	0.65	2.02	0.68	1.24	0.91
43-3a	13	bv	0.93	0.73	0.77	0.46	1.86	0.76	1.47	1.14
43-3a	14	bv	0.92	0.87	0.71	0.62	2.06	0.69	1.27	0.92
43-3a	15	bv	0.90	0.83	0.64	0.51	2.42	0.63	1.40	0.96
43-3a	16	bv	0.92	0.89	0.81	0.66	1.77	0.73	1.23	0.93
43-3a	17	bv	0.92	0.91	0.59	0.66	2.37	0.65	1.23	0.86
43-3a	18	bv	0.90	0.87	0.88	0.59	1.84	0.63	1.30	0.92
43-3a	19	bv	0.96	0.92	0.63	0.69	2.28	0.65	1.21	0.86
43-3a	20	bnv	0.91	0.80	0.86	0.53	2.00	0.61	1.37	0.94
43-3a	21	bnv	0.92	0.86	0.50	0.57	2.58	0.65	1.33	0.93
43-3a	22	bnv	0.95	0.92	0.89	0.75	1.69	0.72	1.16	0.87
43-7a	3	cb	0.94	0.88	0.81	0.68	1.86	0.67	1.21	0.88
43-7a	4	pb	0.96	0.88	0.88	0.70	1.65	0.67	1.20	0.87
43-7a	5	pb	0.90	0.85	0.92	0.61	1.86	0.61	1.28	0.88
43-7a	6	pb	0.91	0.80	0.77	0.55	1.94	0.63	1.35	0.95
43-7a	7	pb	0.93	0.84	0.84	0.61	1.67	0.67	1.28	0.93
43-7a	8	pb	0.93	0.87	0.64	0.61	2.24	0.61	1.29	0.89
43-7a	9	pb	0.86	0.78	0.43	0.43	2.82	0.70	1.53	1.08
43-7a	10	pb	0.95	0.92	0.52	0.68	2.35	0.77	1.21	0.90
43-7a	11	pb	0.92	0.75	0.78	0.49	2.00	0.64	1.43	1.01
43-7a	12	bv	0.93	0.76	0.84	0.52	1.64	0.73	1.39	1.05
43-7a	13	bv	0.88	0.79	0.85	0.51	1.77	0.71	1.40	1.04
43-7a	14	bv	0.94	0.86	0.92	0.66	1.68	0.74	1.23	0.93
43-7a	15	bv	0.92	0.78	0.78	0.52	2.01	0.77	1.39	1.08
43-7a	16	bv	0.92	0.84	0.89	0.60	1.67	0.70	1.29	0.95
43-7a	17	bv	0.93	0.83	0.84	0.60	1.90	0.68	1.29	0.94
43-7a	18	bv	0.87	0.76	0.77	0.45	1.99	0.57	1.49	1.00
43-7a	19	bv	0.91	0.86	0.72	0.60	2.11	0.63	1.29	0.90
43-7a	20	bv	0.88	0.78	0.86	0.49	1.89	0.69	1.43	1.05

Appendix 1 - continues

43-7a	21	bnv	0.91	0.80	0.79	0.54	2.00	0.70	1.36	1.01
43-7a	22	bnv	0.91	0.85	0.89	0.61	1.72	0.65	1.28	0.91
43-7a	23	bnv	0.93	0.88	0.69	0.66	2.00	0.70	1.23	0.90
45-a	2	cb	0.91	0.90	0.83	0.67	1.70	0.63	1.22	0.86
45-a	3	pb	0.93	0.88	0.61	0.62	2.38	0.59	1.27	0.87
45-a	4	pb	0.96	0.89	0.61	0.66	2.36	0.66	1.23	0.87
45-a	5	pb	0.98	0.93	0.68	0.74	2.27	0.64	1.16	0.81
45-a	6	pb	0.94	0.89	0.72	0.70	2.01	0.70	1.20	0.88
45-a	7	pb	0.98	0.95	0.79	0.84	1.71	0.78	1.09	0.85
45-a	8	bv	0.95	0.87	0.81	0.67	1.71	0.67	1.22	0.88
45-a	9	bv	0.92	0.88	0.46	0.55	2.81	0.53	1.34	0.86
45-a	10	bv	0.92	0.90	0.60	0.59	2.97	0.57	1.30	0.85
45-a	11	bv	0.90	0.81	0.90	0.53	1.80	0.64	1.37	0.97
45-a	12	bv	0.95	0.90	0.59	0.69	2.21	0.75	1.21	0.90
45-a	13	bnv	0.93	0.78	0.50	0.45	2.81	0.52	1.49	0.94
45-a	14	bnv	0.97	0.91	0.81	0.76	1.69	0.75	1.15	0.88
45-a	15	bnv	0.92	0.89	0.71	0.65	2.03	0.67	1.24	0.90
45-b	3	cb	0.93	0.86	0.43	0.61	2.08	0.62	1.28	0.88
45-b	4	pb	0.90	0.82	0.76	0.54	2.07	0.65	1.36	0.97
45-b	5	pb	0.96	0.92	0.30	0.77	1.54	0.71	1.14	0.85
45-b	6	pb	0.93	0.83	0.07	0.59	1.81	0.67	1.30	0.94
45-b	7	pb	0.93	0.92	0.31	0.69	2.36	0.60	1.21	0.83
45-b	8	pb	0.94	0.90	0.32	0.67	2.27	0.66	1.22	0.88
45-b	9	pb	0.83	0.76	0.56	0.38	3.05	0.48	1.63	0.99
45-b	10	bv	0.94	0.88	0.62	0.66	2.03	0.76	1.23	0.93
45-b	11	bv	0.93	0.90	0.37	0.67	1.78	0.67	1.22	0.88
45-b	12	bv	0.91	0.91	0.51	0.57	2.77	0.52	1.32	0.84
45-b	13	bv	0.95	0.88	0.52	0.67	1.85	0.70	1.22	0.90
45-b	14	bv	0.87	0.73	0.61	0.40	2.41	0.60	1.58	1.06
45-b	15	bv	0.91	0.85	0.85	0.58	2.33	0.69	1.31	0.94
45-b	16	bnv	0.89	0.76	0.20	0.43	2.48	0.57	1.53	1.01
45-b	17	bnv	0.95	0.86	0.57	0.66	1.94	0.69	1.23	0.90
45-b	18	bnv	0.89	0.76	0.81	0.48	1.98	0.68	1.44	1.05

Appendix 2. Parameters used for PCA Analysis.

Samples	*1-3*	*1-3*	*1-3*	*1-3*	*1-3*	*5-12a*	*5-12a*	*5-12a*	*5-12a*	*13-2*	*13-2*	*13-2*	*20-1*	*20-1*	*20-1*	*20-1*
ID	cb2	pb2	bv4	bnv-m3	ob2	cb1	pb1	bv2	bnv-m2	bv3	bnv-m1	ob5	pb1	bv3	bnv1	bnv-m1
Type	***cb***	***pb***	***bv***	***bnv***	***ob***	***cb***	***pb***	***bv***	***bnv***	***bv***	***bnv***	***ob***	***pb***	***bv***	***bnv***	***bnv***
Ves	18.00	24.00	27.00	8.00	19.00	22.00	17.00	28.00	3.00	19.00	6.00	3.00	11.00	33.00	11.00	8.00
Cry	27.13	26.46	40.56	42.33	0.35	50.11	27.41	45.63	48.61	19.06	40.09	15.50	63.19	25.00	39.08	58.16
VND	3.87	2.56	11.50	9.26	0.92	7.02	3.81	11.90	24.00	4.16	21.00	0.55	24.40	33.00	8.07	9.26
ηr	2.93	2.33	3.75	4.47	2.68	4.63	3.57	3.53	5.86	3.89	4.83	4.29	5.37	4.34	4.32	6.24
Sol_{LI}	0.95	0.94	0.91	0.92	0.75	0.95	0.95	0.94	0.94	0.91	0.93	0.73	0.95	0.94	0.96	0.93
Con_{LI}	0.93	0.93	0.86	0.93	0.72	0.93	0.93	0.90	0.93	0.88	0.91	0.70	0.93	0.91	0.94	0.89
AR_{LI}	0.62	0.63	0.71	0.72	0.56	0.81	0.71	0.75	0.64	0.65	0.72	0.72	0.75	0.70	0.67	0.61
FF	0.71	0.70	0.59	0.68	0.33	0.76	0.75	0.70	0.68	0.61	0.69	0.33	0.74	0.69	0.75	0.65
Elo_{DL}	2.36	2.31	2.19	2.11	3.13	1.88	2.02	1.92	2.44	2.30	2.13	2.88	2.01	2.07	2.09	2.04
Com_{DL}	0.69	0.66	0.65	0.64	0.49	0.68	0.73	0.68	0.64	0.63	0.66	0.49	0.68	0.68	0.68	0.71
$Circ_{DL}$	1.19	1.20	1.31	1.21	1.86	1.15	1.16	1.20	1.22	1.30	1.22	1.94	1.17	1.21	1.16	1.24
Rec_{DL}	0.86	0.85	0.92	0.86	1.13	0.84	0.86	0.87	0.85	0.90	0.87	1.16	0.84	0.88	0.83	0.92
SiO_2	46.74	46.53	48.16	50.50	51.35	47.99	47.94	48.69	51.49	50.73	50.70	53.18	46.24	49.28	49.65	50.92
TiO_2	1.01	0.96	0.87	1.36	1.69	1.04	1.00	1.15	1.55	1.51	1.40	1.49	1.19	1.16	1.22	1.35
$Al2O_3$	20.81	20.91	19.24	17.60	16.80	19.91	19.98	19.51	17.00	17.00	17.39	16.31	19.33	17.79	18.35	17.66
FeOt	13.83	14.01	12.72	12.91	13.70	13.03	12.71	12.94	13.07	13.33	12.77	13.03	13.42	12.26	12.04	12.22
MnO	0.22	0.20	0.23	0.21	0.21	0.19	0.20	0.20	0.20	0.22	0.21	0.25	0.19	0.19	0.19	0.19
MgO	5.22	5.36	5.03	4.25	3.44	4.73	4.60	4.45	3.74	4.21	4.27	3.27	5.62	5.31	4.50	4.22
CaO	9.97	9.93	10.99	9.12	7.97	10.61	11.06	10.12	8.47	8.82	9.22	7.58	11.49	10.31	10.05	9.15
Na_2O	1.77	1.70	2.08	2.47	3.00	1.92	1.94	2.10	2.63	2.52	2.51	2.97	1.82	2.38	2.53	2.62
K_2O	0.27	0.25	0.46	1.23	1.31	0.41	0.42	0.61	1.47	1.33	1.23	1.58	0.55	1.10	1.23	1.34
P_2O_5	0.15	0.16	0.21	0.35	0.53	0.17	0.17	0.24	0.39	0.34	0.32	0.34	0.14	0.21	0.24	0.32

* ηr = relative viscosity; FeOt = total iron.

Appendix 3. Whole-rock geochemical compositions from XRF analysis. (Sample region) WM= West maar; NM= North maar, EM= East maar; NL= North lava; EL= East lava; and NSC= North scoria cone. (Sample location) RP= Ranu Pakis; RK= Ranu Klakah; RKe= Ranu Kering; RA= Ranu Air; NRK= NE Ranu Kembar; RS= Ranu Segaran; nl= North lava; el= East lava; and sc= North scoria cone.

Region	***WM***	***WM***	***WM***	***WM***	***WM***	***WM***	***WM***	***WM***	***WM***
Location	**RP**	**RP**	**RP**	**RP**	**RP**	**RP**	**RP**	**RP**	**RP**
Stage	*2*	*2*	*2*	*2*	*2*	*2*	*2*	*2*	*2*
Sample	1-2 black	1-3 black (lapilli)	1-3 black	1-3 ob (lapilli)	1-5 ob (lapilli)	1-5 black (lapilli)	1-6 black	1-9 ob (lapilli)	1-9 black massive (lapilli)
Size	**bnv**	**bv**	**bnv**	**ob**	**ob**	**bv**	**bnv**	**ob**	**bnv**
Condition	*low-mod coated*	*clean*	*mod coated*	*mod-high coated*	*mod coated*	*low-mod coated*	*mod-high coated*	*low-mod coated*	*low coated*
SiO_2	50.27	48.13	49.62	50.77	50.71	52.16	49.98	51.99	52.01
TiO_2	1.33	0.91	1.23	1.68	1.67	1.62	1.34	1.69	1.76
$Al2O_3$	17.36	19.20	17.91	17.28	16.53	16.65	17.52	16.39	16.11
FeOt	12.79	12.72	12.62	14.00	13.73	12.40	12.86	13.22	13.11
MnO	0.21	0.23	0.21	0.19	0.23	0.20	0.21	0.21	0.20
MgO	4.25	5.02	4.39	2.74	3.97	3.69	4.28	3.58	3.63
CaO	9.10	10.99	9.51	8.08	7.99	7.88	9.26	7.75	7.93
Na_2O	2.42	2.04	2.38	3.19	2.95	2.79	2.41	2.84	2.69
K_2O	1.22	0.46	1.04	1.10	1.30	1.79	1.15	1.51	1.80
P_2O_5	0.331	0.200	0.321	0.573	0.523	0.446	0.326	0.476	0.453
LOI	0.215	-0.037	0.049	2.343	0.920	0.454	0.665	0.933	0.449
Total	99.27	99.90	99.24	99.60	99.61	99.63	99.34	99.65	99.68
V	242	300	473	237	235	326	238	216	284
Cr	7	6	7	9	10	15	9	8	17
Ni	16	6	9	13	13	18	17	16	20
Rb	31	4	27	16	30	47	29	40	58
Sr	443	535	463	454	405	400	445	389	372
Y	25	16	22	31	32	31	25	33	35
Zr	129	62	112	161	149	173	123	172	192
Nb	3	3	4	19	7	7	5	11	17
Ba	668	240	482	669	586	680	620	676	648

Appendix 3 – continues

Region	***WM***	***WM***	***WM***	***WM***	***WM***	***WM***	***WM***	***WM***	***WM***
Location	**RP**	**RP**	**RP**	**RP**	**RP**	**RP**	**RP**	**RK**	**RK**
Stage	*2*	*2*	*1*	*1*	*1*	*1*	*1*	*3*	*3*
Sample	1-9 bv (lapilli)	1-9 black	3-3 black (lapilli)	3-3 greenish black	3-3 cb-pb (lapilli)	3-3 cb-pb	3-7 greenish black	4-12b black	4-12b
Size	**bv**	**bnv**	**bv**	**bnv**	**cb-pb**	**cb-pb**	**bnv**	**bnv**	**cb-pb**
Condition	*low coated*	*mod-high coated*	*low coated*	*clean*	*highly coated*	*low coated*	*clean-low coated*	*clean*	*low-mod coated*
SiO_2	48.05	49.24	50.66	50.78	46.66	46.27	51.31	51.42	47.33
TiO_2	0.87	1.17	1.37	1.50	1.01	0.95	1.60	1.64	1.05
$Al2O_3$	19.20	18.10	17.46	17.00	20.77	20.79	16.84	16.36	19.01
FeOt	12.69	12.68	12.90	13.00	13.80	13.93	12.90	13.38	13.13
MnO	0.23	0.22	0.22	0.21	0.22	0.20	0.20	0.20	0.20
MgO	5.02	4.54	4.19	3.96	5.21	5.33	3.77	3.77	4.86
CaO	10.97	9.85	8.61	8.29	9.95	9.87	8.05	7.99	10.06
Na_2O	2.08	2.27	2.59	2.63	1.77	1.69	2.71	2.71	1.99
K_2O	0.46	0.91	1.43	1.45	0.27	0.25	1.56	1.62	0.54
P_2O_5	0.205	0.294	0.363	0.386	0.153	0.158	0.417	0.437	0.199
LOI	0.190	0.137	0.669	-0.098	2.608	2.062	0.245	0.368	0.632
Total	99.77	99.27	99.77	99.21	99.81	99.44	99.37	99.52	98.37
V	366	311	323	494	275	307	470	554	289
Cr	8	10	11	15	9	11	11	16	23
Ni	7	15	13	19	12	2	19	16	8
Rb	3	23	36	41	2	3	46	49	8
Sr	530	474	443	411	490	482	405	393	497
Y	14	21	25	28	14	14	29	32	18
Zr	64	102	136	151	62	66	161	172	88
Nb	b.d	b.d	16	12	3	b.d	5	5	0
Ba	225	389	523	613	207	275	649	862	363

Appendix 3 – continues

Region	***WM***	***WM***	***WM***	***WM***	***WM***	***WM***	***WM***	***WM***	***WM***
Location	**RK**	**RK**	**RK**	**RK**	**RK**	**RK**	**RK**	**RK**	**RK**
Stage	3	3	3	2	2	2	2	2	2
Sample	4-13 black (lapilli)	4-13 black	4-13 cb	4-4 black	4-5 black	4-6 black	4-6 cb	4-6 black lava? (lapilli)	4-6 black juv? (lapilli)
Size	**bnv**	**bnv**	**cb-pb**	**bnv**	**bnv**	**bnv**	**cb-pb**	**bnv**	**bv**
Condition	*mod-high coated*	*clean-low coated*	*mod coated*	*mod-high coated*	*clean*	*mod-high coated*	*mod coated*	*low coated*	*mod coated*
SiO_2	51.08	50.92	47.11	51.17	51.59	51.41	47.91	53.02	48.61
TiO_2	1.48	1.56	1.06	1.58	1.56	1.57	1.01	1.63	1.15
$Al2O_3$	17.01	16.95	19.79	16.77	16.54	16.78	19.94	16.26	19.48
FeOt	12.97	13.24	13.09	13.00	13.50	13.10	12.65	12.47	12.92
MnO	0.20	0.20	0.20	0.19	0.20	0.19	0.18	0.19	0.20
MgO	3.98	3.95	4.85	3.70	3.64	3.63	4.41	3.34	4.45
CaO	8.51	8.49	10.63	8.36	8.07	8.29	10.66	7.57	10.11
Na_2O	2.54	2.61	1.93	2.57	2.62	2.65	1.87	2.98	2.09
K_2O	1.43	1.39	0.40	1.50	1.51	1.48	0.36	1.84	0.61
P_2O_5	0.354	0.386	0.166	0.393	0.379	0.398	0.157	0.431	0.235
LOI	0.820	0.336	0.926	0.266	0.751	0.619	1.708	0.856	1.620
Total	99.55	99.68	99.22	99.22	99.60	99.50	99.14	99.72	99.85
V	274	463	357	484	532	376	254	403	390
Cr	13	20	9	26	12	12	8	17	9
Ni	22	13	20	21	14	15	1	15	9
Rb	38	41	6	46	48	46	6	53	10
Sr	415	410	510	402	396	399	520	378	490
Y	29	30	16	30	30	29	15	33	19
Zr	150	156	78	161	164	162	70	182	90
Nb	4	13	b.d	3	8	5	2	21	4
Ba	568	681	277	578	612	665	212	677	293

Appendix 3 – continues

Region	***WM***	***WM***	***WM***	***WM***	***WM***	***WM***	***WM***	***WM***	***NM***
Location	**RK**	**RK**	**RK**	**RK**	**RK**	**RK**	**RK**	**RK**	**RKe**
Stage	2	2	2	2	3	3	3	3	3
Sample	4-6 black B	4-6 cb B	4-8 black	4-11d black	5-12a black	5-13 black	5-14 black	5-14 pb	14-4a black massive (lapilli)
Size	**bnv**	**cb-pb**	**bnv**	**bnv**	**bnv**	**bnv**	**bnv**	**cb-pb**	**bnv**
Condition	*mod-high coated*	*mod-high coated*	*low coated*	*highly coated*	*low-mod coated*	*clean*	*clean-low coated*	*low coated*	*mod coated*
SiO_2	51.94	47.59	51.81	51.43	50.23	50.85	50.99	47.34	51.49
TiO_2	1.61	0.98	1.60	1.56	1.38	1.46	1.52	0.98	1.55
$Al2O_3$	16.30	20.07	16.73	17.07	17.75	17.51	17.28	19.73	16.71
FeOt	13.22	12.72	12.93	12.91	12.63	12.55	12.63	12.55	12.75
MnO	0.19	0.19	0.19	0.19	0.20	0.20	0.20	0.20	0.21
MgO	3.63	4.58	3.47	3.46	3.93	3.79	3.76	4.55	4.04
CaO	7.94	10.63	8.10	8.46	9.16	8.98	8.75	10.92	8.55
Na_2O	2.69	1.81	2.67	2.71	2.44	2.62	2.61	1.92	2.66
K_2O	1.63	0.33	1.60	1.41	1.22	1.32	1.43	0.41	1.35
P_2O_5	0.408	0.147	0.413	0.371	0.329	0.368	0.381	0.165	0.378
LOI	0.591	1.432	0.834	0.858	0.293	0.364	0.345	0.938	0.887
Total	99.55	99.03	99.52	99.57	99.27	99.64	99.56	98.75	99.69
V	345	175	414	393	555	569	591	317	367
Cr	22	12	23	24	10	12	15	11	30
Ni	16	16	16	13	13	9	9	5	24
Rb	49	4	50	41	33	38	41	5	34
Sr	388	517	401	414	444	432	430	534	406
Y	32	15	31	28	26	28	29	15	29
Zr	174	65	170	152	131	146	151	72	145
Nb	3	b.d	11	4	1	1	6	b.d	14
Ba	1267	268	639	601	480	576	688	243	480

Appendix 3 – continues

Region	***NM***	***NM***	***NM***	***NM***	***NM***	***NM***	***NM***	***NM***	***NM***
Location	**RKe**	**RKe**	**RKe**	**RKe**	**RKe**	**RKe**	**RKe**	**RKe**	**RKe**
Stage	3	3	3	3	3	3	3	2	2
Sample	14-4a black	14-4a ob (lapilli)	14-4a ob	14-3a black (lapilli)	14-3a black	14-3a ob (lapilli)	14-2 black	13-11 black (lapilli)	13-11 black
Size	**bnv**	**ob**	**ob**	**bv**	**bv**	**ob**	**bnv**	**bnv**	**bnv**
Condition	*mod coated*	*highly coated*	*low coated*	*mod coated*	*mod coated*	*mod coated*	*low-mod coated*	*low coated*	*clean*
SiO_2	50.43	53.29	52.25	48.68	48.60	53.27	49.15	50.62	51.04
TiO_2	1.36	1.48	1.52	1.19	1.24	1.54	1.23	1.62	1.62
$Al2O_3$	17.27	16.29	16.55	18.35	17.92	15.78	17.75	16.41	16.42
FeOt	12.61	13.13	12.88	13.12	12.97	13.22	12.74	13.86	13.17
MnO	0.21	0.21	0.23	0.22	0.22	0.23	0.21	0.24	0.20
MgO	4.46	3.06	3.35	4.82	4.89	3.15	4.65	4.11	4.08
CaO	9.31	7.05	7.75	10.13	10.10	7.18	9.91	8.41	8.45
Na_2O	2.42	3.05	2.81	2.34	2.24	3.14	2.30	2.61	2.58
K_2O	1.12	1.65	1.49	0.75	0.79	1.71	0.90	1.43	1.51
P_2O_5	0.299	0.338	0.365	0.233	0.222	0.375	0.240	0.380	0.370
LOI	0.069	1.543	1.027	0.550	0.098	0.888	0.173	0.205	0.462
Total	99.47	99.54	99.20	99.83	99.19	99.59	99.08	99.68	99.44
V	529	266	211	311	603	365	296	422	186
Cr	24	12	17	16	14	9	18	16	26
Ni	18	10	10	15	11	11	15	13	23
Rb	29	47	42	11	18	48	18	39	42
Sr	407	357	383	448	432	336	422	382	387
Y	25	29	30	21	20	31	22	29	30
Zr	126	147	143	91	90	153	100	147	146
Nb	1	6	7	17	b.d	25	5	5	4
Ba	399	643	813	319	323	550	370	509	669

Appendix 3 – continues

Region	***NM***	***NM***	***NM***	***NM***	***NM***	***NM***	***NM***	***NM***	***NM***
Location	**RKe**	**RKe**	**RKe**	**RKe**	**RKe**	**RKe**	**RKe**	**RA**	**RA**
Stage	2	1	1	1	1	1	1	2	2
Sample	13-6 black	13-2 black massive (lapilli)	13-2 greenish black	13-2 ob (lapilli)	13-2 ob	13-1 black	13-1 ob	18 cb-pb (lapilli)	18 black massive (lapilli)
Size	**bnv**	**massive**	**bnv**	**ob**	**ob**	**bnv**	**ob**	**cb-pb**	**bnv**
Condition	*highly coated*	*mod coated*	*low coated*	*highly coated*	*low coated*	*mod coated*	*mod coated*	*mod-highly coated*	*mod coated*
SiO_2	49.74	52.29	51.45	53.09	52.93	51.19	52.66	46.24	55.02
TiO_2	1.28	1.60	1.41	1.39	1.48	1.54	1.53	1.16	1.35
$Al2O_3$	17.90	16.35	17.28	15.58	16.40	16.72	16.20	19.57	16.10
FeOt	12.77	12.70	11.85	12.43	12.86	12.80	13.43	13.43	11.17
MnO	0.21	0.19	0.18	0.23	0.32	0.20	0.25	0.20	0.18
MgO	4.37	3.38	3.78	3.47	3.21	3.93	3.15	5.41	3.10
CaO	9.47	8.05	8.74	8.36	7.43	8.54	7.10	11.43	7.21
Na_2O	2.32	2.86	2.59	3.11	2.86	2.58	2.93	1.85	3.04
K_2O	1.02	1.85	1.53	1.56	1.61	1.46	1.53	0.55	2.09
P_2O_5	0.254	0.397	0.388	0.318	0.346	0.384	0.336	0.158	0.365
LOI	0.841	0.658	0.501	2.044	1.425	0.607	1.143	1.648	0.602
Total	99.33	99.68	99.20	99.54	99.44	99.34	99.11	99.99	99.61
V	301	313	591	199	205	364	224	353	273
Cr	15	16	28	11	16	21	13	9	38
Ni	13	14	19	14	18	25	11	10	15
Rb	24	47	41	42	43	43	42	8	56
Sr	429	390	437	358	359	402	362	450	354
Y	22	31	27	28	30	29	29	17	31
Zr	107	160	138	139	144	149	152	68	160
Nb	9	0	8	1	4	3	8	b.d	6
Ba	511	724	473	616	649	670	751	143	644

Appendix 3 – continues

Region	***NM***	***NM***	***NM***	***NM***	***NM***	***NM***	***NM***	***NM***	***NM***
Location	**RA**	**RA**	**RA**	**RA**	**RA**	**RA**	**RA**	**RA**	**RA**
Stage	2	2	1	1	1	1	1	1	1
Sample	18-b black bv? (lapilli)	19-a black fluidal (lapilli)	19-1 black	19-1 cb-pb	19-2 black (lapilli)	19-2 black	19-3 black bv? (lapilli)	19-3 black	19-4 gray lava? (lapilli)
Size	**bv**	**bv**	**bnv**	**cb-pb**	**bv**	**bnv**	**bv**	**bnv**	**bv**
Condition	*mod coated*	*mod coated*	*low-mod coated*	*highly coated*	*low coated*	*mod coated*	*low coated*	*low-mod coated*	*clean*
SiO_2	51.01	45.90	50.03	46.99	48.46	50.31	47.43	50.76	48.04
TiO_2	1.16	1.20	1.31	1.18	1.22	1.29	1.16	1.35	0.98
$Al2O_3$	16.67	18.91	17.46	19.02	17.95	17.63	18.87	17.60	18.83
FeOt	12.06	13.44	12.22	12.98	12.81	12.16	12.44	12.18	11.77
MnO	0.19	0.20	0.20	0.18	0.20	0.20	0.20	0.19	0.20
MgO	5.52	5.78	4.37	5.58	5.02	4.33	5.08	4.21	6.24
CaO	9.45	11.65	9.56	11.44	10.47	9.41	11.14	9.12	11.00
Na_2O	2.41	1.97	2.54	1.87	2.47	2.60	2.34	2.61	2.40
K_2O	1.18	0.69	1.26	0.64	1.13	1.29	1.03	1.34	0.58
P_2O_5	0.224	0.150	0.260	0.146	0.217	0.269	0.201	0.317	0.132
LOI	0.784	0.826	0.374	1.078	0.242	0.686	0.229	0.380	-0.147
Total	99.86	99.89	99.21	100.02	99.95	99.48	99.89	99.68	100.15
V	463	547	293	287	495	307	513	496	380
Cr	39	4	15	8	11	19	10	24	60
Ni	26	9	20	8	10	19	8	16	28
Rb	25	14	32	13	25	33	22	36	3
Sr	335	422	421	443	413	432	476	436	463
Y	23	18	23	18	21	24	18	24	15
Zr	104	65	108	66	86	114	71	119	62
Nb	b.d	6	b.d	b.d	6	b.d	9	b.d	b.d
Ba	395	185	591	251	327	512	345	432	198

Appendix 3 – continues

Region	***NM***	***NM***	***NM***	***NM***	***NM***	***NM***	***NM***	***NM***	***EM***
Location	**RA**	**RA**	**RA**	**RA**	**RA**	**RA**	**RA**	**RA**	**NRK**
Stage	1	1	1	1	1	1	1	1	3
Sample	19-4 greenish	19-4 black (lapilli)	19-4 black	19-4 cb-pb (lapilli)	19-4 cb-pb	20-1 black	20-2a black	20-3 black	43-7a gray
Size	**bnv**	**bv**	**bnv**	**cb-pb**	**cb-pb**	**bnv**	**bnv**	**bnv**	**gy**
Condition	*clean*	*low coated*	*mod coated*	*highly coated*	*mod-highly coated*	*low coated*	*low coated*	*mod coated*	*highly coated (w)*
SiO_2	49.79	49.50	49.74	45.62	45.90	48.23	49.82	47.43	45.47
TiO_2	0.81	1.33	1.29	1.21	1.20	1.22	1.33	1.20	1.29
$Al2O_3$	20.40	18.00	17.79	19.35	19.29	18.61	17.54	17.85	18.24
FeOt	10.00	12.31	12.29	13.66	13.57	11.82	12.34	12.78	14.76
MnO	0.14	0.19	0.20	0.20	0.19	0.19	0.21	0.20	0.23
MgO	4.20	4.57	4.36	5.86	5.61	4.59	4.26	5.48	6.03
CaO	10.32	9.98	9.52	11.68	11.39	10.92	9.23	10.84	9.46
Na_2O	2.40	2.50	2.57	1.79	1.76	2.57	2.54	2.23	1.78
K_2O	1.49	1.23	1.22	0.51	0.51	0.96	1.26	1.04	0.70
P_2O_5	0.210	0.291	0.251	0.128	0.133	0.150	0.277	0.201	0.223
LOI	1.904	0.411	0.451	1.311	1.234	-0.155	0.507	0.108	2.114
Total	99.75	99.91	99.22	100.00	99.55	99.25	98.81	99.25	98.18
V	312	377	346	587	499	640	328	381	539
Cr	22	18	23	11	4	20	22	15	28
Ni	20	14	20	14	5	9	26	18	15
Rb	28	28	29	10	7	17	30	26	10
Sr	650	452	433	417	435	409	419	412	470
Y	17	24	22	17	17	19	24	21	19
Zr	82	113	105	65	68	73	111	81	76
Nb	b.d	2	7	19	b.d	4	6	b.d	b.d
Ba	563	440	595	182	245	325	481	360	334

Appendix 3 – continues

Region	***EM***	***EM***	***EM***	***EM***	***EM***	***EM***	***EM***	***EM***	***EM***
Location	**NRK**	**NRK**	**NRK**	**NRK**	**NRK**	**NRK**	**NRK**	**RS**	**RS**
Stage	3	3	2	2	2	2	2	2	2
Sample	43-6 gray	43-5 gray	43-3b gray	43-3b gray (lapilli)	43-3b black (lapilli)	43-3a gray	43-1 gray	45-b gray (lapilli)	45-b gray
Size	**gy**	**gy**	**gy**	**gy**	**gy**	**gy**	**gy**	**gy**	**gy**
Condition	*mod-high coated*	*mod-high coated*	*mod coated*	*mod-highly coated*	*mod-highly coated*	*mod coated*	*low coated*	*mod coated (w)*	*mod coated (w)*
SiO_2	44.45	46.18	44.79	46.07	45.42	46.59	46.55	47.14	44.59
TiO_2	1.37	1.31	1.31	1.23	1.21	1.25	1.22	1.21	1.46
$Al2O_3$	19.31	18.93	19.44	18.48	18.96	18.98	19.08	19.49	18.39
FeOt	14.87	14.80	14.44	13.75	13.85	13.85	13.33	13.52	15.98
MnO	0.21	0.23	0.20	0.20	0.20	0.21	0.20	0.21	0.21
MgO	6.08	5.42	5.72	5.94	6.54	5.26	5.17	6.09	7.26
CaO	10.62	9.16	10.11	10.84	11.34	9.96	10.44	9.30	9.56
Na_2O	1.61	1.88	1.62	2.08	1.62	1.99	2.08	2.03	1.63
K_2O	0.68	0.82	0.76	1.08	0.71	0.95	0.92	0.55	0.42
P_2O_5	0.240	0.242	0.195	0.210	0.205	0.242	0.217	0.208	0.139
LOI	1.653	2.115	2.105	0.975	1.782	1.222	0.914	2.940	2.007
Total	99.44	98.97	98.58	99.88	100.05	99.29	99.20	99.74	99.62
V	957	536	588	633	651	910	809	452	584
Cr	27	23	40	49	47	22	33	53	28
Ni	26	17	24	25	32	23	22	31	21
Rb	13	14	12	20	7	18	18	5	3
Sr	476	470	502	474	484	520	508	408	363
Y	19	20	19	19	18	20	19	15	15
Zr	75	84	78	74	69	79	76	74	61
Nb	b.d	0	b.d	b.d	14	b.d	b.d	1	b.d
Ba	294	378	395	228	265	337	394	272	393

Appendix 3 – continues

Region	**EM**	**EM**	**NL**	**EL**	**EL**	**NSC**	**NSC**	**NSC**	**NSC**
Location	**RS**	**RS**	**nl**	**el**	**el**	**sc**	**sc**	**sc**	**sc**
Stage	2	2							
Sample	45-a gray (lapilli)	45-a gray	15-b	38 felsic (bright)	38 mafic (dark)	21-2b sc	21-2b sc	22-5 sc	22-5 sc
Size	**gy**	**gy**	**nl**	**el**	**el**	**sc**	**sc**	**sc**	**sc**
Condition	*mod coated (w)*	*low coated (w)*	*clean*	*clean*	*clean*	*clean*	*clean*	*clean*	*clean*
SiO_2	44.39	44.57	46.12	45.33	45.51	43.23	43.32	41.40	42.95
TiO_2	1.41	1.48	1.20	0.96	0.97	1.48	1.49	1.60	1.55
$Al2O_3$	20.83	17.95	19.34	15.58	15.26	17.61	17.50	16.73	17.34
FeOt	15.71	15.89	12.74	13.01	12.78	14.74	15.09	17.11	15.47
MnO	0.20	0.20	0.20	0.20	0.19	0.18	0.18	0.18	0.18
MgO	7.34	7.10	5.26	11.08	11.11	6.60	6.68	7.50	6.88
CaO	7.98	9.96	11.42	11.81	12.24	12.79	13.09	12.58	13.17
Na_2O	1.32	1.59	2.27	1.61	1.50	1.84	1.72	1.65	1.72
K_2O	0.37	0.46	1.17	0.32	0.31	0.62	0.58	0.53	0.58
P_2O_5	0.232	0.152	0.180	0.084	0.077	0.080	0.070	0.065	0.071
LOI	2.653	2.034	-0.151	-0.460	0.358	-0.564	-0.458	-0.598	-0.319
Total	99.77	99.36	99.89	99.97	99.94	99.17	99.72	99.34	99.91
V	740	618	426	392	487	1343	843	1823	852
Cr	29	47	7	142	163	0	3	22	6
Ni	24	28	12	66	58	15	16	27	20
Rb	1	5	30	-1	0	4	6	3	2
Sr	364	346	460	288	276	299	298	274	295
Y	16	16	19	13	13	15	15	15	14
Zr	62	63	69	36	36	43	42	39	43
Nb	0	5	b.d	b.d	b.d	b.d	b.d	b.d	3
Ba	322	402	274	147	182	201	179	155	225

Appendix 4. Trace elements concentration in ppm.

Trace elements	***Standard***		***Sample***									
(ppm)	**JB-1b**	**JA-1**	**22-5 sc**	**21-2b sc**	**15b**	**38m**	**46b gray**	**45a gray**	**43-B gray**	**43-6 gray**	**18 cb-pb**	**19-3 black bv?**
Co	37.39	10.69	118.74	156.84	71.61	77.52	212.05	96.77	130.65	115.24	130.94	147.99
Y	18.56	24.65	14.78	15.12	18.23	12.71	16.68	14.27	19.01	18.06	16.96	18.69
Zr	122.42	79.61	27.91	29.40	46.43	23.48	51.38	43.77	51.88	46.26	45.81	48.60
Nb	22.98	1.15	0.96	1.14	2.01	0.78	2.22	1.53	2.18	2.09	1.84	3.08
Cs	0.80	0.61	0.37	0.39	1.10	0.19	0.35	0.13	1.04	0.46	0.43	0.76
La	36.85	4.64	2.56	2.75	10.20	2.07	5.88	3.65	10.72	8.27	7.33	10.58
Ce	63.28	12.16	6.06	6.55	21.84	5.29	13.35	8.55	20.66	17.22	16.27	21.45
Pr	6.74	1.99	0.96	1.02	2.90	0.86	2.00	1.36	2.97	2.41	2.26	2.86
Nd	24.99	10.39	5.24	5.55	13.18	4.75	9.63	6.76	13.55	11.43	10.78	13.01
Sm	4.69	3.26	1.90	1.98	3.54	1.64	2.75	2.18	3.57	3.09	2.97	3.35
Eu	1.43	1.08	0.78	0.80	1.24	0.69	1.08	0.89	1.27	1.15	1.09	1.21
Gd	4.81	4.10	2.62	2.69	3.94	2.18	3.24	2.64	4.11	3.51	3.47	3.83
Tb	0.67	0.70	0.46	0.47	0.62	0.39	0.53	0.45	0.63	0.56	0.55	0.60
Dy	3.76	4.58	2.98	3.02	3.67	2.50	3.27	2.90	3.77	3.42	3.47	3.66
Ho	0.74	0.99	0.61	0.63	0.75	0.53	0.68	0.59	0.76	0.72	0.70	0.74
Er	2.08	2.88	1.75	1.80	2.09	1.53	1.93	1.72	2.15	2.11	2.04	2.15
Tm	0.29	0.42	0.24	0.24	0.29	0.21	0.28	0.25	0.29	0.30	0.28	0.30
Yb	1.91	2.82	1.50	1.55	1.92	1.38	1.82	1.64	1.96	2.04	1.88	1.94
Lu	0.28	0.43	0.22	0.22	0.28	0.20	0.28	0.25	0.27	0.29	0.27	0.29
Hf	3.13	2.39	0.95	0.98	1.30	0.77	1.52	1.29	1.47	1.35	1.30	1.36
Ta	1.70	0.18	2.34	3.10	1.13	0.71	2.07	0.60	1.74	2.13	1.68	2.24
Pb	5.42	5.36	2.03	2.01	2.92	1.76	3.33	2.56	3.93	4.49	3.07	3.27
Th	8.74	0.71	0.48	0.53	2.10	0.28	1.30	0.80	2.09	1.53	1.45	1.79
U	1.48	0.34	0.15	0.16	0.66	0.11	0.24	0.12	0.50	0.38	0.39	0.58

Appendix 4 – continues

Trace elements	***Sample***										
(ppm)	**19-4 black fluidal**	**19-4 cb-pb**	**13-2 ob**	**13-11 black**	**14-4a ob**	**4-6 black juv?**	**4-6 cb (B)**	**4-13 black**	**3-3 cb-pb**	**1-5 ob**	**1-9 bv**
Co	121.68	116.31	140.61	140.05	100.38	150.75	192.90	254.47	111.59	133.75	151.76
Y	18.32	17.02	29.50	33.21	33.55	21.40	14.77	34.04	12.79	39.35	16.75
Zr	47.86	45.40	134.70	141.08	141.31	69.48	41.89	147.95	37.56	144.64	37.55
Nb	1.96	1.82	5.42	5.65	5.51	2.37	1.53	5.93	1.13	5.61	1.40
Cs	0.62	0.53	3.32	2.63	2.55	1.09	0.48	2.57	0.38	2.33	0.56
La	8.04	6.89	15.27	16.25	17.83	8.06	4.85	17.12	4.36	19.34	4.45
Ce	18.09	17.26	34.24	35.92	37.33	17.31	9.86	36.83	8.78	42.97	10.83
Pr	2.45	2.20	4.34	4.91	5.12	2.66	1.71	5.13	1.61	5.92	1.68
Nd	11.52	10.43	19.61	22.42	22.75	12.73	8.46	23.38	7.86	27.32	8.63
Sm	3.15	2.92	5.04	5.73	5.64	3.46	2.40	5.98	2.31	6.95	2.54
Eu	1.16	1.09	1.42	1.62	1.65	1.18	0.95	1.69	0.87	1.98	1.00
Gd	3.72	3.49	5.54	6.51	6.40	4.07	2.84	6.65	2.64	7.61	3.06
Tb	0.60	0.56	0.90	1.03	1.02	0.66	0.47	1.05	0.46	1.20	0.50
Dy	3.63	3.40	5.53	6.36	6.30	4.03	3.01	6.44	2.84	7.37	3.21
Ho	0.74	0.69	1.16	1.30	1.31	0.85	0.64	1.33	0.59	1.53	0.67
Er	2.15	2.00	3.40	3.81	3.81	2.46	1.84	3.88	1.71	4.49	1.95
Tm	0.30	0.28	0.49	0.54	0.55	0.36	0.26	0.55	0.25	0.64	0.28
Yb	1.98	1.86	3.31	3.62	3.70	2.36	1.72	3.68	1.67	4.29	1.84
Lu	0.28	0.26	0.49	0.53	0.55	0.35	0.25	0.54	0.24	0.63	0.28
Hf	1.35	1.29	3.57	3.76	3.76	1.94	1.24	3.92	1.13	3.95	1.14
Ta	1.90	1.43	2.09	2.80	1.74	1.12	2.69	3.63	1.34	3.03	2.74
Pb	2.93	2.83	11.49	10.70	13.67	5.58	3.48	11.57	3.47	12.02	3.44
Th	1.55	1.51	4.76	4.85	5.17	1.79	0.82	4.85	0.56	3.80	0.60
U	0.42	0.35	1.11	1.22	1.19	0.41	0.18	1.21	0.15	0.86	0.18